ISSN en trámite

# Geofísica Internacional

Revista Trimestral Publicada por el Instituto de Geofísica de la Universidad Nacional Autónoma de México

México
Volume 58 Number 2
April - June
2019

# — Geofísica Internacional —

**GEOFÍSICA INTERNACIONAL**, Año 58, Vol. 58, Núm. 2, abril - junio de 2019 es una publicación trimestral, editada por la Universidad Nacional Autónoma de México, Ciudad Universitaria, Alcaldía Coyoacán, C.P. 04150, Ciudad de México, a través del Instituto de Geofísica, Circuito de la Investigación Científica s/n, Ciudad Universitaria, Alcaldía Coyoacán, C.P. 04150, Ciudad de México, Tel. (55)56 22 41 15. URL: http://revistagi.geofisica.unam.mx, correo electrónico: revistagi@igeofisica.unam.mx. Editora responsable: Andrea Rostan Robledo. Certificado de Reserva de Derechos al uso Exclusivo del Título: 04-2022-081610251200-102, ISSN: en trámite, otorgados por el Instituto Nacional del Derecho de Autor (INDAUTOR). Responsable de la última actualización Saúl Armendáriz Sánchez, Editor Técnico. Fecha de la última modificación: 31 de marzo 2019, Circuito de la Investigación Científica s/n, Ciudad Universitaria, Alcaldía Coyoacán, C.P. 04150, Ciudad de México.

Geofísica Internacional

Vol. 58, Núm. 2, abril-junio de 2019

## Contents

Geofísica Internacional (2019) 58-2: 101-111

Original paper

# Geomagnetic anomalies in the area of Popocatepetl volcano, Mexico

A. Kotsarenko, V. Yutsis*, V. Grimalsky, S. Koshevaya and Yu. Kotsarenko

Received: May 05, 2017; accepted: November 14, 2018; published on line: April 01, 2019
DOI: http://dx.doi.org/10.22201/igeof.00167169p.2018.58.2.1953

**Resumen**

Las anomalías geofísicas de diferente naturaleza observadas en el área del volcán Popocatépetl se presentan y analizan en este artículo. Las anomalías encontradas son de origen volcánico. El ambiente electromagnético en las cercanías del volcán resultaron tener más ruido que las estaciones de referencia; una fuerte actividad geomagnética similar al ruido fue observada en la componente H; además solamente se detectaron pulsaciones geomagnéticas en la estación Tlamacas (localizada a 4 km del volcán). Algunos cambios notables en la evolución del índice fractal calculado para el campo geomagnético pueden estar conectados a la presencia de procesos críticos, los cuales pueden estar ocurriendo en la dinámica del volcán.

Palabras clave: actividad volcánica, anomalía geomagnética, índice fractal, Popocatépetl.

**Abstract**

Geomagnetic anomalies of different nature observed in the area of Popocatepetl volcano are presented and analyzed in the current paper. The analysis reveals some anomalies considered to be of local volcanic origin: the EM background in the vicinity of the volcano was found to be significantly noisier than other reference stations; sporadic strong noise-like geomagnetic activity was observed in the H-component; some geomagnetic pulsations were observed only at Tlamacas station (located 4 km near the volcano). Some noticeable changes in the evolution of the fractal index calculated for geomagnetic field may be connected to the presence of critical processes in the volcano dynamics.

Key words: volcano activity, geomagnetic anomaly, fractal index, Popocatepetl.

A. Kotsarenko
Facultad de Ingeniería
Universidad Autónoma del Carmen
Cd. del Carmen, Campeche, México

V. Yutsis*
División de Geociencias Aplicadas
Instituto Potosino de Investigación Científica
y Tecnológica, A.C.
San Luis Potosí, 78216
S.L.P., México
**Corresponding author:* vsevolod.yutsis@ipicyt.edu.mx

V. Grimalsky
S. Koshevaya
Centro de Investigación en Ingeniería
y Ciencias Aplicadas
Universidad Autónoma del Estado de Morelos
Cuernavaca, Morelos, México

Yu. Kotsarenko
Independent Researcher
Cuernavaca, Morelos, México

## Introduction

The object of our interest, Popocatepetl volcano (nicknamed El Popo, Figure 1, top left), is located in Central Mexico (19.0N, 98.6W) at 5465 m altitude. It is one of several active volcanoes that form the Trans-Volcanic Belt of Mexico (also known as Neo-Volcanic Axis) and its existence is related to the geodynamics of the North American and Cocos plates. El Popo is one of the major geological hazards in Mexico, if a sudden eruption would take place (Figure 1, top right), it may result in one of the most dramatic natural disasters in contemporany mexican history due to the fact that El Popo is situated near one of the world's most populated areas (Figure 1, bottom left): Mexico City (about 70 km southeast) and the nearby populations of Puebla (about 45 kilometers west) and Cuernavaca (about 60 kilometers northeast) among others. More than 30 million people live within view distance of the volcano and hundreds of thousands of people would be endangered by hazards associated with a large explosive eruption of the volcano (Macías Vázquez *et al*., 1995). A major eruption would have serious consequences for people living in communities on the flanks of the volcano, and ash from such an eruption could also endanger aircraft using Mexico City international airport.

About 30 eruptions have been reported in historical time (although documentation is poor), the latest significant activity took place from 1920-22. During the eruptive activity from December 2000 (Figure 2) more than 56,000 people were evacuated from the surrounding area and more than hundred civilian air flights departing and landing at Mexico City airport were cancelled. Besides of that, El Popo is a permanent source of the ash periodically polluting nearby metropolitan areas (Juárez *et al*., 2005). Due to its recent activity Popocatepetl volcano is the object of constant seismic and volcanic monitoring by CENAPRED (National Mexican Center for Disasters Prevention) and also the actual interest to establish a station for permanent geomagnetic monitoring of the volcano. Present activity of Popocatepetl volcano can be briefly summarized as follows.

Light eruptions occur everyday: from several to tens of eruptions of gas and water can be daily observed during quiet volcano phases, up to 50-100 eruptions occurred in the active phases (González-Pomposo, 2004; Arámbula-Mendoza *et al*., 2010). In several months moderate eruptions of gases and volcano ash take place from one to several times per day for quiet and active phases, respectively. Moderate eruptions can also be accompanied by explosive elements (rocks injection), with a frequency from several to dozens of events per year in recent times. Major eruptive activity is not so frequent. The last time such activity occurred it lasted from December 2000 to January 2001. At this stage intensive rock expulsions, lava eruptions and pyroclastic flows take place in addition to the above mentioned phenomena. Tectono-volcanic micro-seismic events with magnitudes up to Ms=2-3 and high frequency tremors are also part of the volcano activity.

Geomagnetic anomalies observed in the area of Popocatepetl volcano in the period 2003-2009 during constant monitoring of magnetic field in Tlamacas station are presented in this paper.

Different long-term observatories all over the world collected in monographs (Hayakawa and Fujinawa, 1994; Hayakawa, 1999) points the ULF EM (Ultra Low Frequency Electro-Magnetic) band as very promising for EM emission monitoring generated in the period preceding strong seismic events. The number of volcano-related EM studies is quite smaller but some of them deserve a particular interest (Currenti, *et al*., 2005, Enomoto, et.al., 2006, Fujinawa *et al*., 2006) proving the possibility of generation of similar signals associated with a volcanic activity.

## Geological setting

Popocatepetl is a Pliocene-Quaternary stratovol-cano situated 65 km SE of Mexico City and 45 km to the west of the city of Puebla, in the frontal part of the Trans-Mexican Volcanic belt (TMVB) (Figure 1 and 2) on a basement of Paleozoic metamorphic and Cretaceous sedimentary rocks (Macías *et al*., 2005; Espinasa-Pereña and Martin-Del Pozo, 2006). The volcano forms the southern end of the Sierra Nevada volcanic range. Its stratigraphic column consists of pyroclastic deposits (sandy ash, pumice, ash flow, lithic clasts of granodiorite, hornfels, arenite and other xenolites) erupted during the past 23,000 yr. BP (Siebe *et al*., 1995, Siebe and Macías, 2006). Mooser *et al*. (1996) report the existence of three units differentiated by their lithology. The first corresponds to the Popocatepetl volcano, composed of andesitic, dacitic and rhyolitic lavas alternating with pyroclastic materials. The second corresponds to the foothills of the volcano, and is composed of pyroclastic potent layers as ash and pumice, plus materials such as lahar, fluvial and fluvio-glacial deposits. This whole set is called the Tarango Formation. The third unit consists of a different type of

monogenetic volcanoes that are located in the SW sector of the volcano on its piedmont. These form part of the Chichinautzin Group, where cones of scoria with extensive lava flows of basic and intermediate composition, i.e., where basalts and andesites, are dominating.

## Data collection and processing

Geomagnetic monitoring of Popocatepetl volcano was established on March 8, 2002, as a complimentary part of the Tlamacas seismic station (CENAPRED, *98º 37′ 41″ W, 19º04′*


**Figure 1.** Popocatepetl. Quiet volcano, January 2005 (a). Eruption of Popocatepetl, December 2000 (b). Map of the volcano Popocatepetl (red circle) and Tlamacas station (blue arrow) (c). Gas eruptions as seen from the Tlamacas station (d).


**Figure 2.** Popocatepetl eruption, December 19, 2000. Photo courtesy of Mexico National Center of Prevention of Disasters (CENAPRED).

*01″ N*) located 4 km near the volcano crater (Figure 1, bottom right). First data collected by Torsion type 3-axial magnetometer (GPS-synchronization, 50 Hz sample frequency, designed at St-Petersburg IZMIRAN Dept.) appeared to be contaminated by an intensive periodical multi-band noise coming from the near-buried seismograph cables, as well as the precision of the instrument went down. Recording of the data was renewed in 2003 with a 3-coordinate fluxgate magnetometer (GPS, 1 Hz, designed at UCLA). The results from 2003-2004 (Kotsarenko *et al*., 2005a) due to the numerous power cuts frequently occurred in the observation spot cover an unlucky short time intervals and therefore are considered not very reliable. The powerful USP system established in the 2005 permitted to collect a 5 month constant monitoring data (March-July, 2005) which are analyzed in this study.

The study includes the analysis of dynamic spectra as part of a traditional analysis for the continuous component of the magnetic field and the analysis of geomagnetic micro-pulsations for the pulse component. Temporal intervals with a high geomagnetic activity (estimated by equatorial Dst index) are normally discarded from the analysis. In order to distinguish the local character of the observed phenomena from the global ones compared our results where compared with those calculated from reference stations: the closest Mexican station Juriquilla (JU2 and other geomagnetic stations integrated to the Mid-Continent Magneto-seismic Chain (McMAC, Chi et.al., 2005) network are equipped with the same instrument (Table 1).

Another subject of study was the geomagnetic fractal dynamics which emphasize the character of the criticality of the SOC (Self Organized Critical) processes contributed to the geomagnetic field (Gotoh *et al*., 2004,; Kotsarenko *et al*., 2004 and 2005b).

As the SOC processes emphasize tendency $S(f) \sim f^{-\beta}$ (where $S$ is a spectral density of the signal and $f$ is the frequency), the FFT (Fast Fourier Transform) was used for calculation of tectono-volcanic events $\beta$ as the slope of the line that best fits $log(S) - vs - log(f)$.

**Results**

The analysis of the obtained results shows the following tendencies:

1. The general EM background in the vicinity of the volcano is significantly noisier than in the Juriquilla or the other reference stations (Figure 3). In the very low frequency range, up to 0.01-0.02 Hz, both TLA and JU2 are characterized by rather similar noise intensity, with some "flares" at 2:00 and 6:00. For larger frequency bands, TLA is on the average noisier than JU2. The observed feature has a mostly permanent character.

2. The strong noise-like geomagnetic activity in the H-component of magnetic field with intensity up to tens of gammas and duration from several hours (Figure 4) up to several days (Figure 5) was detected only in the TLA geomagnetic data 13 times during the observations time. These events sometime accompanied by a weak and moderate eruptive activity (mostly gas or water) of the volcano and local seismic events, but at all other times it occurs without any observed activity.

3. Some geomagnetic pulsations observed at LA station (Figure 6) were not detected at the reference station, and use to be locally generated in the volcano area. The observed pulsation do not reveal any dominant direction (arbitrary polarization). Observed phenomena have similarity with seismo-related effects (Kotsarenko *et al*., 2004).

**Table 1.** Description (Geographic Coordinates) for Tlamacas and reference stations.

| Station name | Abbreviation | Latitude N | Longitude E |
|---|---|---|---|
| San Gabriel Dam | SGD | 40.7 | 242.2 |
| Boulder | BLD | 40.1 | 254.8 |
| Juriquilla | JU2 | 20.6 | 259.6 |
| Tlamacas | TLA | 19.0 | 261.4 |
| Jicamarca | JIC | -12.0 | 283.1 |

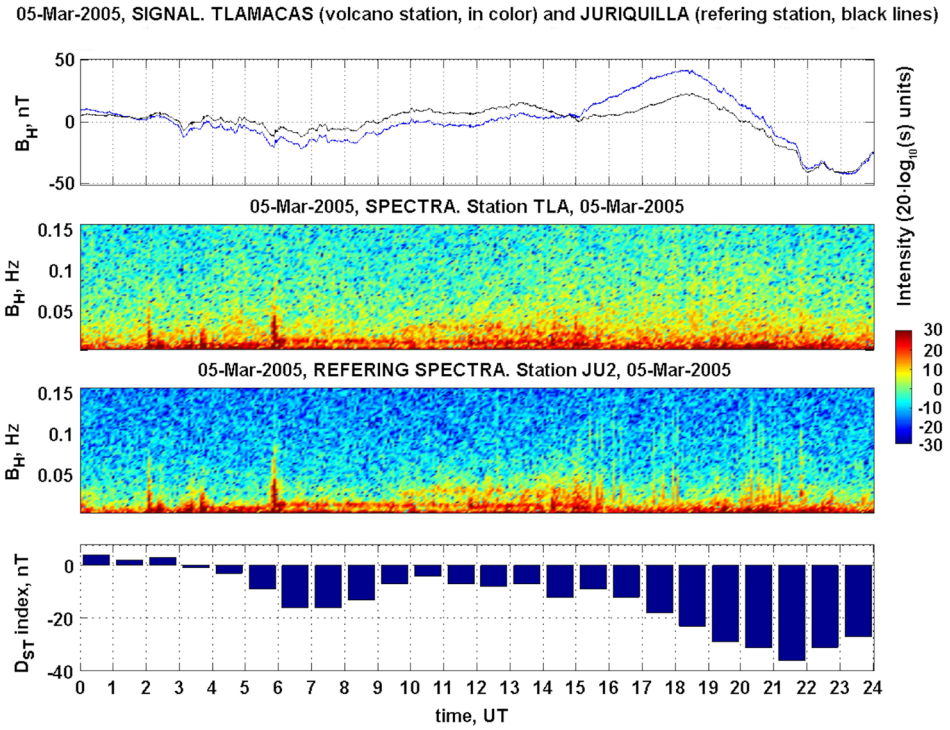


**Figure 3.** Top panel. H-component signals, Tlamacas (blue line) and Juriquilla (black line). 2nd and 3rd panels: Tlamacas and Reference spectrogram accordingly. Bottom panel: Dst index of geomagnetic activity. The spectral intensity of the noise background is higher in the Tlamacas (2nd panel); domination of more intensive orange colors in contrary to the weaker green and blue seen at the 3rd panel, Juriquilla, the reference station.

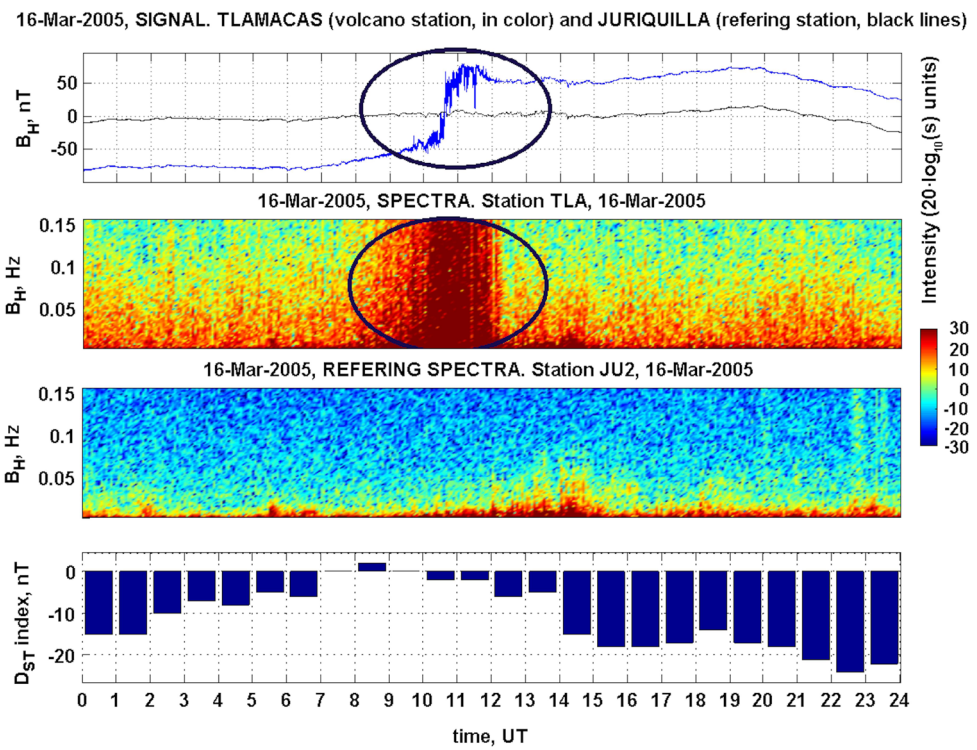


**Figure 4.** The intensive (100 nT change of the base value, up to 50 nT in the noise amplitude) perturbation observed in the signal at Tlamacas station (blue line) in compare with a referent Juriquilla signal (black line) (top panel); and its spectra (2nd panel). Referent (not-perturbed) Juriquilla spectra (3rd panel) observed under geomagnetically quiet period. Dst index of geomagnetic activity (bottom panel).

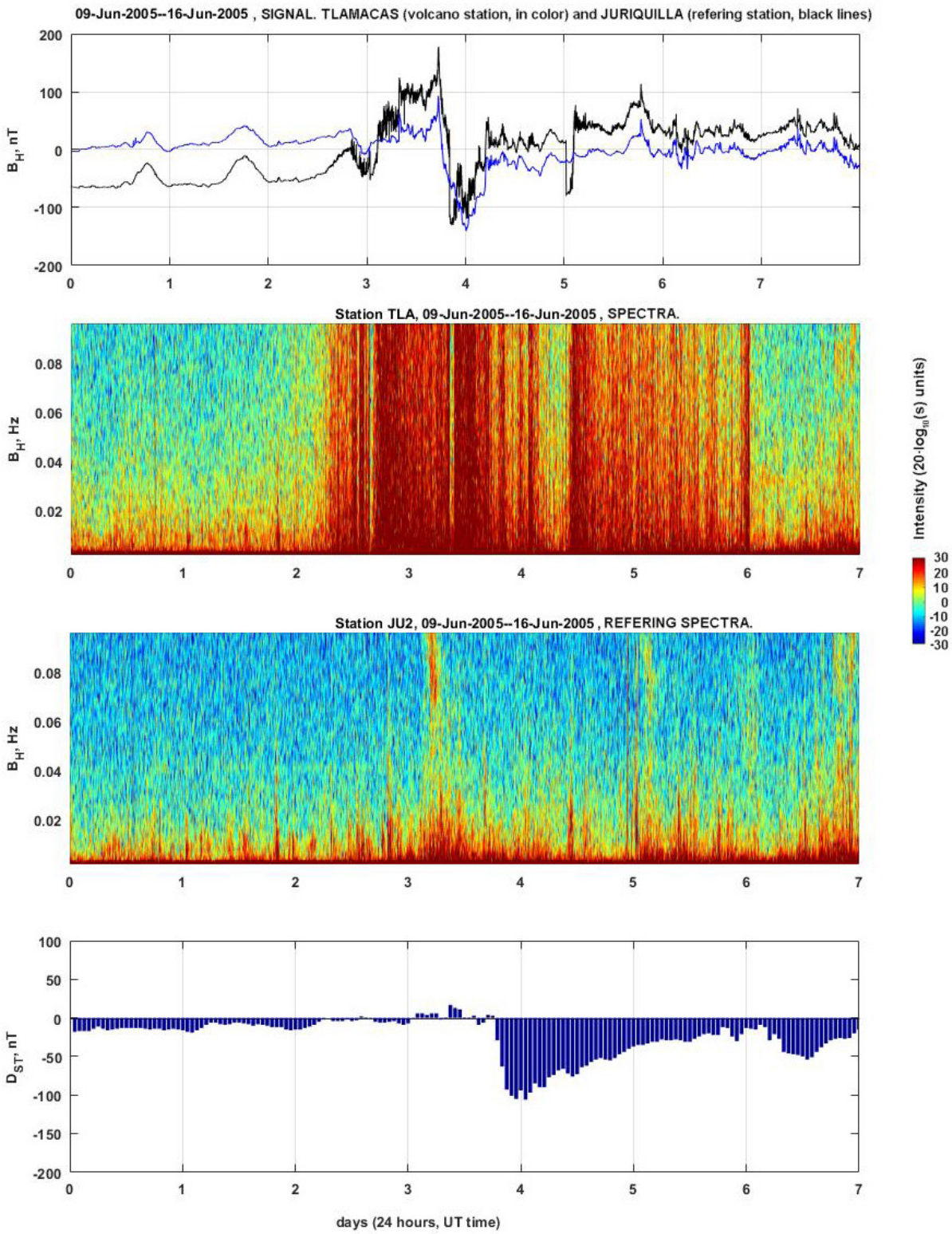


**Figure 5.** Top panel. Noise-like geomagnetic behavior observed several days in the signal of Tlamacas station (blue line) in compare with a referent Juriquilla signal (black line), and its spectra (2nd panel). Referent (not-perturbed) Juriquilla spectra (3rd panel). Bottom panel: Dst index of geomagnetic activity.

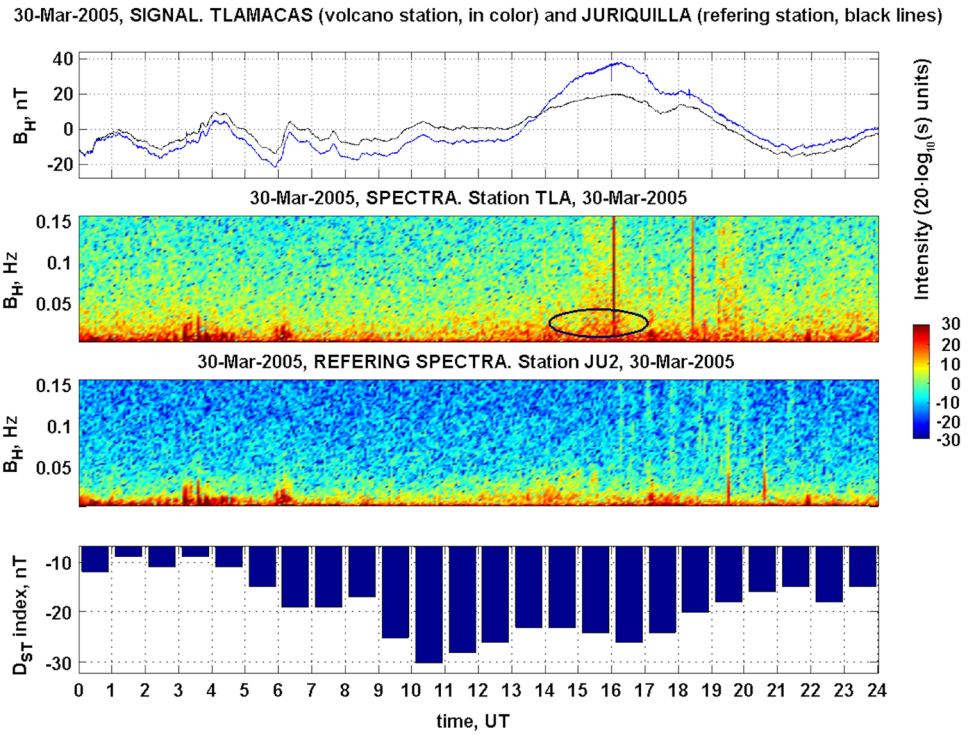


**Figure 6.** The example of locally generated PC4-like geomagnetic micro-pulsation is marked by ellipse. In the presented case the pulsation intensity is more expressed in the H-component. The table of symbols is the same as in Figures 4-5.

4. The dynamics of the fractal index for the LA station, in comparison with the reference station, show 1-2 days drops during geomagnetically quiet days (marks 1-4, Figure 7) whereas at the other stations results are rather comparable (especially for the northern stations, the Jicamarca station is located at Zero magnetic latitude). Events 1-3 may indicate the increase of the level of criticality in the processes that contributed to the signal (also see Kotsarenko *et al*., 2004, 2005b) while event 4 is probably related to the effect of a geomagnetic storm.

## Discussion

As the observed phenomena have occurred in an electromagnetically calm place as a volcano, the following provisional models that could possibly explain the mentioned anomalies are presented:

1. As the magma has good conductive properties, convective circular motion in the magmatic reservoir may create a perturbed magnetic field due to the effect of self-induction.

2. The thermal heating may induce re-magnetization processes in the rock medium.

3. The different mechanisms of micro-fracturing (already developed) may be enhanced by the conductive currents in the lava.

4. The effect of the magneto-striction simulated by stressed rock movement may also be possible source of the generated emission (in analogy to the electro-striction).

Among the observed anomalies one (the highly perturbed H-component, Figures 4 and 5) is a subject of special interest and should be discussed separately. Similar links to the observed phenomena were presented in Martin-Del Pozzo *et al*. (2002). The significant differences between these results and the presents one are that the firts authors used a total field magnetometer system and, therefore, could not distinguish the polarization of the observed signals. The actual polarization of the perturbations, mostly expressed in the horizontal component, makes the recently obtained result important because it indicates

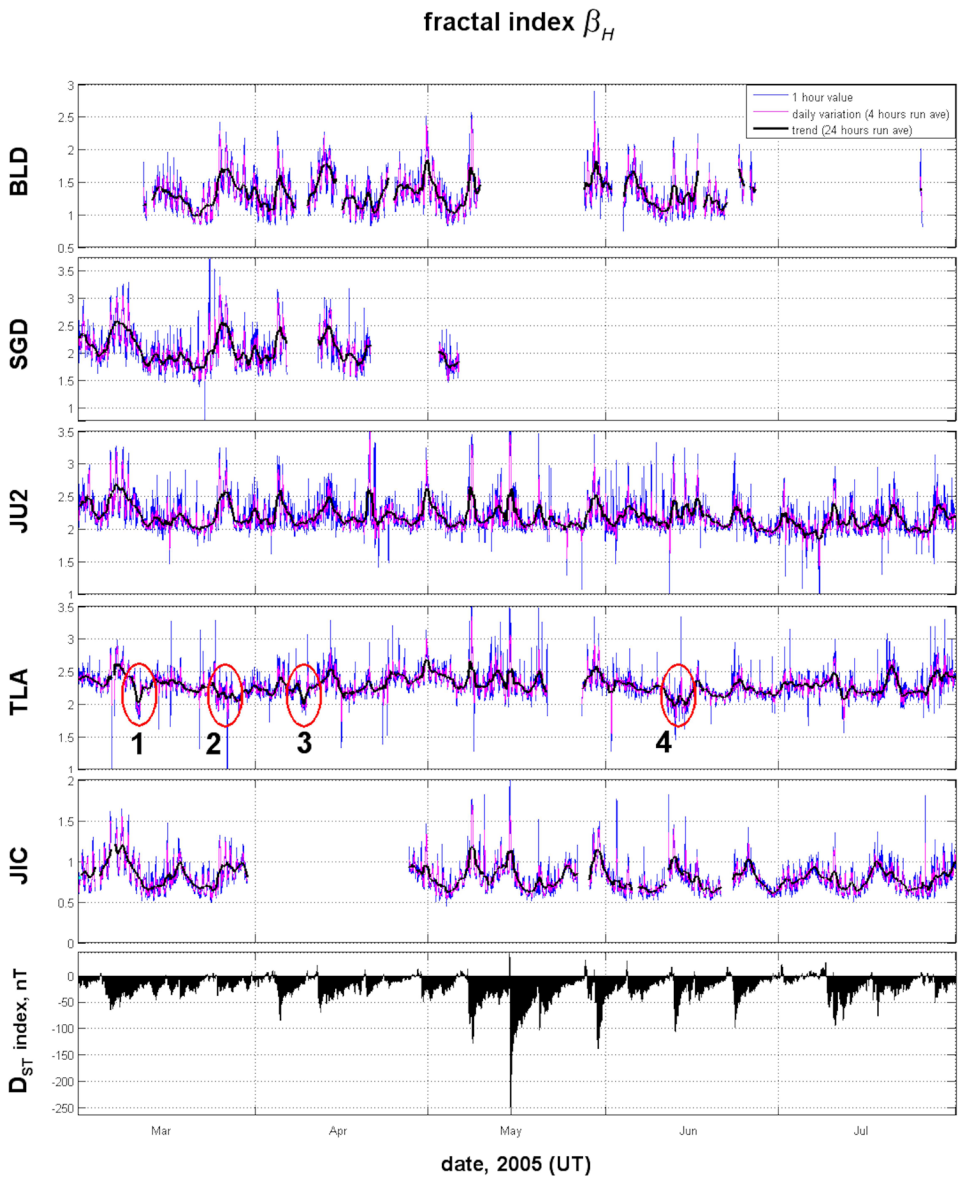


**Figure 7.** Dynamics of the fractal index β calculated for geomagnetic field at Tlamacas and referring stations (see for description Table 1). Local drops in geomagnetic fractal dynamics (marked by ellipses 1-4) may indicate some critical processes occurred in the region of volcano.

certain anisotropy in their generation, or a specific geometry of the source system. The majority of natural physical mechanisms capable of producing similar perturbations, such as the already mentioned re-magnetization and magmatic flows, are in general, isotropic. Another suitable mechanism, magneto-striction, implies friction in the rock medium, i.e. tectono-volcanic events and therefore does not match the evidence, because most of the observed perturbations occur under seismically quiet periods.

In the present study original mechanism of the generation, can theoretically explain the strict polarization of the perturbations is shown. It is based on the specific geometry of the source. The possible existence of an additional lateral magmatic camera (or broad magmatic channel) besides the main magmatic reservoir is proposed. This camera should have *flat* geometry and be oriented strictly perpendicular to the line S-N, which almost coincides with the axis LA – Popocatepetl Crater with a very small deviation. From this, circular

motions in that hypothetical flat camera will produce manifestations of the H-component of the geomagnetic signal only.

To estimate a possible current configuration that could yield the measured values and directions of the magnetic field, let us consider the simplest circular closed loop with current (Figure 8). It is well-known (Batygin and Toptygin, 1978) that the magnetic field of the loop with electric current is given by the formula:

$$B_\rho = \frac{\mu_0 I}{2\pi}\frac{y}{\rho[(R+\rho)^2+y^2]^{1/2}}\times\left[-K(k)+\frac{R^2+\rho^2+y^2}{(R-\rho)^2+y^2}E(k)\right];$$
$$B_y = \frac{\mu_0 I}{2\pi}\frac{1}{[(R+\rho)^2+y^2]^{1/2}}\times\left[K(k)+\frac{R^2-\rho^2-y^2}{(R-\rho)^2+y^2}E(k)\right];$$
$$B_\varphi = 0; \quad k^2 = \frac{4R\rho}{[(R+\rho)^2+y^2]} \qquad (1)$$

Here $I$ is the value of the electric current, $K(k)$ and $E(k)$ are the elliptic integrals of the first and second kinds. That the volcanic rocks are assumed nonmagnetic. In the present case, the magnetic component in one specified direction dominates. A possible origin of such a field can be the loop with electric current oriented in the vertical direction, when the normal vector to the area of the loop is directed along the line S-N. Under conditions $\rho << R$, $y \sim R$ we have:

$$B_\rho \approx 0; B_y \approx \frac{\mu_0 R^2 I}{2(R^2+y^2)^{3/2}} \qquad (2)$$

In this configuration, the measured magnetic field is directed along the y-axis. For the estimations, $R$ = 2 km (a possible size of current loop within the volcano´s body), $y$ = 2 km, $B_y$ = 100 nT are used. From (2), one can get $I \approx 10^3$ $A$.

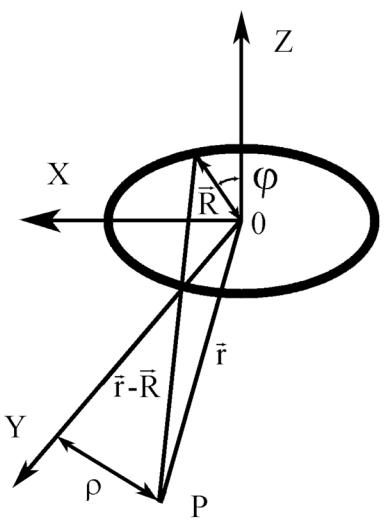


**Figure 8.** Schematic source configuration for the flat magmatic camera (ring) for the calculation of the magnetic field in the observation point (P).

Assuming the shape of the ring as a torus with the radius of its internal cross-section $a << R$, it is possible to estimate a density of the current within such a torus:

$$i \approx \frac{I}{\pi_a^2} \qquad (3)$$

The estimations for realistic values of such a radius are $a$ = 200 m give $j \approx 0.01$ A/m$^2$.

This model is still very hypothetic. However, on the basis of the results by Zúñiga and Valdés (2007) analysis of the spatial distribution of magnitudes of the local seismicity in the vicinity of Popocatepetl volcano points out a possible existence of a new magma chamber. Eventually, to prove this hypothesis, permanent simultaneous observations at different points (at least 4) separated by distances of 1- 10 km and situated at different heights are desirable. A more solid confirmation can be obtained from geophysical and geological studies in the area of the volcano.

Finally, geomagnetic micro-pulsations with arbitrary elliptical polarization was detected, locally generated in the vicinity of the volcano, not observed in the reference station. The event presented in Figure 6 was observed during an intense and long-duration volcano eruption (it started at 11:21 UT, and the cloud raised up to 1.5 km moving in the N-W direction). Their possible sources could involve collective properties of the extending aerosol (dusty) plasma like the generation of different plasma instabilities due to the motion of the ionized (and metallic) particles erupted from the crater.

Unfortunately, the precision of the instrument (noise power is $10^{-3}$ nT$^2$/Hz at 1 Hz) prevent to confidently resolve them from the enhanced noise level, especially at the time when the eruption began.

## Conclusions

A series of anomalies of different geophysical nature were presented in the current paper. Description of the geomagnetic anomalies observed at Popocatepetl volcano were shown have a discussion of the possible mechanisms of their generation. The first two phenomena observed, EM noisy background and strong

burst-like activity, reveal manifestations of the internal dynamics of the volcano related to the local geomagnetic field, and, therefore, their future analysis could be useful to obtain some latent processes at the body of the volcano, which are difficult to locate by traditional methods. The last phenomena, the locally generated magnetic pulsations, can also serve as a marker for the direction and velocity of the motion of eruptive clouds (using triangulation technique in case the geomagnetic station set is greater than 4) and, therefore, can also be useful for an efficient prevention of the pollution in the air and nearby populated lands.

**Acknowledgments**

Authors would like to thank Prof. Corrado Cigolini and an anonymous reviewer for their comments and suggestions that improved the manuscript.

**References**

Arámbula Mendoza R., Valdés González C., Martínez Bringas A., 2010, Temporal and spatial variation of the stress state of Popocatépetl volcano, Mexico. *J. Volcanol. Geotherm. Res.,* 196, 156–168.

Batygin, V. and Toptygin, I., 1978, Problems in Electrodynamics, Academic Press, N.Y., 574 pp.

Chi P.J., Engebretson M.J., Moldwin M.B., Russell C.T., Mann I.R., Samson J.C., López

Cruz-Abeyro J.A., Yumoto K. and Lee. D.-H., 2005. Mid-continent Magnetoseismic Chain (McMAC): A Meridional Magnetometer Chain for Magnetospheric Sounding, Proceedings of the Enviroment Modeling Workshop, June 17-22, 2005, Snowmass, Colorado, USA.

Currenti G., Del Negro C., Lapenna V. and Telesca L., 2005, Multifractality in local geomagnetic field at Etna volcano, Sicily (southern Italy). *Nat. Hazards Earth Syst. Sci*. (NHESS), 5, 555-559.

Enomoto Y., Hashimoto H., Shirai N., Murakami Y., Mogi T., Takada M., Kasahara M., 2006, Anomalous geoelectric signals possibly related to the 2000 Mt. Usu eruption and 2003 Tokachi-Oki earthquakes. *Physics and Chemistry of the Earth,* 31, 319–324.

Espinasa-Pereña R., Martín-del Pozzo A.L., 2006, Morphostratigraphic evolution of Popocatépetl volcano, México, in: Siebe, C., Macías, J.L., Aguirre-Díaz, G. (eds.), Neogene-Quaternary continental margin volcanism: a perspective from México, Boulder, Colorado, Geol. *Soc. of America, Special Paper*, 402, 115-138.

Fujinawa Y., Matsumoto T., Iitaka H., Takahashi K., Nakano H., Doi T., Saito T., Kasai N., Sato S., 2006, Earliest detection of magma movements by measuring transient streaming potential. *Physics and Chemistry of the Earth,* 31, 223–233.

González-Pomposo G.J., 2004, Análisis de la sismicidad asociada a la actividad del volcán Popocatépetl y determinación de su estructura por medio de tomografía sísmica, PhD Thesis, Instituto de Geofísica, National University of Mexico, Mexico.

Gotoh K., Hayakawa M., Smirnova N. and Hattori K., 2004, Fractal analysis of seismogenic ULF emissions. *Phys. Chem. Earth*, 29, 419–424.

Hayakawa, M. and Fujinawa, Y. (Eds.), 1994, Electromagnetic Phenomena Related to Earthquake Prediction, Terra Sci. Pub. Co., Tokyo.

Hayakawa, M., (Ed.), 1999, Atmospheric and Ionospheric Electromagnetic Phenomena Associated with Earthquakes, TERAPPUB, Tokyo.

Juárez A., Gay C., Flores Y., 2005, Impact of the Popocatepetl's volcanic activity on the air quality of puebla City, Mexico. *Atmósfera*, 57-69.

Kotsarenko A., Pérez Enríquez R., López Cruz-Abeyro J.A., Koshova S., Grimalsky V., 2004, Analysis of the ULF electromagnetic emission related to seismic activity, Teoloyucan geomagnetic station, 1998-2001. *Natural Hazards and Earth System Sciences (NHESS),* Vol.4, P. 679–684.

Kotsarenko A., Valdez-Gonzalez C., López Cruz-Abeyro J.A., Pérez Enríquez R., Koshevaya S., Grimalsky V., 2005a, Seismogenic ULF EM emissions of volvano origin, observed at Tlamacas seismo-geomagnetic station, volvano Popocatepetl, Mexico, 2001-2004. International Workshop on Seismo Electromagnetics IWSE 2005, Programme and Extended Abstracts, 217-218.

Kotsarenko A., Molchanov O., Perez Enrıquez R., Lopez Cruz-Abeyro J. A., Koshevaya S., Grimalsky V., and Kremenetsky I., 2005b,

Possible seismogenic origin of changes in the ULF EM resonant structure observed at Teoloyucan geomagnetic station, Mexico, 1999– 2001. *Natural Hazards and Earth System Science*s *(NHESS)*, 5, 711–715.

Macías J.L., 2005, Geología e historia eruptiva de algunos de los grandes volcanes activos de México, *Boletín de la Sociedad Geológica Mexicana*, Tomo LVII, núm. 3, 379-424.

Macías Vázquez J.L., Carrasco Núñez G., Delgado Granados H., Martín Del Pozzo A.L., Siebe Grabach C., Hoblitt R.P., Sheridan M.F., Tilling R.I., 1995a, Mapa de peligros del volcán Popocatepetl, Instituto de Geofísica, UNAM, Mexico, 1995. http://tornado.cenapred.unam.mx/es/Instrumentacion/InstVolcanica/MVolcan/ImagenesMV olcan/mapaPeligrosA.jpg

Martin-Del Pozzo A.L., Cifuentes-Nava G. Cabral-Cano E., 2002, Volcanomagnetic signals during the recent Popocatepetl (Mexico) eruptions and their relation to eruptive activity. *J. Volc. Geoth. Res.*, 113, 415-428.

Mooser F., Montiel A., Zúñiga Á., 1996, Nuevo mapa geológico de las cuencas de México, Toluca y Puebla: México, D.F., Subdirección de Construcción, Comisión Federal de Electricidad México, D.F.

Siebe C., Macías J.L., Abrams M., Rodríguez-Elizarrarás R.S., Castro R., Delgado H., 1995, Quaternary Explosive Volcanism and Pyroclastic Deposits in East-Central México: Implications for Future Hazards. *Geol. Soc. of America*, 1, 1-48.

Siebe C. and Macías J., 2006, Volcanic hazards in the Mexico City metropolitan area from eruptions at Popocatépetl, Nevado de Toluca, and Jocotitlán stratovolcanoes and monogenetic scoria cones in the Sierra Chichinautzin Volcanic Field. Geological Society of America Special Papers, 402, 253–329.

Zúñiga R.D.M. and Valdés C., 2007, Se está formando una segunda cámara magmática en el Popocatepetl? Análisis de la variación espacial de los valores B bajo el edificio volcánico, *Geos,* 27 (1), 113, 2007, http://www.ugm.org.mx/raugm/docs/geos27-1b.pdf.

Geofísica Internacional (2019) 58-2: 113-126

Original paper

# Hydraulic parameters evaluation of the Pan-African aquifer by applying an alternative geoelectrical approach based on vertical electrical soundings

Zakari Arétouyap*, Dieudonné Bisso, Jorelle Larissa Méli'i, Philippe Njandjock Nouck, André Njoya and Jamal Asfahani

Received: September 04, 2017; accepted: January 01, 2019; published on line: April 01, 2019
DOI: http://dx.doi.org/10.22201/igeof.00167169p.2018.58.2.1964

**Resumen**

Para este estudio se realizaron cincuenta Sondeos Eléctricos Verticales (SEVs), de los cuales en 14 sitios se tenía información de muestreos de agua. Estos sondeos se interpretaron para determinar los parámetros hidráulicos del acuífero Pan-Africano en la región de Adamawa-Camerún, y estos fueron Transmisividad (T) y Conductividad Hidráulica (K). El enfoque utilizado es efectivo y aplicable a otras áreas similares, si se toman las suposiciones adecuadas. La resistencia transversal (RT) del acuífero oscila entre 24 y 31,350 Ω.m² con un promedio de 7476 Ω.m²; la resistencia transversal modificada (RTM) oscila entre 1526 y 28209 Ω.m² con un promedio de 7873 Ω.m²; la Transmisividad (T) oscila entre 4 y 17,4 m²/día con un promedio de 7.23 m²/día y una desviación estándar de 3.42 m²/día; y la Conductividad Hidráulica (K) varía de 0,07 a 0,74 m/día con una media de 0,31 m/día y una desviación estándar de 0,17 m/día.

Palabras clave: conductividad hidráulica, resistencia transversal modificada, transmisividad, resistencia transversal, Pan-Africano, mediciones *SEV*.

**Abstract**

The present article aims at determining hydraulic parameters of the Pan-African aquifer in the region of Adamawa-Cameroon, namely the transmissivity (*T*) and the hydraulic conductivity (*K*). For this, fifty vertical electrical soundings (*VESs*),including 14 performed near existing boreholes with known values of water resistivity, have been conducted in the region using the Terrameter ABEMSAS-1000 with a spacing of current electrodes (*AB*) varying from 2 to 600 m.The curve matching technique is used to set structural parameters then, an inverse technique algorithm fits both theoretical and field curves for each experimental. The transverse resistance *TR* and the transmissivity *T* for the interpreted 14 *VES* are computed, then used to establish two relationships: one between the modified transverse resistance (*MTR*) andthe transverse resistance (*TR*) and another between *MTR* and the transmissivity (*T*).This enabled to compute *MTR (*ranged from 1526 to 28209 Ω.m² with an average of 7873 Ω.m²),*TR (*ranged from 24 to 31350 Ω.m² with an average of 7476 Ω.m²), *T* (ranged from 4 to 17.4 m²/day with an average of 7.23 m²/day) and *K* (ranged from 0.07 to 0.74 m/day with an average of 0.31 m/day) values in the whole region. The approach used for this purpose is effective and exportable to other Pan-African regions in the world.

Key words: hydraulic conductivity, modified transverse resistance, transmissivity, transverse resistance, Pan-African, *VES* measurements.

Z. Arétouyap*
D. Bisso
J. Larissa Méli'i
P. Njandjock Nouck
Faculty of Science
University of Yaounde I, P.O. Box 812
Yaounde, Cameroon
*Corresponding author: aretouyap@gmail.com

A. Njoya
Institute of Fine Arts
University of Dschang, P.O. Box 32
Foumban, Cameroon

J. Asfahani
Geology Department
Atomic Energy Commission, P.O. Box 6091
Damascus, Syria

## Introduction

Because of its relatively better quality (compared to surface water) and its potential ubiquity, groundwater plays a very important role in water resources management policies. However, aquifers that provide groundwater are mostly characterized among others by the hydraulic conductivity (Arétouyap *et al*., 2015). Indeed, the modelling and the behaviour of the groundwater during the upcoming exploitation strongly depend on this parameter as it informs us about the recharge capacity of the aquifer (Asfahani, 2007).

Nowadays, because of the imprecision and the low efficiency of the traditional methods of pumping test, geo-electrical methods are increasingly used since the late 70s through the world to model and predict groundwater behavior during the upcoming exploitation (Kelly, 1977). Jones and Bufford (1951) and Croft (1971) established a sound relationship between permeability and formation factor. Similar relationships were established between resistivity and well productivity (Vincenz, 1968), transmissivity and transverse resistance (Ungemach *et al*., 1969), saturated thickness resistivities and hydraulic conductivities (Kelly,1977), aquifer transmissivity and transverse resistance (Mazáč and Landa, 1979). Scarascia (1976) estimated the transmissivity through interpreting the electrical soundings in Italy. Asfahani (2007) applied the vertical electrical soundings technique to characterize the Neogene aquifer (Salamiyeh region in Syria) in terms of hydraulic conductivity, transmissivity, transverse resistance and thickness. Tahmasbi-Nejad (2009) and Anomohanran (2013) used also this resistivity method to study the water potential in areas of Behbahan-Azad (Iran) and Ukelegbe (Nigeria) respectively. Asfahani (2016) used surficial vertical electrical sounding technique (VES) to compute the aquifer hydraulic conductivity. Those alternative approaches have been successfully applied for characterizing the transmissivity of the Quaternary and Paleogene aquifers in the semi-arid Khanasser valley region (Northern Syria), and for determining the hydrodynamic parameters of the Pan-African aquifer in the Adamawa-Cameroon region (Arétouyap *et al*., 2015).

More recently, Asfahani (2016) developed a new practical and easy approach for computing the hydraulic conductivity of aquifer by taking into consideration only the groundwater salinity. The main objectives of the present paper are therefore the following:

1. to check the efficiency and the effectiveness of the recent Asfahani (2016)'s method, by applying his approach in another region than Syria;

2. to use his method to locate and characterize local aquifers in terms of hydraulic conductivity and in order to re-compute the hydraulic parameters of the Pan-African aquifer in the Adamawa-Cameroon region;

3. to compare the results of hydraulic conductivity and the transmissivity obtained by Asfahani's approach with those obtained previously.

## Previous geophysical research

In hydrological terms, 150 to 300 km wide, the Adamawa plateau is called "the water tower of the region" because it feeds three of the four major watersheds of the country. The most recent hydrogeophysical survey conducted in the region (Arétouyap *et al*., 2015) enabled to infer major hydrodynamic parameters of the local aquifers. It revealed that almost all of them are made of the fractured portion of the granitic bedrock located at a depth ranging between 7 and 84 m, the thickness between 1 and 101 m, the resistivity between 3 and 825 Ω.m, the hydraulic conductivity between 0.012 and 1.677 m/day, the transmissivity between 0.46 and 46.02 m²/day, and the product $K\sigma$ between $2.1\times10^{-4}$ and $4.2\times10^{-4}$. Those results were derived from an empirical relationship established by Arétouyap *et al*. (2015) between the aquifer resistance $R$ and the product $K\sigma$, in a region considered as a single uniform geological unit.

## Geomorphology and hydrogeology of the Adamawa Plateau

This study is conducted in the Adamawa-Cameroon region, located in the heart of Central Africa between 6° -8° north and 11° -16° east (Figure 1). The study region extends over a length of about 410km from west to east between the Federal Republic of Nigeria and the Central African Republic, with an area of 6782 km$^2$. The morphology of the region is of volcanic highlands, resulting from tectonic uplift and subsidence accompanied by intense magmatic emissions (Vincent, 1970; Tchameni *et al*., 2001). Although the average altitude is 1100 m, this region of a rugged terrain is limited at the North by a large cliff and an uneven escarpment of several hundred meters that dominates the area.

The center of the plateau is marked by soft forms barely accented and swampy valleys, dotted with mountains or/and volcanic cones. At the East, there are massifs resulting from the former erosion and tectonic movements around the regions of Meiganga and Bagodo. In the West, the terrain is mountainous with hills. Volcanic inheritance covers the North, the East and the South areas. One notes the presence of an assembly line which occupies an important part of the region, reaching altitudes greater than 2240 m at Mount Tchabal-Mbabo. There are also plains and basins such as the Tikar plain in the Mayo-Banyo division. The southern part is characterized by a huge plateau that gradually drops until the penepla in Djerem (Toteu *et al*., 2000).

The geological history of the Adamawa-Cameroon region is marked by three major events (Toteu *et al*., 2000):

- A long period of continental erosion from Precambrian to Cretaceous;

- The onset of volcanism from Cretaceous to Quaternary;

- Recurrent basement tectonics that explain the horst and graben structure of the region.

An investigation of superficial formations in the region has highlighted the Pan-African granite-gneiss basement, represented by Ordovician granites, gneisses and Pan-African migmatites. The main geological units present inthe study region are basalts, trachytes and trachyphonolites based mostly on concordant ttcalco-alkaline granites and discordant alkaline granites (Toteu *et al*., 2000). The presence of metadiorites of Paleoproterozoic basement it is also observed (Toteu *et al*., 2001). According to the same authors, major fractures of the Pan-African bedrock fall into two main directions:

- The most common direction oriented N 30 °E, is that of the "volcanic line of Cameroon";

- The second directed N 70 °E, corresponds to the "line of Adamawa" or "Adamawa shear zone".

Geophysical surveys revealthat the bedrock of the study area is intensely faulted (Robain *et al*., 1996; Cornacchia and Dars, 1983; Dumont, 1986; Njonfang *et al*., 2008; Toteu *et al*., 2004). Such tectonic activities augur potential existence of groundwater in the region. However, apart from Arétouyap *et al*. (2015) that considered the whole region as a single geological unit, there is no recent study

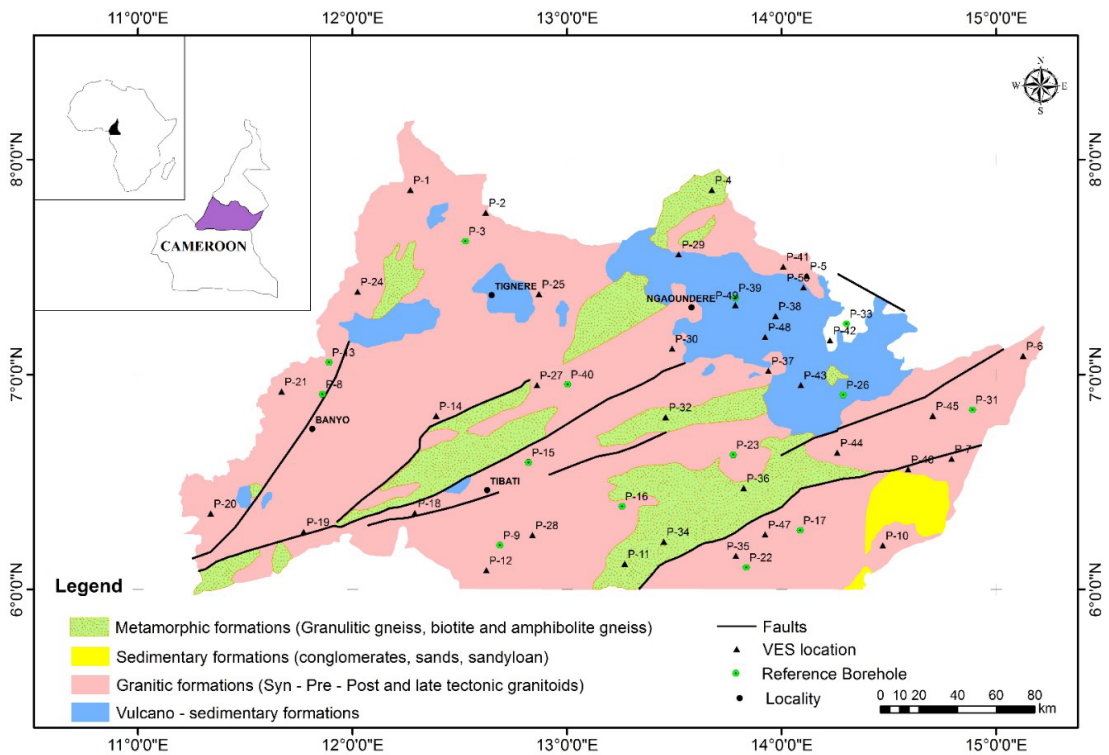


**Figure 1.** Geological map of the study area, with the locations of VES measurements (Maréchal, 1976) as amended.

to locate and characterize the local aquifers. This situation justifies the interest of the present paper.

## Methodology

*VES data recording and interpretation*

A vertical electrical sounding (VES) with Schlumberger configurationis conducted in the region in order to locate and characterize the aquifers in the study region. With this technique, the electrical resistivity variations are expressed as a function of depth. Fifty vertical electrical soundings (*VES*) including 14 with available water samples have been conducted in the region using the Terrameter ABEMSAS-1000 with a spacing of current electrodes (*AB*) varying from 2 to 600 m.

In the present research, the curve matching technique is used to set structural parameters (Orellana and Mooney, 1966). Then, an inverse technique algorithm developed by Zohdy (1989) and Zohdy and Bisdorf (1989) fits both theoretical and field curves for each experimental. Dey and Morrison (1979) mentioned the possibility of considering and assuming the medium to be as a one-dimensional model (1D). The geological conditions in the study area were favorable and allowed us to assume and apply the 1D model. The 1D quantitative interpretation of the 50 VES has already enabled the identification of geoelectrical characteristics of the Pan-African deposits (Arétouyap *et al*., 2015).

*Hydraulic conductivity estimation*

This section is the main core of the survey. The hydraulic conductivity is estimated by using the approach proposed by Asfahani (2016), which consists of the seven steps reminded below.

*Determination of the water resistivity $\rho_w$*

14 experimental VES measurements are carried out in the vicinity of available water samples(boreholes in function). Values of water conductivity ($\sigma_w$)from those 14 available water samples are measured, their water resistivity ($\rho_w$) values are thereafter deduced by using equation 1.

$$\rho = {}^{1}/_{\sigma_w} \quad (1)$$

Hence, the factor formation (*F*) used in Archie's law becomes a function of both $\sigma_w$ and ($\rho_w$).

Those 14*VESs* have been quantitatively interpretedusing curve matching method (as illustrated in Figure 2), where the resulting resistivity ($\rho_{rock}$) and thickness (*h*) values are shown in Table 1.

*Determination of the formation factor*

The formation factor (*F*) used in Archie's law (Worthington, 1993) is computed as the ratio of $\rho_{rock}$ and $\overline{\rho}_w$ (Equation 2).

$$F = \frac{\rho_{rock}}{\overline{\rho}_w} \quad (2)$$

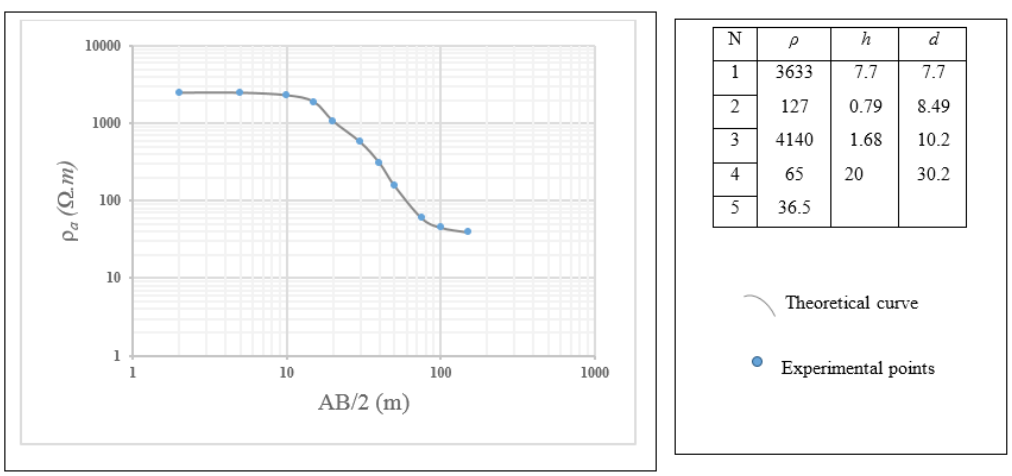


| N | $\rho$ | $h$ | $d$ |
|---|---|---|---|
| 1 | 3633 | 7.7 | 7.7 |
| 2 | 127 | 0.79 | 8.49 |
| 3 | 4140 | 1.68 | 10.2 |
| 4 | 65 | 20 | 30.2 |
| 5 | 36.5 | | |

**Figure 2.** An illustration of CMM interpretation of VES measurements.

In this Equation (2), $\rho_{rock}$ represents the saturated aquifer resistivity estimated from the quantitative interpretation (using curve matching method as illustrated above) of *VES*, and $\overline{\rho}_w$ is the average pore fluid resistivity for the 14 reference VES. Water resistivity $\rho_w$ is obtained through converting water conductivity $\sigma_w$ since the conductivity is the inverse of the resistivity (see Equation 1).

*Computation of the corresponding hydraulic conductivity*

The formation factor *F* obtained previously using *VES* method is related to the hydraulic conductivity (Salem, 1999) as expressed by equation 3.

$$K\,(m/day) = 0.66528 \times F^{2.09} \qquad (3)$$

*Estimation of the transverse resistance and the transmissivity for the 14 experimental VES*

The transverse resistance *TR* and the transmissivity *T* for the interpreted 14 *VES* are computed using Equations 4 and 5.

$$TR = \rho_{rock} \times h \qquad (4)$$

$$T = \overline{K} \times h \qquad (5)$$

where $\overline{K}$ is the average value of hydraulic conductivity of the available 14 water samples shown in Table 1.

*Expressing the MTR as a function of TR*

The modified transverse resistance (*MTR*) is expressed by Equation 6 (Niwas and Singhal, 1985).

$$MTR = \mathrm{TR}\,\frac{\rho_w}{\overline{\rho}_w} \qquad (6)$$

Where $\overline{\rho}_w$ is the average water resistivity of the available fourteen water samples shown in Table 1, and $\rho_w$ is the water resistivity at the location of the *VES* point (Table 1). Knowing $\overline{\rho}_w$ and $\rho_w$, *MTR* for the 14 *VES* points is plotted versus *TR* (Figure3).

This plot enabled to establish an empirical relationship between both parameters (equation 7).

$$MTR = 0.8518\ TR + 1505.6 \qquad (7)$$

With $R^2$ = 0.8447

Equation 9 will be used to extrapolate *MTR* values at the remaining *VES* points where no water sample exists.

*Expressing T as a function of MTR*

The transmissivity *T* is expressed as a function of the modified transverse resistance *MTR* (Equation 8) thanks to the plot (Figure 4).

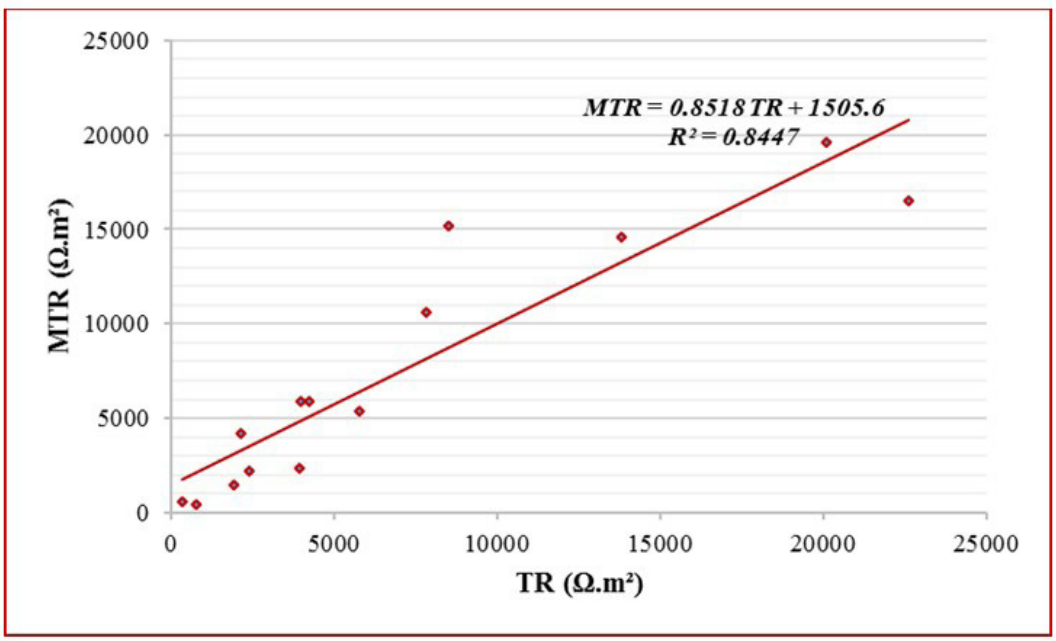


**Figure 3.** *MTR* expressed as a function of *TR* for a suitable empirical relationship purpose.

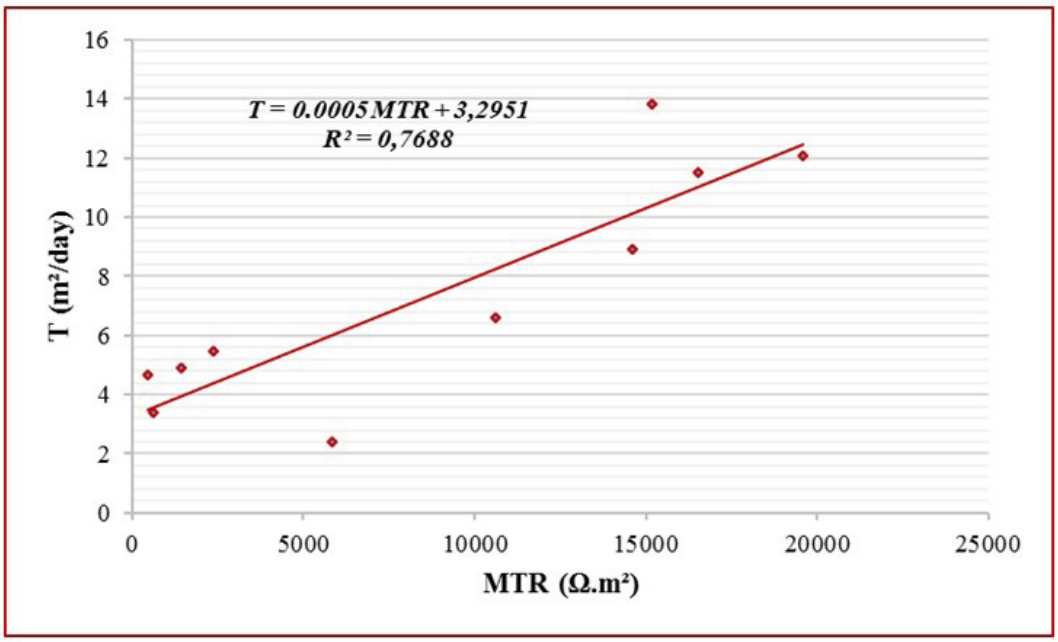


**Figure 4.** *T* expressed as a function of *MTR* in order to establish an empirical relationship between both parameters.

$$T = 0.0005\ MTR + 3.2951 \qquad (8)$$

With $R^2$ = 0.7688

Equation 10 will be used to extrapolate *T* values at the remaining 36 *VES* points where no water sample exists.

*Extrapolation of T in the whole region*

In order to estimate *MTR* values in the remaining 36 VES points without water sample, the formula established in equation (7) is applied. Equation 8 is thereafter used to compute *K* values in those VES without water sample. In other terms, since the transverse resistance of each point is known (as the product of rock resistivity by its thickness as expressed by earlier Equation 5) from VES interpretation, the empirical relationship established in Equation 7 enables us to obtain the modified transverse resistance as the product of the transverse resistance by 0.8518 plus 1005.6. Finally, the transmissivity of each point is obtained as the product of the modified transverse resistance by 5 x $10^{-4}$ plus 3.2951. This methodology takes into account the geological context of the study area as exposed in Section 3.

## Results and discussion

This geoelectrical investigation consisted in applying the approach developed and proposed recently by Asfahani (2016) on 14 reference *VES*, then using the above calibrated relationships established to extrapolate aquifer parameters in the whole study area. Two relationships have been established: one between *MTR* and *TR* (Equation 7), and another between *T* and *MTR* (Equation 8). Those relationships were established assuming that the study area is geologically homogeneous and regular.

*Hydrogeophysical parameters of 14 reference VES*

Fourteen *VES* were conducted near existing boreholes with available water samples. Interpretation of those *VES* enabled to compute rock resistivity ($\rho_{rock}$) and aquifer thickness (*h*) at those points. The corresponding transverse resistance (*TR*), modified transverse resistance (*MTR*), formation factor (*F*) and hydraulic conductivity (*K*) are thereafter computed since the expression of water resistivity ($\rho_w$) is known. These parameters are represented in Table 1.

Those 14 reference boreholes have an average value of water resistivity $\overline{\rho}_w$ = 3.0 Ω.m and an average value of hydraulic conductivity $\overline{K}$ = 0.29 m/day. Those average values have been used respectively to compute *MTR* and *T*. Geophysical and hydrogeological parameters of those 14 reference *VES* points are summarized in Table 2.

**Table 1**. Hydrological and geophysical parameters of 14 reference *VES.*

| VES | $\rho_{rock}$ (Ω.m) | $\rho_w$ (Ω.m) | h (m) | TR (Ω.m²) | MTR (Ω.m²) | F | K (m/day) | T (m²/day) |
|---|---|---|---|---|---|---|---|---|
| P-3 | 472.0 | 2.03 | 8.4 | 3964.8 | 5856.5 | 157.4 | 0.62 | 2.4 |
| P-8 | 134.0 | 3.21 | 43.0 | 5762.0 | 5382.5 | 44.7 | 0.09 | 12.4 |
| P-9 | 207.0 | 5.01 | 19.0 | 3933.0 | 2354.0 | 69.0 | 0.09 | 5.5 |
| P-13 | 177.0 | 1.68 | 48.0 | 8496.0 | 15164.2 | 59.0 | 0.23 | 13.8 |
| P-15 | 112.9 | 4.01 | 17.0 | 1919.3 | 1435.2 | 37.7 | 0.55 | 4.9 |
| P-16 | 46.0 | 1.51 | 46.0 | 2116.0 | 4202.0 | 15.3 | 0.12 | 13.2 |
| P-17 | 446.0 | 2.84 | 31.0 | 13826.0 | 14598.0 | 148.7 | 0.89 | 8.9 |
| P-22 | 341.0 | 2.22 | 23.0 | 7843.0 | 10593.6 | 113.7 | 0.13 | 6.6 |
| P-23 | 48.0 | 5.21 | 16.2 | 777.6 | 447.5 | 16.0 | 0.22 | 4.7 |
| P-26 | 110.8 | 2.15 | 38.0 | 4210.4 | 5872.2 | 37.0 | 0.56 | 10.9 |
| P-31 | 565.0 | 4.10 | 40.0 | 22600.0 | 16528.7 | 188.4 | 0.09 | 11.5 |
| P-33 | 479.0 | 3.08 | 42.0 | 20118.0 | 19586.1 | 159.7 | 0.19 | 12.1 |
| P-39 | 28.0 | 1.64 | 11.8 | 330.4 | 604.1 | 9.3 | 0.09 | 3.4 |
| P-40 | 40.0 | 3.29 | 60.0 | 2400.0 | 2187.4 | 13.3 | 0.16 | 17.3 |

**Table 2.** Averaged statistical hydraulic and geophysical parameters of the 14 reference *VES* points presented in Table 1.

| Parameter | Min | Max | Average |
|---|---|---|---|
| *h* (m) | 8.40 | 60.00 | 31.67 |
| $\rho_{rock}$ (Ω.m) | 28.00 | 565.00 | 229.05 |
| $\rho_w$ (Ω.m) | 1.51 | 5.21 | 3.00 |
| *F* | 9.34 | 188.42 | 76.39 |
| *TR* (Ω.m²) | 330.40 | 22600.00 | 7021.17 |
| *MTR* (Ω.m²) | 447.54 | 19587.12 | 7486.57 |
| *K* (m/day) | 0.09 | 0.89 | 0.29 |
| *T* (m²/day) | 2.42 | 17.27 | 9.12 |

*Hydrogeophysical parameters of 36 remaining VES without available water sample*

*MTR* ant *T* at the 36 *VES* points without available water samples are obtained using the established empirical Equations 7 and 8. The resulting *MTR*, *T*, and *K* values enable to approximately characterize the Pan-African aquifer. Those values are presented and compared with previous results (Arétouyap *et al*., 2015) as shown in Table 3. Significant changes between those results are visible in hydraulic conductivity and transmissivity values. This difference attests the necessity and the advantage of using this alternative approach, where salinity variations from place to place are taken into consideration.

**Table 3.** Hydrological and geophysical parameters of the 36 *VES* points without available water samples, in comparison with previous results (Arétouyap *et al*., 2015).

| VES | *h* (m) | $\rho$ (Ω.m) | TR (Ω.m²) | MTR (Ω.m²) | T (m²/day) | T* (m²/day) | K (m/day) | K*(m/day) |
|---|---|---|---|---|---|---|---|---|
| P-1 | 25 | 811.0 | 20275.0 | 18775.85 | 12.68 | 26.62 | 0.51 | 1.06 |
| P-2 | 47 | 362.1 | 17018.7 | 16002.13 | 11.30 | 39.25 | 0.24 | 0.84 |
| P-4 | 48 | 175.7 | 8433.6 | 8689.34 | 7.64 | 8.09 | 0.16 | 0.17 |
| P-5 | 20 | 608.0 | 12160.0 | 11863.49 | 9.23 | 16.93 | 0.46 | 0.85 |
| P-6 | 6 | 157.0 | 942.0 | 2308.00 | 4.45 | 10.06 | 0.74 | 1.68 |
| P-7 | 10 | 137.0 | 1370.0 | 2672.57 | 4.63 | 0.09 | 0.46 | 0.09 |
| P-10 | 19 | 114.1 | 2167.9 | 3352.22 | 4.97 | 28.40 | 0.26 | 1.49 |
| P-11 | 40 | 410.0 | 16400.0 | 15475.12 | 11.03 | 48.60 | 0.28 | 1.21 |
| P-12 | 37 | 22.0 | 814.0 | 2198.97 | 4.40 | 43.25 | 0.12 | 1.17 |
| P-14 | 8 | 8.0 | 64.0 | 1560.12 | 4.08 | 1.87 | 0.51 | 0.23 |
| P-18 | 43 | 408.0 | 17544.0 | 16449.58 | 11.52 | 38.71 | 0.27 | 0.90 |
| P-19 | 34 | 26.0 | 884.0 | 2258.59 | 4.42 | 6.91 | 0.13 | 0.20 |
| P-20 | 61 | 188.0 | 11468.0 | 11274.04 | 8.93 | 13.76 | 0.15 | 0.23 |
| P-21 | 19 | 221.5 | 4208.5 | 5090.40 | 5.84 | 42.63 | 0.31 | 0.55 |
| P-24 | 17 | 112.9 | 1919.3 | 3140.46 | 4.87 | 3.29 | 0.29 | 0.33 |

For each *VES* point presented in Table 3, the *K** value of the hydraulic conductivity can be obtained as a ratio of the transmissivity *T* to the saturated thickness *h* obtained at that point. The spatial distribution of *h* is shown in Figure 5, where its values range from 6 to 84 m, with an average of 32 m.

The spatial distribution of the transverse resistance (*TR*) shown in Figure 6 reveals that *TR* values range from 330 to 22600 Ω.m² with an average value of 7021 Ω.m².

The distributions of the modified transverse resistance (*MTR*), transmissivity (*T*) and hydraulic conductivity (*K*) are also shown respectively in Figures 7, 8 and 9, and summarized in Table 4. Many similitudes are observed between *TR* distribution (Figure 6) and MTR distribution (Figure 8). Respective minimum and maximum values are located in the same regions. However, one can observe a minor dissimilarity in the variation rate and direction. This change can be explained by several factors as electric anisotropy, mineralogical variation, hydraulic anisotropy and lithological disparity. Furthermore, since the local aquifer results from the bedrock alteration/weathering, it is possible to have many mini aquifers confined in unconnected aquitards.

The transmissivity distribution shown in Figure 9 exhibits the existence of a poor-transmissive zone in the eastern part of the study area. Transmissivity values are low in this area contrary to the west and the center, where values can reach 17 m²/day. The presence of sedimentary formations can explain the easy spread of water in horizontal direction unlike the western area, covered by surficial granite.

However, it is important to note that hydraulic conductivity *K* varies in the opposite sense to transmissivity. Indeed, higher *K* values are observed eastward while lower ones are observed westward (Figures 8 and 9). This distribution can also be explained by the geological and lithological setting as in transmissivity distribution. On the other hand, the inverse proportion between hydraulic conductivity (derived from vertical flow) and transmissivity (derived from horizontal) can be due to the presence of vertical faults and lineaments in the region.

Transmissivity and hydraulic conductivity of the Pan-African aquifer are determined through the proposed alternative approach (Asfahani, 2016). However, the application of this approach recommends the respect of three fundamental principles:

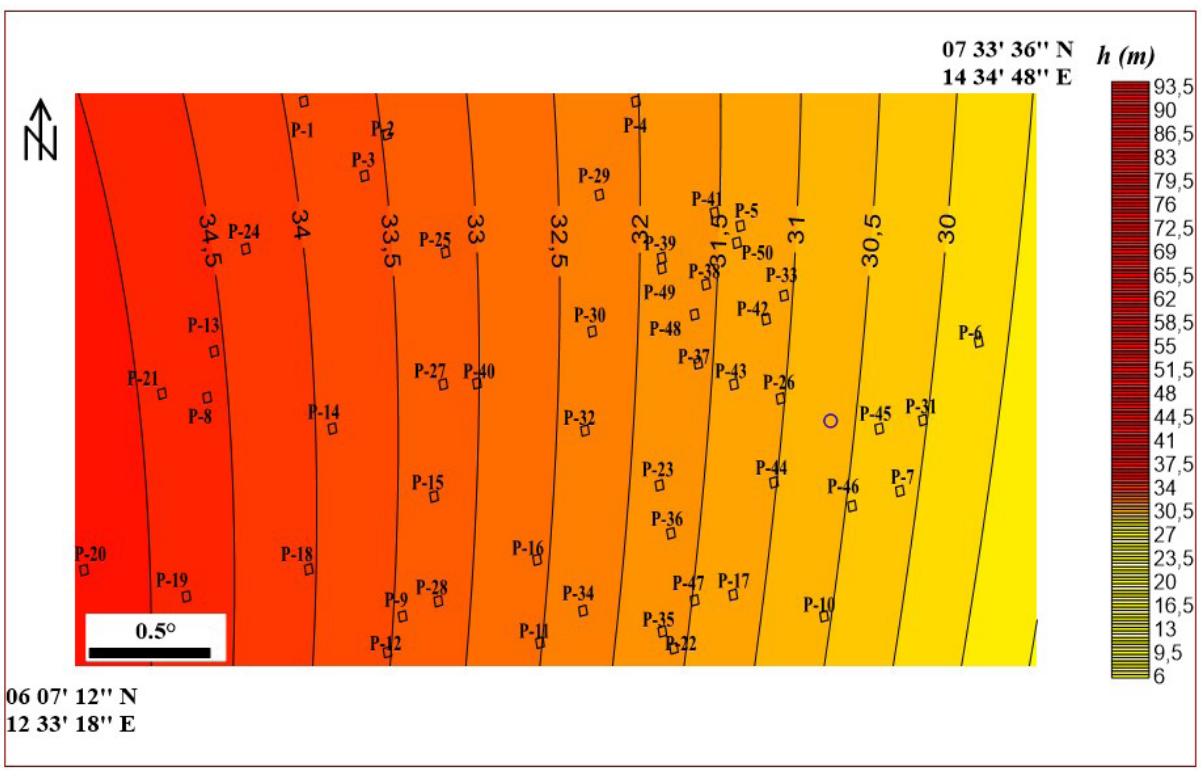


**Figure 5.** Thematic map of the Pan-African thickness.

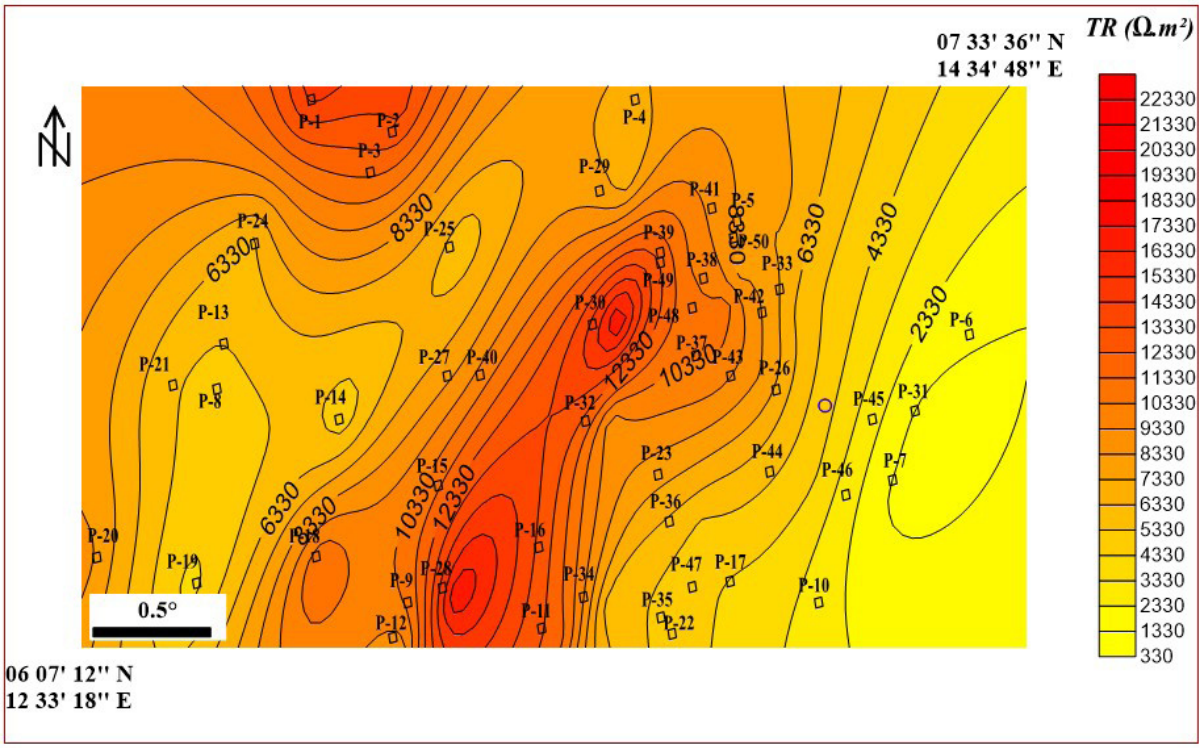


**Figure 6.** Thematic map of the Pan-African transverse resistance.

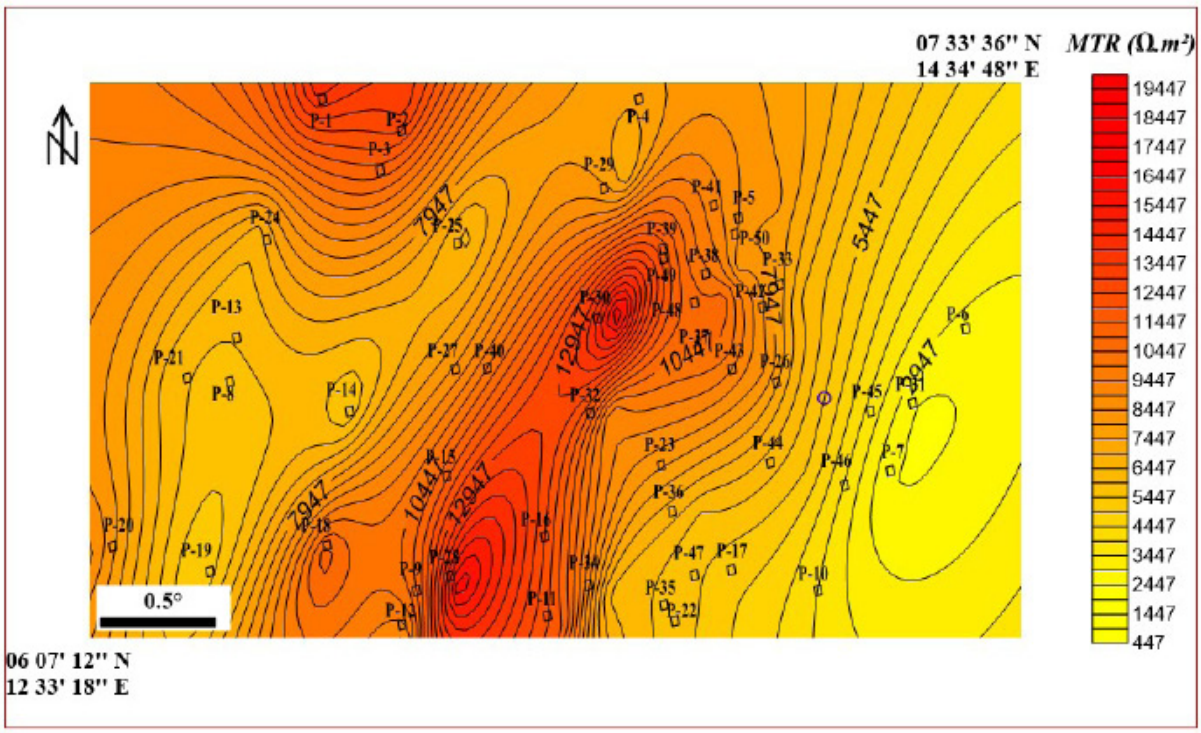


**Figure 7.** Thematic map of the Pan-African modified transverse resistance MTR.

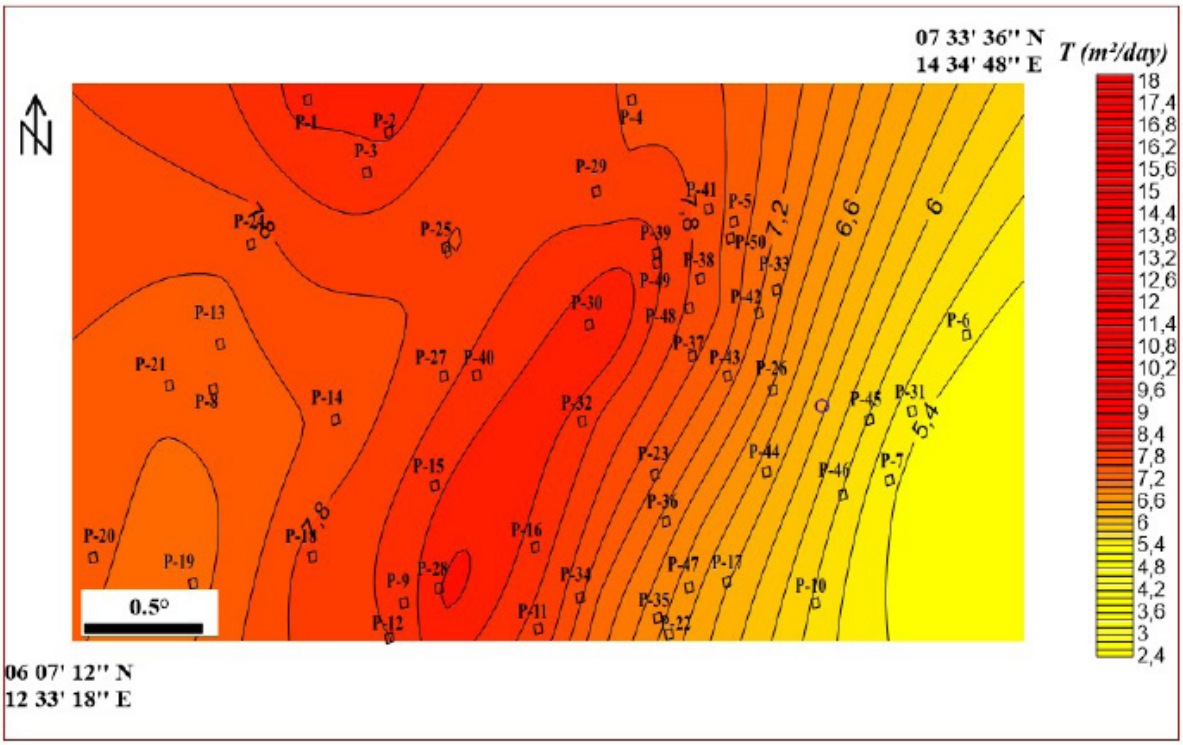


**Figure 8.** Thematic map of the Pan-African transmissivity.

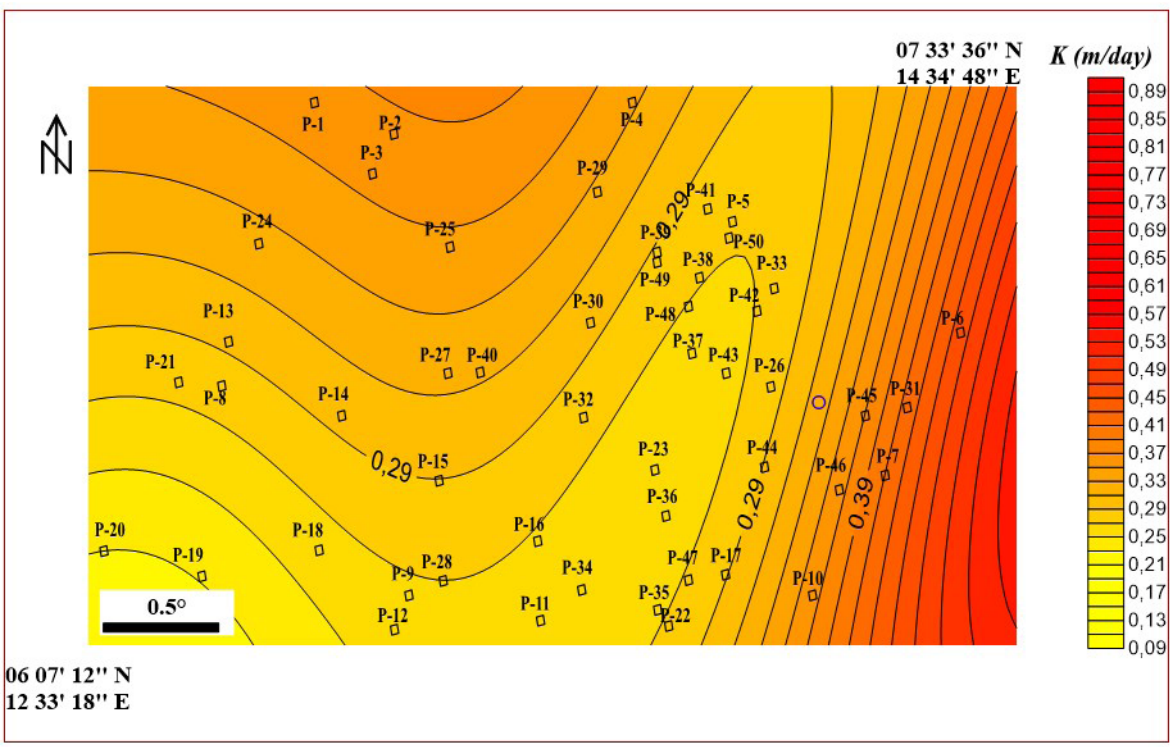


**Figure9.** Thematic map of the Pan-African hydraulic conductivity.

**Table 4.** Statistical hydraulic and geophysical parameters of the 36 *VES* points without available water samples.

| Parameter | Min | Max | Average | SD |
|---|---|---|---|---|
| *h* (m) | 6 | 98 | 32.08 | 21.49 |
| $\rho_{rock}$(Ω.m) | 3 | 825 | 225.21 | 222.18 |
| *TR* (Ω.m²) | 24 | 31350 | 7476.20 | ---- |
| *MTR* (Ω.m²) | 1526.04 | 28209.53 | 7873.83 | 6844.31 |
| *K* (m/day) | 0.07 | 0.74 | 0.31 | 0.17 |
| *T* (m²/day) | 4.06 | 17.40 | 7.23 | 3.42 |
| *TR* (Ω.m²) | 24 | 31350 | 7476.20 | ---- |
| *MTR* (Ω.m²) | 1526.04 | 28209.53 | 7873.83 | 6844.31 |

1. Where there are water samples (the case of 14 reference *VES* points presented in Table 1), the hydraulic conductivity *K* is firstly estimated by such an alternative approach, while the transmissivity *T* is secondly computed by assuming an average constant hydraulic conductivity and a variable thickness *h* of the saturated aquifer.

2. Where there are no available water samples (e.g. 36 *VES* presented in Table 3), the transmissivity is firstly estimated by the proposed approach, while the hydraulic conductivity is secondly computed.

3. A field hydrogeological investigation should be conducted in order to estimate the uncertainty and the confidence level of this new proposed approach in the study area.

The first two rules are followed. In addition, the results obtained are compared with those of Arétouyap *et al*. (2015). This comparison shows a fairly good agreement between the values of the aquifer thickness and a slight agreement regarding the values of hydraulic conductivity and transmissivity (Figure 10). Those differences are due to the basis of the analysis method. In the previous study, Arétouyap *et al*. (2015) used an empirical linear relationship between *Kσ* and the resistance *R* of the aquifer, where *K* and *σ* represent the hydraulic conductivity and the electrical conductivity of the aquifer respectively. Yet in the present investigation, the aquifer hydraulic conductivity is the ratio of the transmissivity to the saturated thickness. Note that transmissivity values are derived from modified transverse resistance computed thanks to an empirical relationship between *MTR* and *T*. Furthermore, the present study has increased the number of reference boreholes, top to 14.

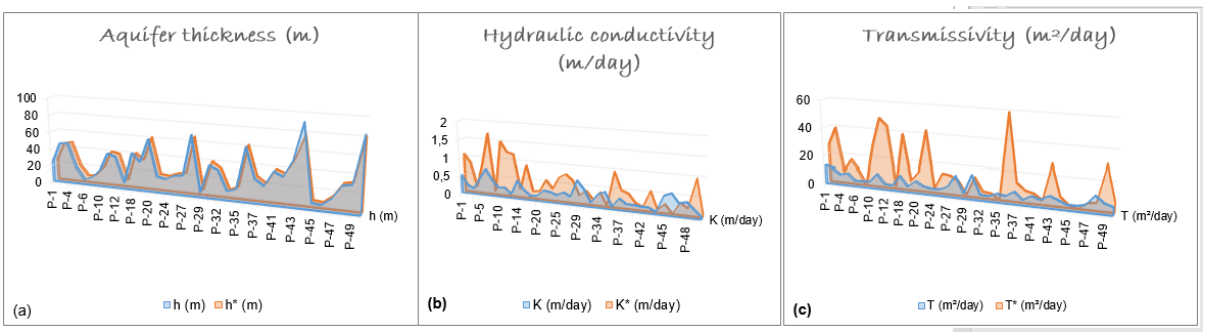


**Figure 10.** Comparison between aquifer parameters obtained respectively from former approach and newer one.

## Discussion

*Validation of the approach*

The equation used to determine hydrodynamic parameters from this approach isan empirical relationship (Table 3). In order to assess its reliability, the values of transmissivity obtained experimentally from pumping tests and those computed analytically using equation 8, as shown in Table 5, we compared.

This comparison shows an absolute random ranging from 0.003 to 1.576 with an average value of 0.38, which is bearable. Thus, this method that has already been proven inthe Quaternary and Paleogene aquifers in the semi-arid Khanasser valley region of Northern Syria (Asfahani, 2016) can also be used in the Pan-African context.

*Further conditions on the approach*

Since *VES* results are highly influenced by electrical noise, land use and other economic activities such as agriculture, livestock, tannery etc., measurements may be carried out in locations far away from any electrical line from several anthropogenic activity centers. *K* values are generally influenced. In order to mitigate such negative impacts, *VES* measurements may be calibrated and their 1D quantitative interpretation must necessarily reflect the aquifer lithology. This is the case of *VES* measurements presented in the present study. Geostatistical analysis largely contributes in assuming that *VES* data are not influenced by electrical noise.

Contamination is another technical concern. The methodology proposed by Asfahani (2016) and applied in this paper is entirely based on water resistivity. Any contamination of that water may affect and modify its resistivity, and by consequence will affect the *K* values. This methodology must therefore be applied in a proper area, without any contamination influence. If this is not the case, the contamination factor and its influence on water resistivity must be calibrated and moved away. Fortunately, our study area is free of any relevant contamination.

## Conclusions

The transmissivity (*T*) and the hydraulic conductivity (*K*) of the Pan-African aquifer in the region of Adamawa-Cameroon have been determined using an alternative method based on *VES* interpretation. 14 experimental *VES* conducted in the vicinity of existing boreholes with known water resistivity are interpreted using curve matching method. This interpretation led to two mathematical laws (empirical equations). The first equation establishes a strong relationship between the

**Table 5.**Comparison of analytical and experimental values for the 14 existing boreholes.

| VES | T (m/day) | T#(m/day) | MTR (Ω.m²) | $\Delta T = \left\| \frac{T^{\#} - T}{T} \right\|$ |
|---|---|---|---|---|
| P-3 | 2.42 | 6.22 | 5856.52 | 1.57 |
| P-8 | 12.38 | 5.99 | 5382.48 | 0.52 |
| P-9 | 5.47 | 4.47 | 2353.97 | 0.18 |
| P-13 | 13.82 | 10.88 | 15164.20 | 0.21 |
| P-15 | 4.89 | 4.01 | 1435.20 | 0.18 |
| P-16 | 13.24 | 5.39 | 4201.97 | 0.59 |
| P-17 | 8.92 | 10.59 | 14597.97 | 0.19 |
| P-22 | 6.62 | 8.59 | 10593.60 | 0.29 |
| P-23 | 4.67 | 3.52 | 447.54 | 0.25 |
| P-26 | 10.94 | 6.23 | 5872.18 | 0.43 |
| P-31 | 11.51 | 11.56 | 16528.71 | 0.003 |
| P-33 | 12.09 | 13.09 | 19586.12 | 0.08 |
| P-39 | 3.39 | 3.59 | 604.10 | 0.06 |
| P-40 | 17.27 | 4.39 | 2187.41 | 0.75 |
| | Average | | | 0.38 |

#Analytical values obtained from the empirical equation 9

modified transverse resistance (*MTR*) while the second links the transmissivity (*T*) to *MTR*. From those equations, aquifer of the study is characterized as follows: *TR* ranges from 24 to 31350 Ω.m² with an average of 7476 Ω.m²; MTR ranges from 1526 to 28209 Ω.m² with an average of 7476 Ω.m²; *T* ranges from 4 to 17.4 m²/day with an average of 7.23 m²/day; and *K* ranges from 0.07 to 0.74 m/day with an average of 0.31 m/day. A cross validation, comparing *T* values obtained respectively from pumping test and developed approach (Table 5) reveals a fairly agreement between both sets of values. This approach is then suitable for investigation in the Pan-African context extended from Africa to South America.

**Acknowledgement**

The first author would like to thank Prof. I. Othman, General Director of the Syrian Atomic Energy Commission for allowing Prof. J. Asfahani to join the research team that conducted this investigation.The two reviewers are cordially thanked for their professional critics and remarks that improved considerably the final version of this paper.

**References**

Anomohanran, O., 2013. Geophysical investigation of groundwater potential in Ukelegbe, Nigeria. Journal of Applied Sciences 13, 119-125.

Archie, E., 1942. The Electrical Resistivity Log as an Aid in Determining Some Reservoir Characteristics, vol. 8. Technical Publication 1422, Petroleum Technology. American Institute of Mining and Metallurgical Engineer, New York, USA.

Arétouyap, Z., Nouayou, R., NjandjockNouck, P., Asfahani, J., 2015. Aquifers productivity in the Pan-African context. Journal of Earth System Science,124(3): 527-539.

Asfahani, J., 2007. Neogene aquifer properties specified through the interpretation of electrical sounding data, Sallamiyeh region, central Syria. Hydrol. Process. 21, 2934-2943.

Asfahani, J., 2016. Hydraulic parameters estimation by using an approach based on vertical electrical soundings (VES) in the semi-arid Khanasser valley region, Syria. Journal of African Earth Sciences 117, 1-11.

Cornacchia, M., Dars, R., 1983. Un trait structural majeur du continent africain. Les linéaments centrafricains du Cameroun au Golfe d'Aden. Bulletin de la Société géologique de France 7, 101-109.

Croft, M.G., 1971. A method of calculating permeability from electric logs. In *US Geological Survey Staff, Geological Survey Research 1971;Chapter B*. US Geological.

Dey, H., Morrison, H., 1979. Resistivity modeling for arbitrarily shaped 3-D structures. Geophysics 44(4), 753.

Dumont, J.F., 1986. Identification par télédétection de l'accident de la Sanaga (Cameroun). Sa position dans le contexte des grands accidents d'Afrique centrale et de la limite nord du craton congolais. Géodynamique 1, 13-19.

Jones, P.H, and Bufford, T.B, 1951. Electric logging applied to groundwater exploration. *Geophysics* 16, 115-139.

Kelly, W. E. 1977. Geoelectric sounding for estimating aquifer hydraulic conductivity: Ground Water 15, 420-424.

Maréchal, A., 1976. Géologie et géochimie des ressources thermominérales du Cameroun. Doc ORSTOM 59**,** 169-176.

Mazáč, O. and Landa, I., 1979. On determination of hydraulic conductivity and transmissivity of granular aquifers by vertical electric sounding. Journal of Geological Sciences16, 123–139.

Niwas, S., Singhal, D.C., 1985. Aquifer transmissivity of porous media from resistivity data. Journal of Hydrology 82, 143-153.

Njonfang, E., Ngako, V., Moreau, C., Affaton, P., Diot, H., 2008. Restraining bends in high temperature shear zones: "The Central Cameroon Shear Zone", Central Africa. Journal of African Earth Sciences 52, 9-20.

Orellana, E., Mooney, H.M., 1966. Master Tables and curves for vertical electrical sounding over layered structures. Interciencia.

Robain, H., Descloitres, M., Ritz, M., Yene Atangana, J.Q., 1996. A multiscale electrical survery of a lateritic soil system of the rain forest of Cameroon. Journal of Applied Geophysics 47, 237-253.

Salem, H.S., 1999. Determination of fluid transmissivity and electric transverse resistance for shallow aquifers and deep reservoirs from surface and well-log electric measurements. Hydrological Earth System Sciences 3(3), 421–427.

Scarascia, S., 1976. Contributions of geophysical methods to the management of water resources. Geoexploration14, 265-266.

Tahmasbi-Nejad, 2009. Geoelectric investigation in the aquifer characteristics and groundwater potential in Behbahan Azad University farm, Khuzestan Province, Iran. Journal of Applied Sciences 9, 3691-3698.

Tchameni, R., Mezger, R., Nsifa, N.E., Pouclet, A., 2001. Crustal Origin of Early Proterozoïc Syenites in the Congo (Ntem Complex), South Cameroon. Lithos 57.

Toteu, S.F., Ngako, V., Affaton, P., Nnange, J.M., Njanko, T.H., 2000. Pan-African tectonic evolution in Central and Southern Cameroon: tranpression and transtension during sinistral shear movements. Journal of African Earth Sciences 36, 207-214.

Toteu, S.F., Van Schmus, W.R., Michard, A., 2001. New U-Pb and Sm-Nd data from North-Central Cameroun and its bearing on the pre-pan African history of Central Africa. Precambrian Res 180, 45-73.

Toteu, S.F., Penaye, J., Poudjom, Djomani, Y., 2004. Geodynamic evolution of the Pan-African belt in central Africa with special reference to Cameroon. Canadian Journal of Earth Sciences 41, 73-85.

Vincent, P.M., 1970. Conséquences tectoniques de la présence d'un métamorphisme crétacé au Cameroun, Annuaire Faculté des Sciences, Université de Yaoundé, Cameroun, 431-434.

Ungemach, P., Mostaghimi, F., Dupart, A., 1969. Essais de détermination du coefficient d'emmagasinement en nappe libre, application à la nappe alluviale du Rhin. Bulletin de l'Association Internationale d'Hydrologie Scientifique14, 169-190.

Vincenz, S.A., 1968. Resistivity investigations of limestone aquifers in Jamaica. *Geophysics* 33, 980-994.

Worthington, P.F., 1993. The uses and abuses of the Archie equations: the formation factor-porosity relationship. J Appl Geophys 30(3), 215–228.

Zohdy, A.A.R., 1989. A new method for the automatic interpretation of Schlumberger and Wenner sounding curves. Geophysics 54, 245–253.

Zohdy, A.A.R., Bisdorf, R.J., 1989. Schlumberger sounding data processing and interpretation program. US Geological Survey.

Geofísica Internacional (2019) 58-2: 151-168

Original paper

# Probabilistic seismic hazard analysis in La Paz-Los Cabos, Mexico: The importance of active Quaternary fault segments

Roberto Ortega*, Dana Carciumaru, Edahí Gutierrez, Eduardo Huesca–Pérez and Luis Quintanar

Received: August 01, 2018; accepted: January 23, 2019; published on line: April 01, 2019
DOI: http://dx.doi.org/10.22201/igeof.00167169p.2018.58.2.1967

**Resumen**

Se presenta un estudio de Análisis Probabilístico de Riesgo Sísmico (PSHA) en el sur de la Península de Baja California, México. En este estudio se analizó la contribución de segmentos de falla del Cuaternario que incluyen dos fallas que han sido consideradas potencialmente activas por algunos autores, pero inactivas por otros, que son las fallas de La Paz y San José. Se probaron varios escenarios para comparar la estimación del riesgo con la contribución de dichas fallas y finalmente se propuso un árbol lógico para añadir las mentidumbres epistemicas. Adicionalmente se escogieron tres presas situadas alrededor del área de estudio, La buena Mujer, La Palma y Santa Inés. Los valores máximos de aceleración del suelo (PGA) se compararon por 50, 100, 200 años al 10.5 y 2% de excedencia. La combinación de periodos con niveles de porcentajes de excedencia se usaron como referencia para distintos grados de riesgo. El modelo escogido se presenta en un árbol de riesgo PSHA clásico. Contrariamente a lo esperado, no parece muy importante incluir todas las fuentes sísmicas como las fallas de La Paz y San José en la determinación de riesgo de diseño ingenieril, ya que en la región las fallas características son insensibles a las relaciones bajas. Sin embargo es solo un artefacto de la decisión arbitraria de utilizar periodos de retorno como grado de protección. Los resultados muestran que en el caso de construcciones esenciales, 2% de probablilidades de excedencia en 200 años lo mejor para esta región. Es necesario realizar estudios poleosísmicos en esta región para saber si estas fallas geologicas son activas ya que muchas estructuras importantes se encuentran cerca de las fallas estudiadas.

Palabras clave: peligro sísmico, sur de Baja California, atenuación sísmica.

**Abstract**

A study of Probabilistic Seismic Hazard Analysis (PSHA) in the southern part of the Baja California Peninsula, Mexico is presented. In this study, the contribution of Quaternary fault segments are analyzed including two faults that have been considered potentially active by some authors, but inactive by others, namely, La Paz and San José faults. Therefore, different scenarios were tested to compare the hazard estimation with the contribution of these faults and finally a logic tree was proposed to add the epistemic uncertainties. In addition, three dams situated around the study area were chosen: La Buena Mujer, La Palma and Santa Ines. The peak ground acceleration values (PGA) were compared for 50, 100 and 200 years at 10, 5 and 2% of exceedance. The combinations of periods with percentages of levels of exceedance were used as reference for different degrees of hazard assessments. The preferred model is presented in a classical PSHA logic tree. Contrary to expectations, it seems that it is not so important to include all the seismic sources as La Paz and San José faults in hazard assessment of engineering design because in this region the characteristic faults are not sensitive for lower rates. However, this is only a mere artifact of the arbitrary decision of using return periods as a degree of protection. The present results show that in the case of essential facilities 2% probability of exceedance in 200 years is the best for this specific region. It is necessary to perform paleoseismic studies in this region, to know if these geological faults are active because many important structures are located close to the studied faults.

Key words: seismic hazard, southern Baja California, seismic attenuation.

R. Ortega*
D. Carciumaru
Centro de Investigación Científica
y de Educación Superior de Ensenada
Unidad La Paz. Miraflores 334
La Paz 23050 BCS, México.
*Corresponding author: ortega@cicese.mx

E. Gutierrez
E. Huesca–Pérez
CONACYT
Centro de Investigación Científica
y de Educación Superior de Ensenada
Unidad La Paz. Miraflores 334
La Paz 23050 BCS, México.

L. Quintanar
Instituto de Geofísica
Departamento de Sismología
Universidad Nacional Autónoma de México
Ciudad Universitaria
Delegación Coyoacán, 04510
CDMX, México.

## Introduction

The La Paz-Los Cabos region is an active tectonic zone with little historical seismicity reported, (Ortega and González, 2007). This article is a long-term effort, started in 1995 when a major earthquake struck the southern part of Baja California Peninsula. From 1996 to 1997 the Centro de Investigación Científica y de Educación Superior de Ensenada, Baja California (CICESE) deployed a local seismic network. Later, a temporary strong motion network was in operation from 1998 to 2007 (Munguía *et al*., 2006; Ortega and González, 2007). Recently, CICESE installed seismic broadband stations within and around La Paz Bay. For 15 years, seismicity and attenuation relations that are the basic parameters for seismic hazard analysis are been studied. In this work, a probabilistic seismic hazard analysis for the southern part of the Baja California Peninsula is presented.

Particularly, the seismic sources that have been a topic of active discussions are studied. There has been a long debate on whether some fault segments should be considered active or not. Of special importance are La Paz and San José faults because they are the most prominent features of the region. Therefore, all the fault segments that have been reported and mapped by the Mexican Geological Service (SGM, Servicio Geológico Mexicano) are presented. For example, some authors, (Cruz-Falcón *et al*., 2010; Munguía *et al*., 2006) have reported the existence of La Paz fault, whereas others, (Busch *et al*., 2006; Busch *et al*., 2007; Maloney *et al*., 2007; Ramos 1998) say this fault does not exist. In addition, a common problem is that there are several faults which cannot be identified with a unique name. The purpose of this work is to compare the seismic hazard in different scenarios: a) using all faults, b) without La Paz Fault (WLP) and c) without the San Jose Fault (WSJ). It is important to note that in this article active Quaternary faults only those faults that have exhibited an observed movement or evidence of seismic activity during the last 20,000 years are called.

## Tectonic setting

The Gulf of California is an oblique – divergent plate boundary with active transtensional continental rifting (Busby and Ingersoll, 1995). Strike slip and normal faults systems accommodate the deformation in this region (Angelier *et al*., 1981; Fletcher and Munguía, 2000; Umhoefer *et al*., 2002; Plattner *et al*., 2007). Right lateral strike slip faults marked the extremities of the Gulf of California and they are separated by short spreading centers. On the east side of the southern part of Baja California peninsula an array of onshore to offshore faults north striking exists, left stepping and east dipping known as system of gulf margin (Fletcher and Munguía, 2000) (Figure 1).

During the continental rifting (DeMets, 1995; Fletcher and Munguía, 2000; Plattner *et al*., 2007; Lizarralde *et al*., 2007), starts the onset of seafloor spreading in the southern part of the Gulf of California (Lizarralde *et al*., 2007); Umhoefer *et al*., 2008). In this region, the fault system development could be studied during the transition of rift to drift process, when ocean spreading begun and continental rifting is active. Along the Alarcon rise in the southern Gulf of California the spreading rate is slower than across plate boundary of the Pacific – North America, indicating that structures along with transform faults and spreading centers in the gulf could finally accommodate deformation in this region (DeMets, 1995; Fletcher and Munguía, 2000; Plattner *et al*., 2007).

The seismicity data (Munguía *et al*., 2006) and geomorphic relationships (Fletcher and Munguía, 2000; Busch *et al*., 2006, 2007; Maloney *et al*., 2007) show that the normal faults array rupturing the southern tip of Baja California peninsula are still active and act as a shear zone which contributes to translating the peninsula blocks away from mainland Mexico (Plattner *et al*., 2007). The gulf – border is an extensional zone as well as an area of decreasing elevation and thinning crust (Lizarralde *et al*., 2007). The topography of the southern tip of the Baja California peninsula is controlled by normal faults which produced moderate sized earthquake (Fletcher and Munguía, 2000), whereas the gulf margin fault array has a minor contribution to the plate divergence in the region. The faults delineate Quaternary basins and offset Quaternary alluvial deposits (Fletcher and Munguía, 2000; Busch *et al*., 2006, 2007; Maloney *et al*., 2007).

During the Cenozoic, the western part of North America at the latitude of Baja California was the place of a subduction zone, where Farallon plate was subducting beneath Western North America (Stock and Hodges, 1989; Hausback, 1984). During Farallon plate subduction (Figure 1a), the Pacific plate, located west of the Farallon plate met the North America plate (Atwater, 1970; Stock and Hodges, 1989) and stopped the subduction in the north beginning the development of the Mendocino and Rivera triple junction

along southern California and northern Baja California (Gorbatov and Fukao, 2005).

While Mendocino triple junction moved northward the Rivera triple junction went southward lengthening the right lateral transform plate boundary that had initiated between Pacific and North America plates (Stock and Hodges, 1989). This right–lateral system developed marked the early stages of San Andreas system (Atwater, 1970). Between 20 and 12 Ma a series of microplates was formed along Baja California. The microplates were located within the Pacific Plate, and the trench was developed in a right lateral fault zone, known as the Tosco-Abreojos fault (Stock and Hodges, 1989). Between 12 and 6 Ma normal faults with NNW and N trend, developed the east of the Tosco-Abreojos fault (Figure 1b) adjacent to the west of the current Gulf region from California (Stock and Hodges, 1989; Hausback, 1984; Umhoefer *et al*., 2002). The system of normal faults that dominates the margin of the gulf was part of the distribution of the deformation between the Gulf of California and the Tosco-Abreojos fault (Stock and Hodges, 1989), the gulf margin system was part of a complex system of transtensional faults from 12 Ma (Fletcher *et al*., 2007). The regime of oblique-divergence started about 6 ago Ma, when small rift basins began to form in the current Gulf of California (Figure 1c). This oblique – divergence regime began as transform faults separated by rift basins (Fletcher and Munguía, 2000; Oskin *et al*., 2001; Fletcher *et al*., 2007). Along Alarcon Rise, the southernmost spreading center in the Gulf of California, new ocean crust started forming (DeMets, 1995; Umhoefer *et al*., 2008). Nowadays, the Gulf of California continues to be an oblique divergent continental rifting (Fletcher and Munguía, 2000; Umhoefer *et al*., 2002; Mayer and Vincent, 1999; DeMets, 1995).

## Method

In this study, a classical approach for Probabilistic Seismic Hazard Analysis (PSHA) was used based on a three-step procedure (Cornell, 1968; Algermissen *et al*., 1990; Algermissen and Perkins, 1976; Bernreuter *et al*., 1989; Electric Power Research Institute, 1986). First, the seismicity parameters (*a* and *b* values) of the transform fault system were obtained. The Quaternary faults with low seismicity rate were also included using their annual rate of displacement obtained from independent studies. These faults were assumed to present a constant moment rate. Next, the attenuation relations were estimated using a simple omega-squared model based on a general regression of the maximum acceleration recorded versus distance. These attenuation relations for this region were published in a previous work (Ortega and González, 2007). Finally, the hazard maps were computed to show probabilistic ground accelerations with 10%, 5%, and 2% probabilities of exceedance in 50, 100 and 200 years. The maps were constructed on the assumption that earthquake occurrence is Poissonian. Then the hazard curve was computed for three specific dams belonging to the National Commission of Water in Mexico and different fault system combinations comparing the results. The details on the hazard estimation are described in Frankel (1995), and Frankel *et al*., (1997). In the following sections, the steps to prepare the different parts of the probabilistic hazard analysis are describe.

## Seismicity and moment rate

Two different models were used to compute the seismic hazard: Gutenberg-Richter and Characteristic Models. The former was used to analyze the transform fault system of the Gulf of California and the latter was used for the Quaternary faults within the Baja California Peninsula. For the Gutenberg-Richter model, the catalog was compiled for 18 years of operation of La Paz Seismic Network (Munguía *et al*., 2006). 2127 earthquakes ranging from 1 to 6.1 degrees in magnitude, between 23° < Lat < 25° and -111° < Long < -108° were located. The catalog to remove the aftershocks of 1998 in Los Barriles, and 2007 Cerralvo earthquake was reviewed (Ortega and Quintanar, 2010). In Figure 1d the seismicity of the region from 1998 to 2013 is present.

The $a$ and $b$ values were computed using the EMR method described by Woessner and Wiemer (2005), and coded in the Z-Map suite of programs (Wiemer, 2001, Figure 2). The $b$ values were estimated using a maximum likelihood method (Bender, 1983).

The hazard calculation using the Gutenberg - Richter model involves the summation of the source contribution ranging from a minimum to a maximum expected earthquake magnitude. For each magnitude, a fault rupture length is calculated using the relationships of Wells and Coppersmith (1994). Next, a floating fault along the geological fault was set, and then the distance to the floating rupture for each site to calculate the frequency of exceedance (equation 2 from Frankel (1995) was found).

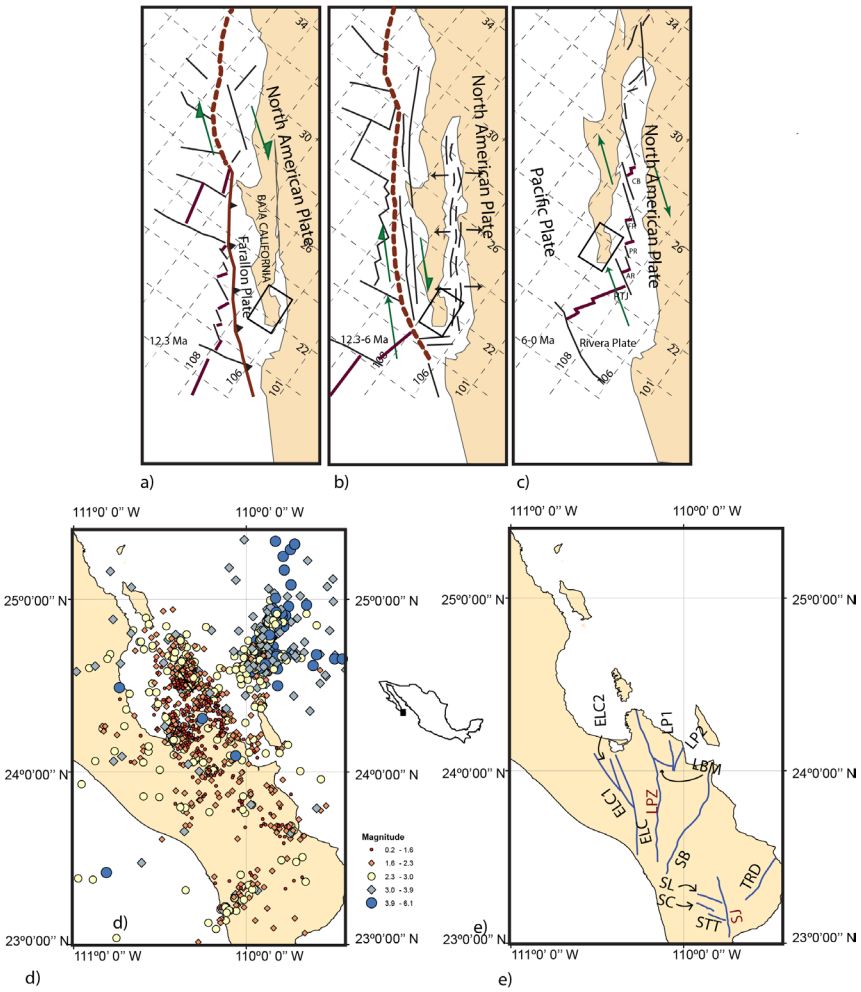


**Figure 1.** a) Farallon Plate that began the process of subduction starting the development of the Rivera Triple Junction. Between 20 and 12 Ma a series of microplates were formed along Baja California. b) Between 12 and 6 Ma normal faults with NNW and N trend, developed the east of the Tosco-Abreojos fault the system of normal faults was part of the distribution of the deformation, the gulf margin system was part of a complex system of transtensional faults. c) The regime of oblique divergence started about 6 Ma, when small rift basins began to form in the current Gulf of California. d) seismicity of the region, the complete catalog is represented. e) Quaternary Faults used in this article, La Paz and San José faults are used later to define different scenarios. AR, Alarcon Rise, PR, Pescadero Rise, FR Frallon Rise, CB Carmen Basin, RTJ, Rivera Triple Junction, and the faults: ELC, El Carrizal, ELC1, El Carrizal 1, ELC2, El Carrizal 2, LPZ, La Paz, LP1, San Juan de los Planes I, LP2, San Juan de los Planes II, LBM La Buena Mujer, SB, San Bartolo, TRD, La Trinidad, SL, San Lazaro, SC, San Carlos.

The estimation of the annual rate of earthquakes ($v_0$) for a characteristic fault was computed using the following relation (Wesnousky, 1986, Stirling and Gerstenberger, 2018):

$$v_0 = \mu \dot{u} LW / M_{0c} \qquad (1)$$

where $\mu$ is the shear modulus (30 GPa), $\dot{u}$ the annual slip rate of the fault, L and W are the fault length and width, respectively and $M_{0c}$ the characteristic moment obtained from the empirical scaling relation of Wells and Coppersmith (1994). The width of the fault $W$ was determined assuming a seismogenic depth of 20 km and projecting its dip, so that the width is equal to 20 km divided by the *sine* of the dip. The fault length is calculated from the total length of the digitized fault traces (Figure 1b). The slip rate was estimated using paleoseismic studies based on the overall vertical offset of the basins, and quantitative studies using trenches in specific areas (Maloney *et al*., 2007). Table 1 shows inland faults displacements and other parameters useful to estimate (1).

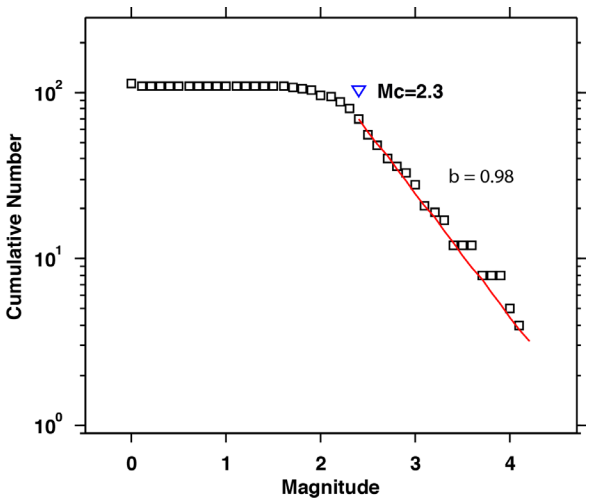


**Figure 2.** Plot of cumulative number of earthquakes versus earthquake magnitude, Mc =2.2 is the magnitude of completeness (b value is equal to 0.98).

The characteristic magnitude was determined from the length of the fault using the relationships of Wells and Coppersmith (1994), whose regression parameters depend on the tectonic environment. The characteristic moment was finally calculated from Kanamori (1977) equation once given the characteristic magnitude.

## Attenuation relations

The earthquake attenuation relations estimated in this area by Ortega and González (2007) were used. They observed that the attenuation in general is similar to that of southern California. The data were recorded using 32 strong-motion seismic stations from La Paz network

Table 1. Quaternary fault parameters used in this study.

| No. | Length (km) | Name | $M_{max}$ | Min. displacement (mm / year) | Max. displacement (mm / year) | Average displacement (mm / year) | Mo (dyne/cm) | Moment rate (dyne/cm*year) |
|---|---|---|---|---|---|---|---|---|
| 1 | 19.3 | San Juan de Los Planes I | 6.68 | 0.25 | 1 | 0.63 | 1.17E+26 | 7.24E+22 |
| 2 | 16.09 | San Juan de Los Planes II | 6.61 | 0.25 | 1 | 0.63 | 9.22E+25 | 6.03E+22 |
| 3 | 13.42 | La Buena Mujer | 6.54 | 0.25 | 1 | 0.63 | 7.27E+25 | 5.03E+22 |
| 4 | 39.47 | San José del Cabo | 6.95 | 0.5 | 1.5 | 1.00 | 2.97E+26 | 2.37E+23 |
| 5 | 15.22 | San Lázaro | 6.59 | 0.5 | 1.5 | 1.00 | 8.57E+25 | 9.13E+22 |
| 6 | 11 | Saltito | 6.47 | 0.7 | 0.8 | 0.75 | 5.61E+25 | 4.95E+22 |
| 7 | 11.35 | San Carlos | 6.48 | 0.25 | 1 | 0.63 | 5.84E+25 | 4.26E+22 |
| 8 | 71.4 | San Bartolo | 7.17 | 1 | 1 | 1.00 | 6.44E+26 | 4.28E+23 |
| 9 | 32.9 | Trinidad | 6.88 | 1 | 1 | 1.00 | 2.34E+26 | 1.97E+23 |
| 10 | 100 | La Paz | 7.30 | 0.11 | 1.6 | 0.86 | 1.00E+27 | 5.13E+23 |
| 11 | 65 | Carrizal | 7.14 | 0.11 | 1.6 | 0.86 | 5.70E+26 | 3.33E+23 |
| 12 | 34 | Carrizal1 | 6.89 | 0.11 | 1.6 | 0.86 | 2.45E+26 | 1.74E+23 |
| 13 | 37.5 | Carrizal2 | 6.93 | 0.11 | 1.6 | 0.86 | 2.78E+26 | 1.92E+23 |

(LAP) comprising 1320 small to moderate earthquakes (Figure 3). Some characteristics of the ground motion are:

a) attenuation functions for distances ranging between 40 and 100 km tend to slightly increase their amplitudes due to the critical reflections of the shear waves from the Moho. This feature is better observed at low frequencies (<5 Hz). These fluctuations are modeled in the parametric form of the geometrical spreading function, $g(r)$, which controls some changes in the seismic wave propagation.

b) values of the geometrical spreading control the general propagation effect due to distance between site and source. This propagation effect includes the source parameters, effects from finite faults that generate seismic waves at different depths, and the contribution of small and large earthquakes.

The predicted ground motion spectra at a frequency $f$ as a function of the hypocentral distance $r$ is given by:

$$logA_{ij}(r,f) = E_i(r_{obs},f)+SITE_j(f)+D(r,f) \quad (2)$$

where:

$$E_i(r_{obs},f)=log[S(f,M_w)+ +log[g(\frac{-\pi r_{obs}}{Q(f)\beta})exp(fr_{obs})] \overline{V}(f)e^{-\pi f\kappa eff} \quad (3)$$

and, $S(f, M_w)$ is the source Fourier velocity spectrum

$M_w$ is the moment magnitude

$g(r_{obs})$is the geometrical spreading function relative to $r_{obs}$ = 40 km

$Q(f)$ is the frequency-dependent quality factor

$\overline{V}(f)$ is a site amplification function

$\beta$ is the shear-wave propagation velocity

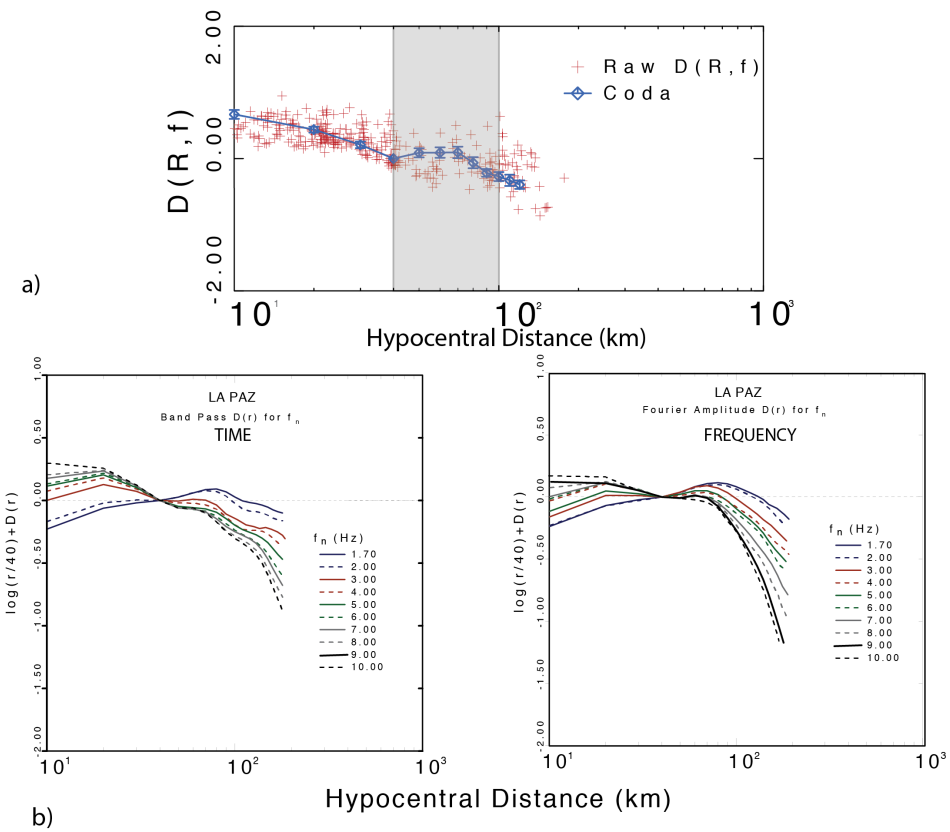


**Figure 3.** Attenuation relations estimated in the area. Top, example of the attenuation function from the regression, the gray area represents the distance between 40 and 100 km where the geometrical spreading exponent is low (0.2). Bottom, attenuation function for different frequencies using time (left) or frequency (right) analysis.

$\kappa_{eff}$ is a site attenuation coefficient

$r_{obs}$ is the observed distance from which we extrapolate to other distances

The second term is a level of motion that propagates the $S(f, M_w)$ term at $r_{obs}$. The source function $S(f)$ is a simple $\omega^2$ model as described by Brune (1970):

$$\mathrm{S}(f, Mo) = \frac{CM_0 2\pi f}{1+(f/[4.91\mathrm{x}10^6\,\beta\,(\Delta\sigma/M_0)^{1/3}])^2} \quad (4)$$

where: $C$ is equal to (0.55) (2) (0.707)/$4\pi\rho\beta^3$
the term $[4.91\mathrm{x}10^6\,\beta\,(\Delta\sigma/M_0)^{1/3}]$ is the corner frequency
$\Delta\sigma$ is the stress parameter in (bars)
$\beta$ is the average shear-wave crustalvelocity (3.5 km/sec.)
$M_0$ is the scalar seismic moment, which in turn is related to the moment magnitude (Kanamori, 1977).

$$M_w = \left(^{logMo}/_{1.5}\right) - 10.73. \quad (5)$$

Magnitude-distance tables were constructed using the SMSIM suite (Boore, 1983) and the ground motion parameters of Table 2.

Table 2. Ground-motion parameters

| | |
|---|---|
| $\kappa_{eff}$ | 0.06 |
| $\mathrm{Q}(f)$ | $180f^{0.32}$ |
| $\beta$ | 3.5 |
| $\rho$ | 2.8 |
| $\overline{\nabla}(f)$ | GEN97* |
| $\Delta\sigma$ | 40 |
| $\mathrm{g}(r)$ | $\begin{cases} r^{-1.0} & 0 \le r < 40 \\ r^{-0.2} & 40 \le r < 100 \\ r^{-0.5} & 100 \le r < 180 \end{cases}$ |

These attenuation relations are used in a look-up table procedure that was originally coded by (Frankel, 1995) in the USGS computer programs.

**Hazard estimation**

The hazard calculation was performed using the codes of USGS for the National Seismic Hazard Mapping Project (NSHMP) (Petersen, 2008). This code has the flexibility to be easily adapted and has been extensively reviewed during some decades (Frankel, 1995; Frankel *et al*., 1997). The attenuation relation's analysis were adapted using a look-up table. This code has the advantage that the data structure is virtually identical to the New Generation of Attenuation relations (NGA) that has been reviewed recently. So, any logical tree that would be adequate to this region can be created, including NGA attenuation relations. For simplicity, the attenuation relations of Table 2 were used. On the other hand, there are some advantages of using this computer code such as simple input of geological data and easy access to adjust the source code. This code has different modules including a smoothed grid source (Frankel, 1995) and floating fault sources. The program allows choosing between Gutenberg – Richter or the Characteristic models. During the last 20 years, thas been observed that there is not enough information to compute robust $a$ and $b$ values for Quaternary faults. However, for transform fault systems, the Gutenberg – Richter model is adequate. Most of the seismicity occurred in main - aftershock earthquake sequences, and once the aftershock removal is performed, the seismicity parameters can be obtained. The hazard calculation was performed using the Characteristic model for the Quaternary faults and the Gutenberg – Richter for the transform fault system.

**Fault contributions**

There are two types of sources. Active faults and Quaternary Faults both sources are fault areas; there is much work in defining the correct source. For the Quaternary faults, which is the focus of this article, in a map view, a fault is a line because it is expressed as a strike and dip. Not a smoothed grid area source was used because the transform system is well defined and there is no sparse seismicity in the surrounding region. The active faults were modeled using the Anderson (1979) model. The seismogenic thickness is constrained to 20 km; the fault dip is based on geophysical models (Arzate, 1986). Since the present model is based on the Characteristic fault rupture, then completeness magnitude and statistical values of a and b are not used. However, in the active tectonics, the maximum magnitude and magnitude range play an essential role.

In the study area, faults that control the hazard are not well identified and different authors disagree on whether some faults should be considered as potentially dangerous in hazard estimation. The purpose of this work is to test whether there are significant

differences if some Quaternary fault segments are included or discarded in the seismic hazard analysis. First, the seismic hazard was computed using all the source information that is available from the national geological maps of the Mexican Geological Survey (SGM), using the 1: 10,000 and 1: 250,000 maps (SGM, 1996, 1999, 2000, 2001, 2002, 2008). Second, two different scenarios were computed: scenario (a), the seismic hazard without La Paz fault (WLP), and scenario (b) seismic hazard without San Jose fault (WSJ). Finally, the PGA for 3 sites was computed. In Figure 4, the results of the probabilistic seismic hazard analysis for all the faults are shown. It is noticeable that the Transform Fault System of the Gulf of California controls the seismic hazard for short return periods. This are to the use of the Characteristic Model for inland faults with a return period greater than 1000 years, and these characteristic faults do not contribute to the hazard estimation for short return periods. On the other hand, in the case of long return periods the characteristic faults control the hazard.

In Figure 4, the lower panels represent the 2% of exceedance of 50, 100 and 200 years that correspond to return periods of 2479, 4950 and 9900 years, respectively. These return periods are usually used for the engineering design of essential facilities such as bridges and dams.

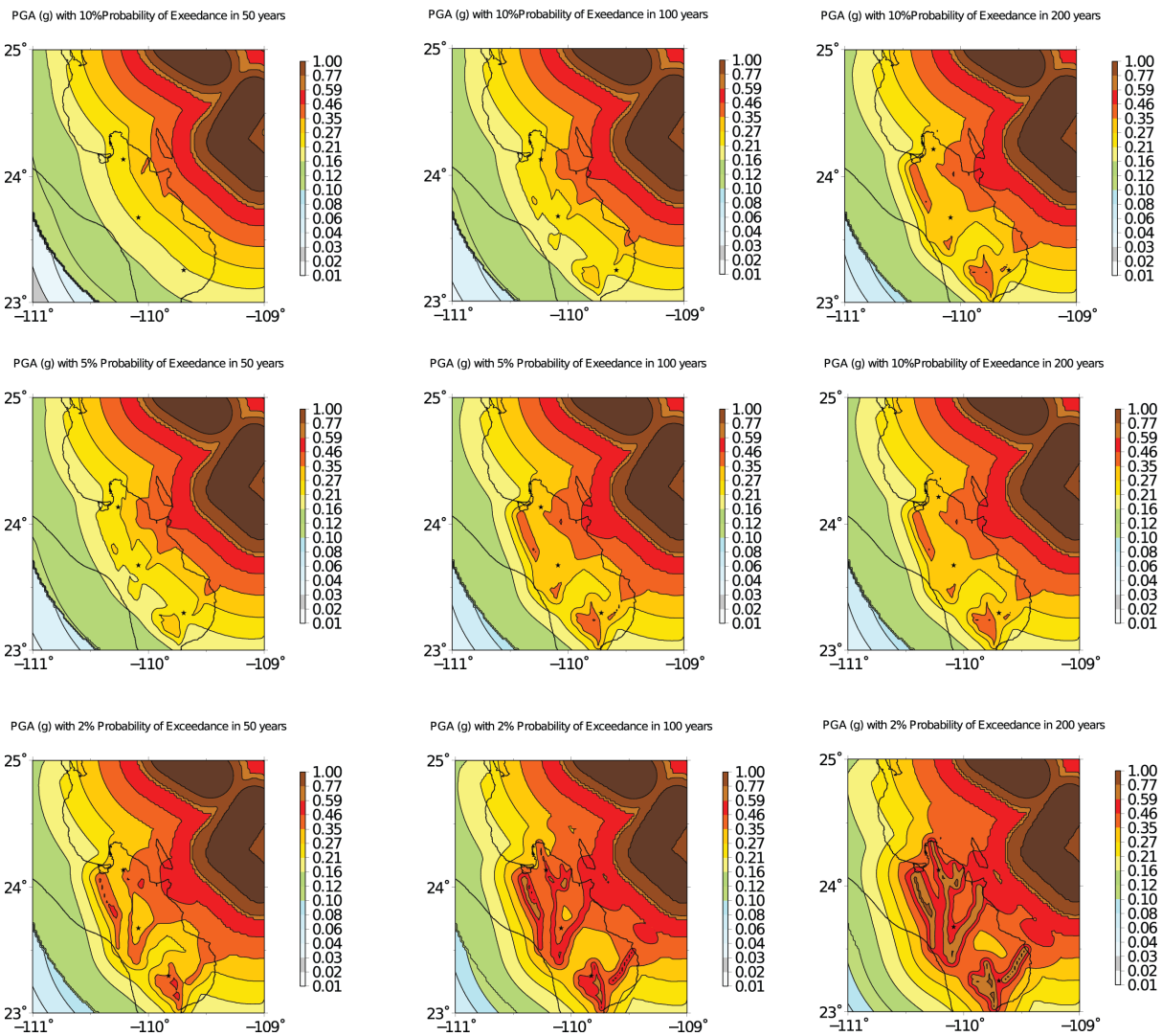


**Figure 4.** Probabilistic seismic hazard analysis for different return periods and observation times using all the sources. The transform fault system is located at the top right of the map and analyzed with the Gutenberg-Richter model. The Quaternary faults are located within the Baja California Peninsula and analyzed with the Characteristic model, the stars represent the site of the dams, the northern dam is La Buena Mujer, in the middle Santa Ines and at the southern side La Palma (see text for details).

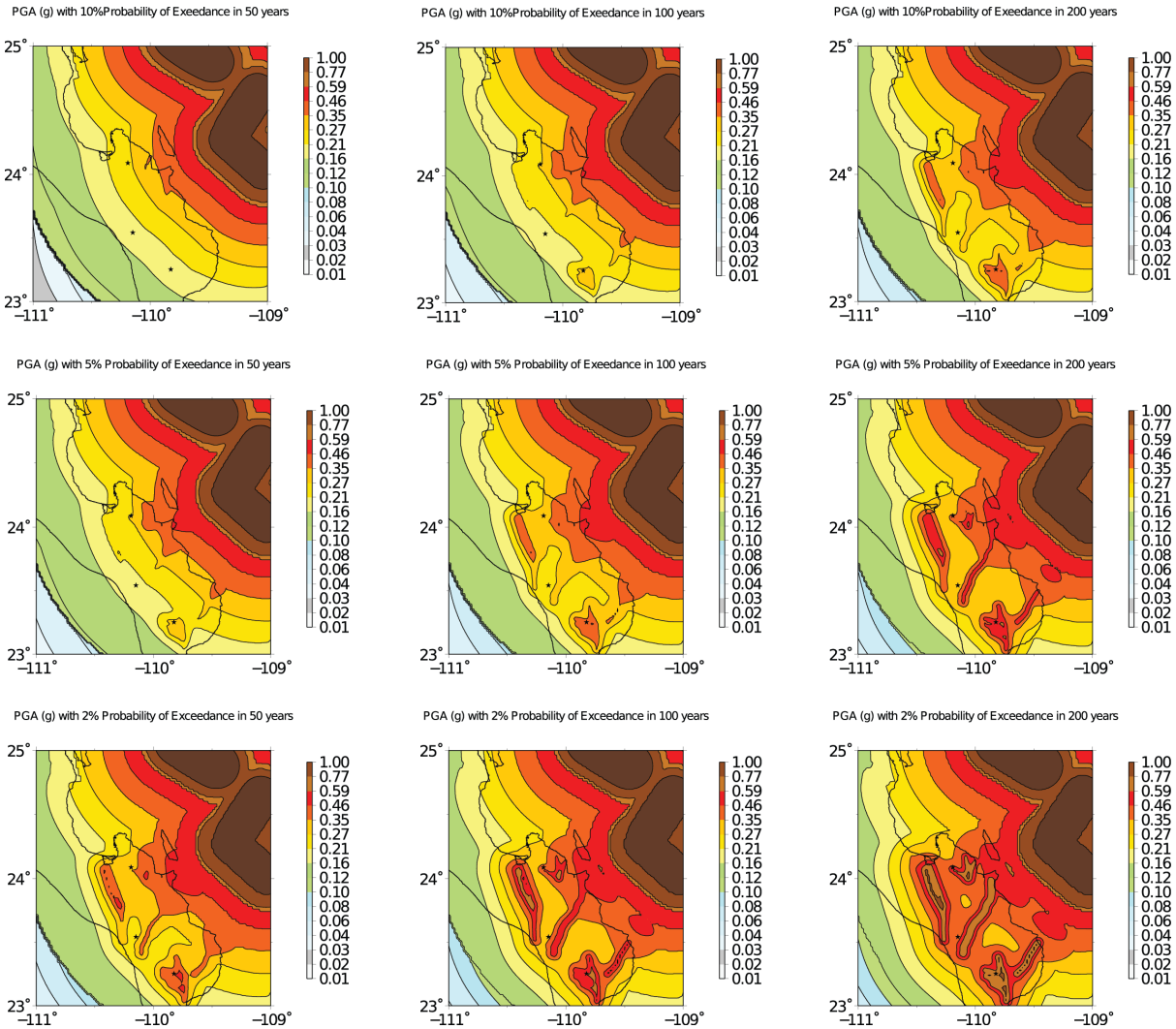


**Figure 5.** Probabilistic seismic hazard analysis for different exceedance probabilities and observation periods using the WLP model. The transform fault system is located at the top right of the map and analyzed with the Gutenberg-Richter model. The Quaternary faults are located within the Baja California Peninsula and analyzed with the Characteristic model (see text for details).

In the last panel of Figure 4, the location of the three principal dams (stars) match with the region of the high seismic hazard.

In Figure 5 the seismic hazard using the WLP model is shown and for short return periods (panels 1,2,4) the maps are virtually identical. However, for long return periods there are substantial differences among the principal dams, especially for the Buena Mujer and Santa Ines dams, identified at the northern side of the region (panels 6,7,8 and 9). In contrast, La Palma dam is too far from La Paz fault and the hazard contribution is negligible.

Similarly, in Figure 6, the hazard using the WSJ model was calculated. The San José fault affects La Palma dam and is not contributing to the hazard of Buena Mujer and Santa Ines dams. In this case, the presence of smaller faults (Saltito, San Lazaro, Trinidad) are of special importance since they are located close to La Palma dam and the absence of the San José fault in the hazard calculation is not so sensitive as is the case of the WLP model.

Figure 7 shows a comparison among models for PGA values of hazard calculation for different return periods and the three different fault scenarios. In the absence of these faults, the PGA is reduced for the long return period.

In Figure 8, the hazard curve of the complete model for La Palma, Santa Ines and

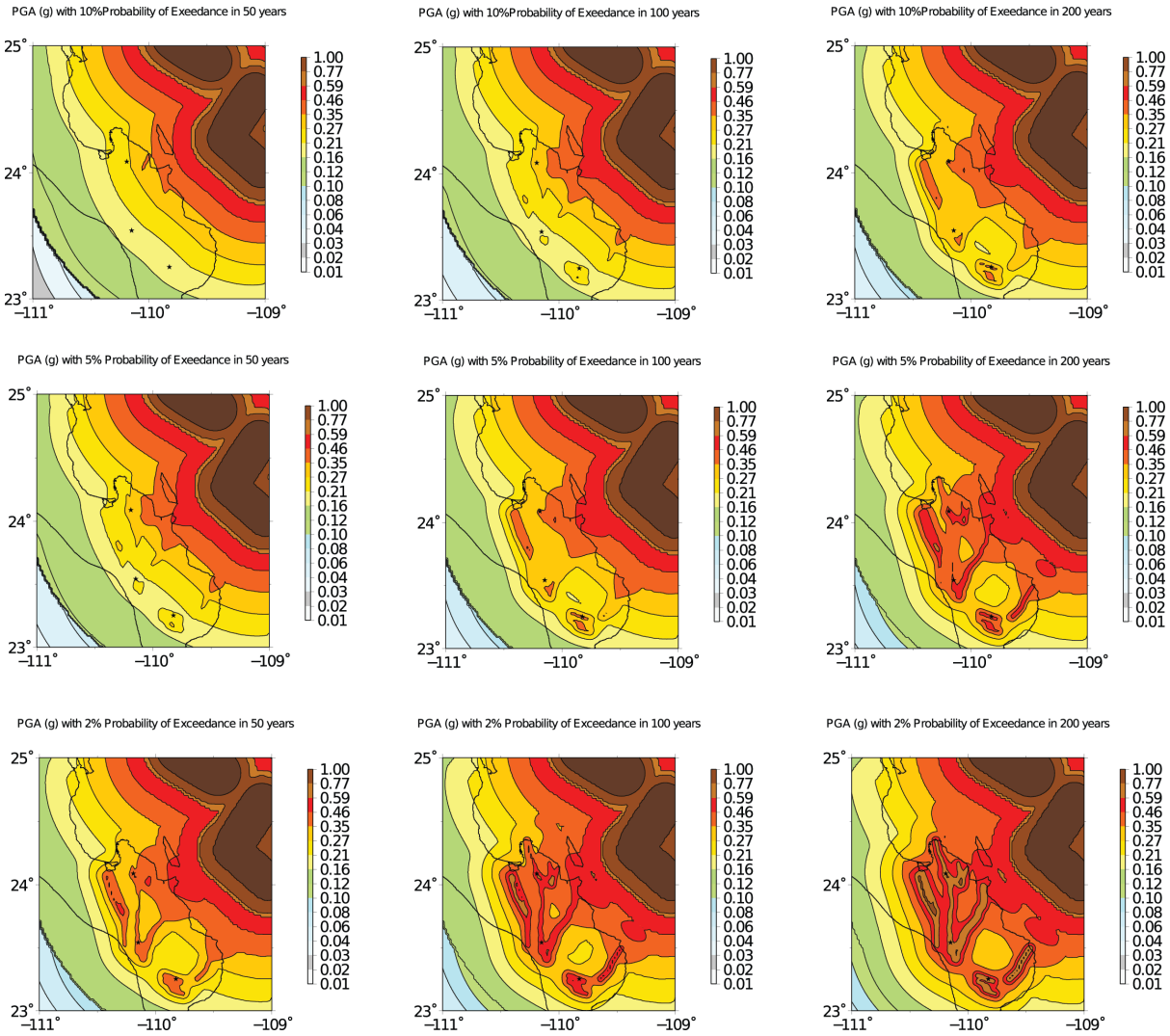


**Figure 6.** Probabilistic seismic hazard analysis for different return periods and observation times using the WSJ model. The transform fault system is located at the top right of the map and it was analyzed with the Gutenberg-Richter model. The Quaternary faults are located within the Baja California Peninsula and analyzed with the Characteristic model (see text for details).

Buena Mujer dams is depicted. In the hazard curve, the Characteristic Fault Model was used excluding the transform faults of the Gulf of California. The three curves are similar; the Buena Mujer and Santa Ines curves are parallel because their hazard is controlled mainly by La Paz fault, and the rest of the faults are not important.

In Figure 9, the hazard curves of the three dams using the WLP model are shown. In this case, the three curves are different and we observe that the Santa Ines dam has lower PGA values. The Santa Ines dam is relatively far from the other faults, except for La Paz fault that is the closest to the dam.

In Figure 10, the WSJ model is depicted. Interestingly, the WSJ and the complete model of Figure 8 are similar, suggesting that for these sites the contribution of the San José fault is not so important.

In general, the hazard estimation has been used in Mexico with $a$ and $b$ values statistical coefficients of seismicity. Little importance has been given to faults that exhibit large return periods and pose risks in the long term. A recent example reported by a study of seismic hazard in central Mexico used instrumental seismicity as well as historical data includeding fault information (Beyona *et al*., 2017). However, this is the first time that a similar study is performed in Baja California

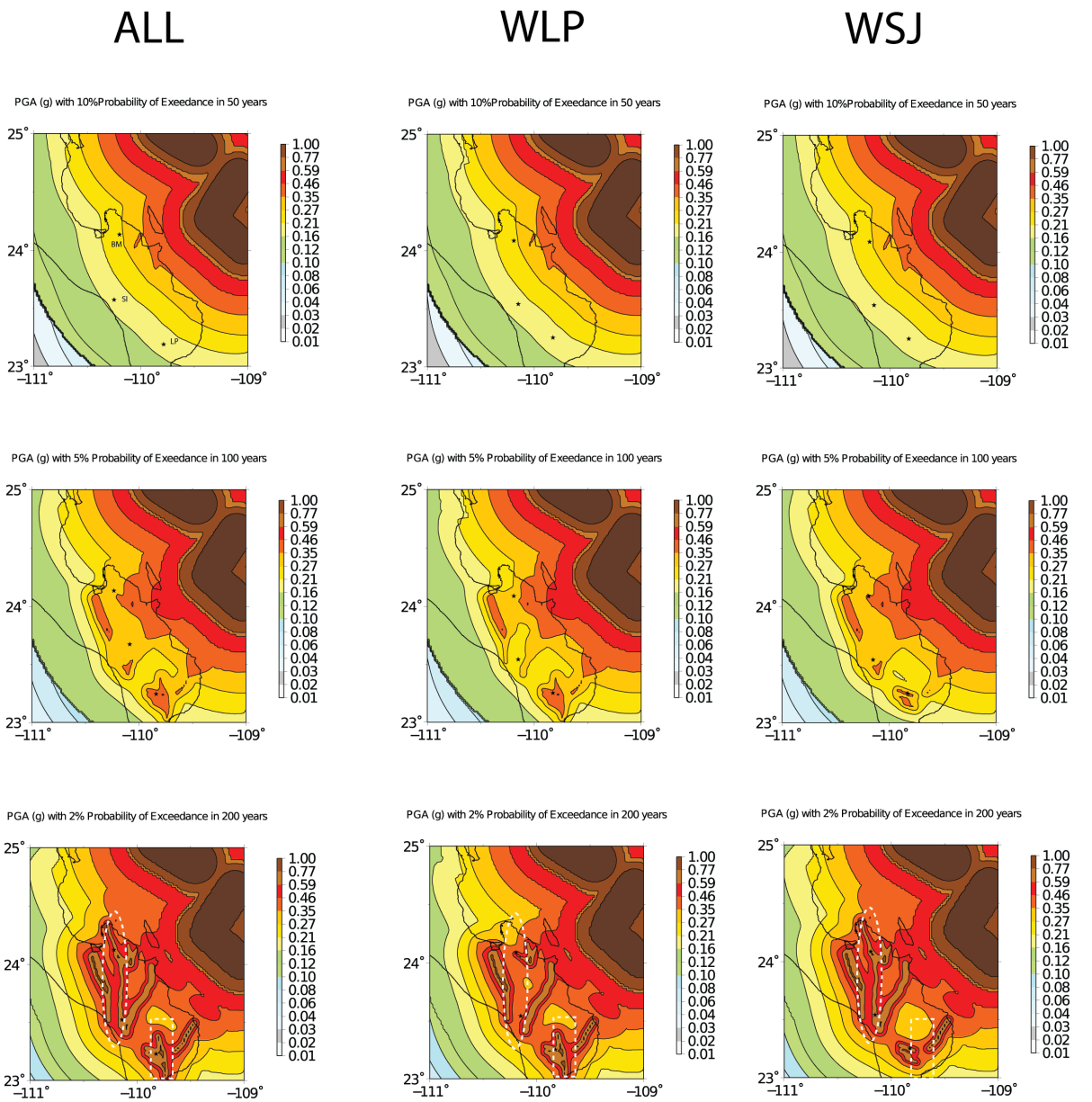


**Figure 7.** Contour plot for PGA values of hazard calculation for different return periods and three different fault scenarios. Left column, model with all faults; central column, model without La Paz fault; right column, model without San José fault. The cases are 10% of probability of exceedance in 50 years (first row, from top to bottom); 5% of probability of exceedance in 100 years (second row); 2% of probability of exceedance in 200 years (third row). The last row shows the long return period expressed as 2% probability of exceedance in 200 years. The elliptical region covers La Paz fault and the squared region San Jose fault. BM Buena Mujer Dam, SI Santa Ines Dam and LP La Palma Dam.

Sur. There are some reasons why long return periods have not been traditionally considered in the seismic hazard estimation in Mexico, such as: a) the high active tectonics in the coast which is usually more important than inland active faults and b) there are insufficient paleoseismic studies in the region. However, in Baja California Sur, the active sources with high annual moment rate occur in the Gulf of California, and Quaternary faults are located in the peninsula. Moreover, this region was originally populated in areas close to principal faults, because these faults are the principal sources of water that is collected from the mountain ranges situated at the center of the Peninsula. Also, these faults are the cause of the high mineralization of gold, copper and silver, giving rise to important mining development. Therefore, there is a high correlation between fault location and population.

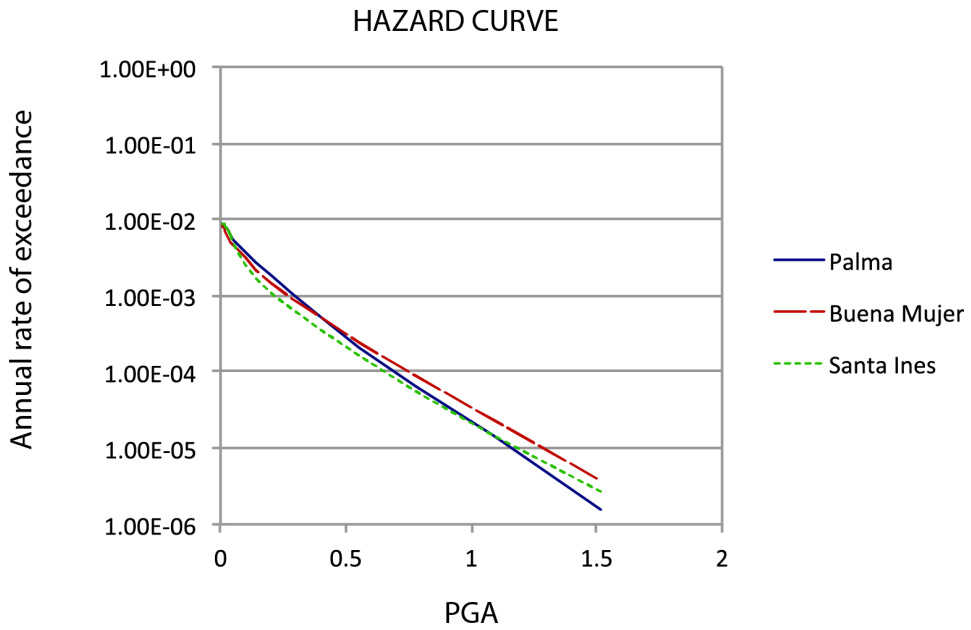


**Figure 8.** Hazard curve for the complete model for La Palma, Santa Ines and Buena Mujer dams using the Characteristic models of the Quaternary faults.

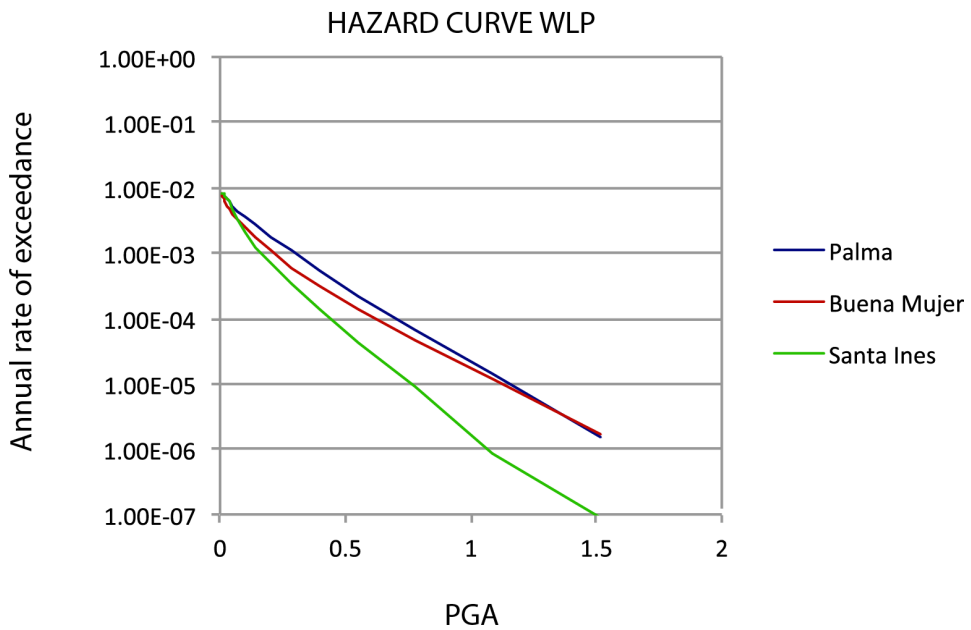


**Figure 9.** Hazard curve of the WLP for La Palma, Santa Ines and Buena Mujer dams using the Characteristic models of the Quaternary faults.

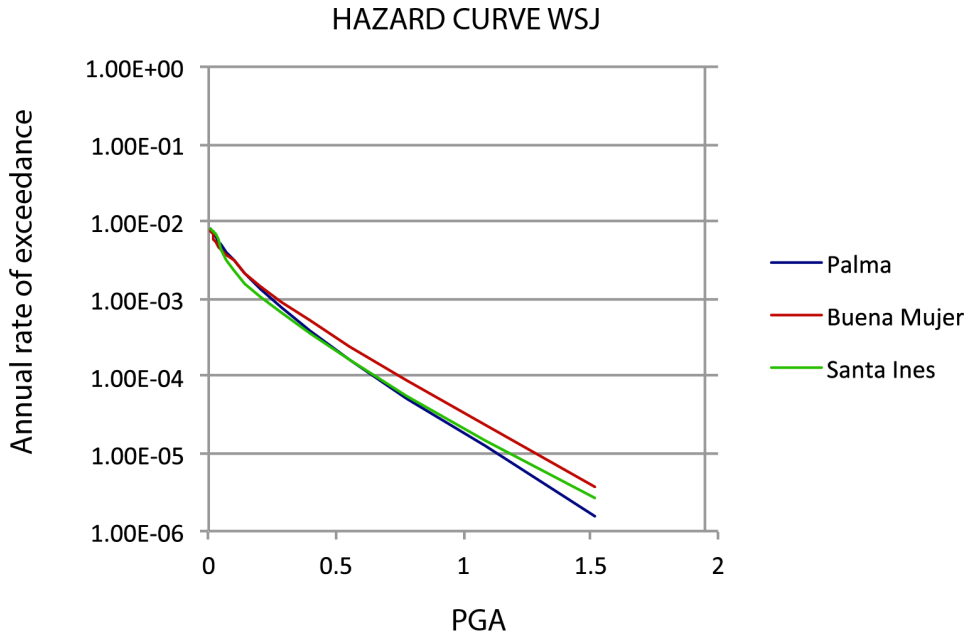


**Figure 10.** Hazard curve of the WSJ for La Palma, Santa Ines and Buena Mujer dams using the Characteristic models of the Quaternary faults.

Another contribution of this study is the usage of attenuation relations obtained for this region. A simple look-up table of magnitude-distance based was introduced on the work of Ortega and González, (2007). However, the results do not differ considerably when the attenuation relations of Southern California are used instead, since they are characterized by similar values of $Q(f)$, geometrical spreading function and kappa (Ortega and Gonzalez, 2007). Moreover, the NGA attenuation relations are also a good approximation. In this work, rather than analyzing the sensitivity of the predictive relationships, the differences in considering or ignoring some faults are studied.

## Discussions

Including or excluding faults in PSHA implies great differences in the results. This is not surprising in PSHA because this problem has been observed over decades in different regions, however, there are some interesting aspects of this region that we will discuss. First, the PSHA is based on a formal probabilistic framework that considers all the uncertainties, including the epistemic ones. For this reason, PSHA is based on logic trees that mimics the probability distribution of the seismic sources epistemic errors. To design the logic tree, decisions are always made through panels of experts. Marzochi and Jordan (2017) discussed a global framework to analyze the PSHA, in their article they noted the importance of the participation of experts, but it is important to say that there is a subjective part that implies adding preferential information, which not always seem to have a scientific basis. It is important to emphasize that adding subjective preferences is not necessarily non-scientific knowledge, the most important thing is to be able to prove if our preferences make sense or if they should be discarded in the future.

A problem that frequently occurs in the PSHA by participating in a committee of experts that is specifically focused to seismic hazard, is that experts tend to strategically manipulate their opinion. For example, in the case of giving advice on the existence of a fault to develop hazard maps, an expert knows that in case of an error there is a risk of a major disaster, but in the case of developing maps of natural resources those errors are not so relevant and probably their opinion will be different. In addition, an expert may be pro- environment and inadvertently he would include more restrictions if the panel of experts take decissions for nuclear power plants for example. After analyzing the best option for PSHA the logic tree of Figure 11 was prefered. This model exemplifies the epistemic uncertainty of sources, magnitude and attenuation relations (GMPE, Ground motion prediction equations).

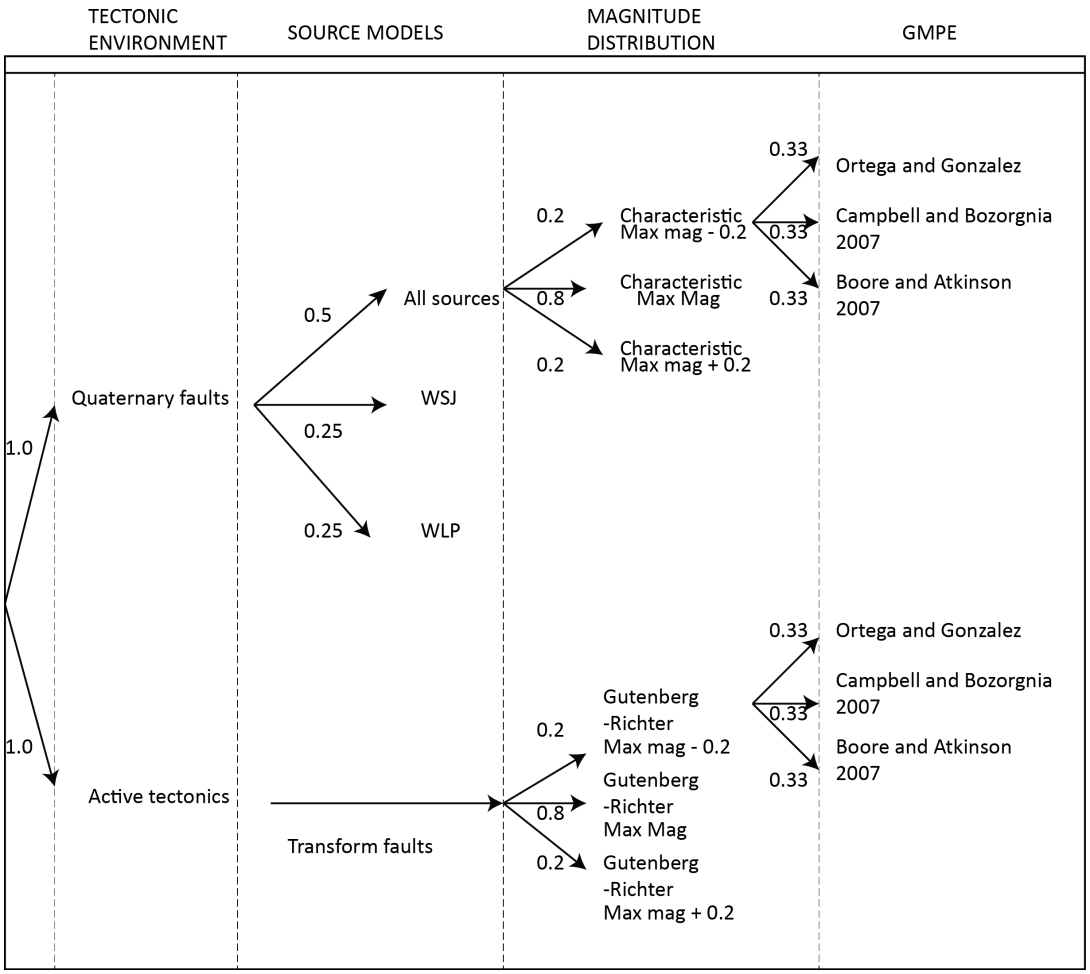


**Figure 11.** Logic tree for PSHA of Baja California Sur.

The logic tree of Figure 11 is based on analyzing advantages and disadvantages of the different models. In this model, the most important decision was the Quaternary faults weights of three different models (all faults, WSJ and WLP).

In Figure 12 the final map for two return periods is presented, the first panel represents 2% of exceedance in 50 years, the second represents 2% of exceedance in 200 years, therefore the first is equivalent to a return period of 2475 years and de second of 9900 years. In this interval, there is a major difference in the hazard maps. However, the 2475 return period is sometimes considered as the highest threshold for essential facilities. Comparing the 2475 return period (Figure 12 first panel) with the 474 years (Figure 4 first panel) we observe that the Quaternary faults apparently are not sensitive for high rates. However, this is only a mere artifact of the arbitrary decision of using return periods as a degree of protection because at higher return periods the hazard should be nuanced. Recently Stirling and Gerstengerg (2018), studied the applicability of a Gutenberg-Richter magnitude distribution instead of the Characteristic fault model. In their study Stirling and Gerstengerg (2018) analyzed active faults with high slip rates (> 1 mm/yr), their results suggest that the Gutenberg Richter magnitude distribution is compatible with active faults and cannot be ruled out in PSHA, but for low slip rates ( < 1 mm/yr), this possibility has not been tested yet. Our study opens a possibility to improve the PSHA in Baja California to include the Gutenberg-Richter magnitude distribution in the future. Similar studies have been reported in central Mexico (Bayona *et al*., 2017). Work is in progress to present a combination of Gutenberg-Richter and Characteristic magnitude distribution. Care should be taken if we compare our results with other studies, for example, it is common to represent a PGA concerning a specific rock

site namely Vs30=760, this reference is based on geotechnical studies in which there is a competent rock at 30m depth with a value of 760 m/s for shear wave velocity. We used a general average value that represents the common amplification of the basins in BCS. Also, we used a low attenuation model. It is important to note that we do not have the intention to use our results for engineering purposes until we can validate them.

This article reflects the importance of studying active Quaternary faults at a regional scale. Paleoseismic studies provide valuable information about slip rates. It is crucial to use this information in the seismic hazard analysis and include the results in a specific way that can be useful in hazard maps. For example, Busch *et al*. studied the Carrizal Fault (Figure 1) they prepared trenches and presented their results in a self-consistent tectonic framework. Their studies discussed a tectonic relation of the transtensional regime in Baja California. We obtained the slip rate from their analysis, but in other cases, the slip rate is not estimated. For example in the La Paz fault. In that case, we only estimated a possible slip rate based on limited work about the fault.

Nowadays, paleoseismology studies are becoming a new discipline; they also provide information that the instrumental seismicity is not capable of obtaining. The active crustal faults sometimes are not included in PSHA because it seems that they are not as dangerous if compared to active tectonics (e.g., subduction margins), but we believe that this impression is incorrect. The Major-Cucapah earthquake in 2010 (Mw = 7.2) that occurred in Mexicali, Baja California is an excellent example of a crustal fault that caused severe damages. The geological and geophysical geometry is essential to consider in mapping the damages (Wei *et al*., 2011), the recurrence is about 2,000 years (Rockwell *et al*., 2010) so, if we compare to the active tectonics of few tens of years, it probably should be not so critical. However, the problem is the location of these faults. In the Baja Peninsula, the faults are located close to the urban centers.

Another problem to address is the lack of studies and instrumentation. For example, Suter (2018) reported the Loreto earthquake of 1878; this event seems to be the worst scenario for Baja California Sur, the destruction was very severe. Up to date, there are no studies that identify the actual fault. Note that in this region, there are seismic records with extreme levels of PGA, in 2007 a strong motion instrument recorded an earthquake with a maximum value of 0.6 g in Bahia Asuncion (Munguia *et al*., 2010; Ortega *et al*., 2017). The value of 0.6 g exceeds by far any expected value in previous hazard maps in the region, reflecting the need to study the Quaternary Faults and the effect in the seismic hazard.

We conclude that the Quaternary faults are only important when computing the hazard using high recurrence rates. In places where the active tectonic sources, such as faults belonging to the transform fault system, are far from the sites, as is the case of Baja California Sur, the contribution of the hazard of such Quaternary faults is not so evident. Specially for low recurrence rates. Clearly, a detailed paleoseismic study is of crucial importance to assess the hazard for this region. The complete model with all the sources is the best for earthquake-resistance structures, especially for dams' design. On the other hand, overestimating the hazard may have the consequence of introducing unnecessary severe construction codes causing an economic impact on the development of this region due to the increase in construction costs. In Mexico, there is no specific guidance for choosing return periods on dams' designs. However, the general trend of 2% of exceedance in 50 years may be not adequate and 2% of exceedance in 200 years seems to be adequate in Baja California Sur. This level of security has a large impact in the economic development and is very important for strategic planning.

## Conclusions

The general conclusions are:

1) The southern part of Baja California is a region with important faults that control the seismic hazard of the high return periods.

2) Active Quaternary faults need to be studied, especially the average displacement or moment rates.

3) Specifically, in Baja California Sur, the return period for critical facilities should be 9900 years expressed as the 2% probability of exceedance in 200 years.

## Acknowledgments

This work is the effort of many years of seismic studies; we are in debt with the technical staff of CICESE Ensenada who initiated most of the field work in Baja California Sur. Alfredo Aguirre and Sergio Mayer are acknowledged for maintaining the seismic stations of Baja California Sur during the past 18 years. We

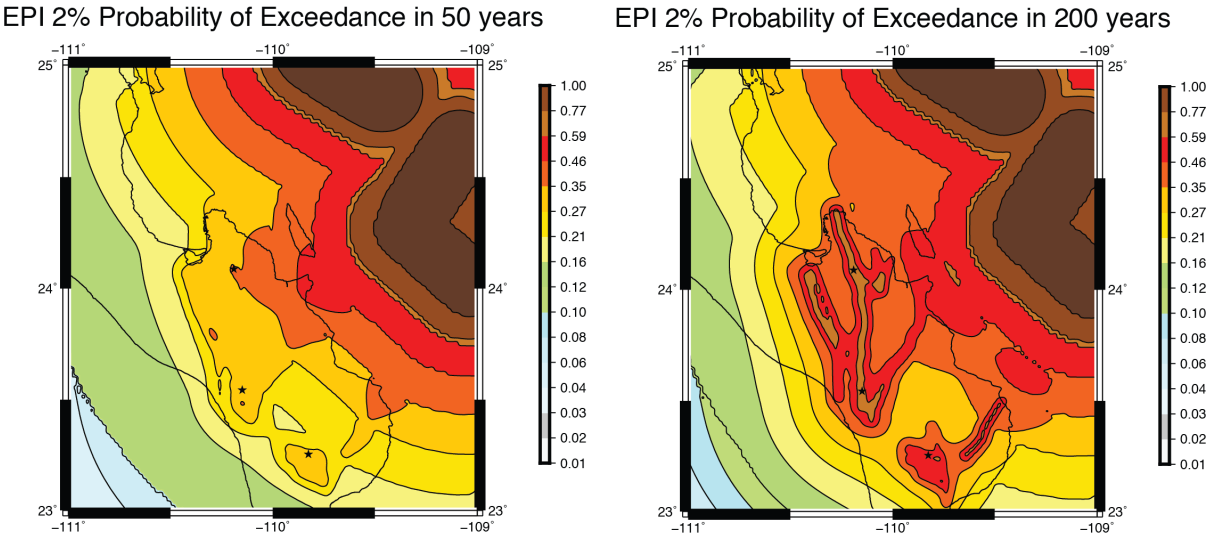


**Figure 12.** Hazard map of the final model using a logic tree for Baja California Sur for two different return periods. The 2% probability of exceedance in 50 years is a standard for dam designs. In contrast a 2% probability of exceedance in 200 years is plotted for comparison.

acknowledge three anonymous reviewers that helped to improve the quality of this article. This work was partly supported by a CONACYT grant number 133910, CICESE internal projects 691114, 691115, and Cátedras Conacyt projects 97 and 2284.

## References

Algermissen, S.T., and D.M. Perkins ,1976, A probabilistic estimate of máximum acceleration in rock in the contiguous United States, *US Geological Survey Open – File Report* 76 – 416, 45 pp., 3 plates.

Algermissen, S.T., Perkins, D.M., Thenhaus, P.C., Hanson, S.L., and Bender, B.L., 1990, Probabilistic earthquake acceleration and velocity maps for the United States and Puerto Rico, *US Geological Survey Map MF – 2120*, 2 sheets, 4 plates.

Anderson, J.G.,1979, Estimating the seismicity from geological structures for seismic risk studies, *Bull. Seism. Soc. Am*. 69 135 -158.

Angelier, J., B. Colletta, J. Chorowicz, L. Ortlieb, and C. Rangin, 1981, Fault tectonics of the Baja California peninsula and the opening of the Sea of Cortez, Mexico, *Journal of Structural Geology* 3, no. 4, 347–357, doi:10.1016/0191-8141(81)90035-3.

Arzate, J. 1986. Geophysical Reconnaissance for Geohydrological Evaluation in the La Paz-El Carrizal Valley, Baja California Sur, Mexico. M.S. Thesis. International Institute for Aerosurvey and Earth Sciences (ITC), Delft, Holanda.

Atwater, T.,1970, Implications of plate tectonics for the Cenozoic tectonic evolution of western North America, *Geol. Soc. Am. Bull*. 81 3513– 3536, doi:10.1130/0016-7606(1970)81[3513: IOPTFT]2.0 .CO;2.

Bayona Viveros J. A., G. Suarez G. and M. Ordaz, 2017, A probabilistic seismic hazard assesment of the Trans-Mexican volcanic belt, Mexico, based on historical and instrumentally recorded seismicity, Geofisica Internacional, 56, 1, 87-101.

Bender, B., 1983, Maximum likelihood estimation of b values for magnitude grouped data, *Bull. Seism. Soc. Am*. 73, no. 3, 831 -851.

Bernreuter, D.L., J.B. Savy, R.W. Mensing, and J.C. Chen, 1989, Seismic hazard characterization of 69 nuclear power plant sites east of the Rocky Mountains, *U.S Nuclear Regulation Commission, NUREG/CR – 5250, UCID 21517,* Lawrence Livermore National Lab.

Boore, D. M., 1983, Stochastic simulation of high-frequency ground motions based on seismological models of the radiated spectra, *Bull. Seism. Soc. Am.* 73, no.6 1865-1894.

Brune, J. N., 1970, Tectonic stress and the spectra of seismic shear waves from earthquakes*, J. Geophys. Res*. 75, 4997–5009, doi:10.1029/JB075i026p04997.

Busby, C. J. and R.V. Ingersoll, 1995, *Tectonics of sedimentary basins*, Blackwell Science, Cambridge, MA, 579 pp.

Busch, M.M., J.R. Arrowsmith, P.J. Umhoefer, G. Martínez- Gutiérrez, N.A. Toké, D. Brothers, E.N. DiMaggio, S.J. Maloney, O. Zielke, and B. Buchanan (2006). Late Quaternary faulting in the Cabo San Lucas–La Paz region, Baja California, *Eos (Transactions, American Geophysical Union).* 87, no. 52, fall meeting supplement, [abs] T41D-1612.

Busch, M.M., J.A. Coyan, J.R. Arrowsmith, S.J. Maloney, G. Martínez-Gutiérrez, and P.J. Umhoefer, 2007, Late Quaternary faulting along the San Juan de Los Planes fault zone, Baja California Sur, Mexico, *Eos (Transactions, American Geophysical Union).* 88, no. 52, [abs] T41A-0357.

Cornell, C.A., 1968, Engineering seismic risk analysis, *Bull. Seism. Soc. Am*. 58, 1583 – 1606.

Cruz Falcón A., R. Vázquez González, J. Ramírez Hernández, F. Salinas González, E. Nava Sánchez and E. Troyo Diéguez, 2010, Depth estimation to cristalline basement in the valley of La Paz, Baja California Sur, Mexico*, Geofísica Internacional*, 49, 213-224.

DeMets, C., 1995, A reappraisal of seafloor spreading lineations in the Gulf of California: Implications for the transfer of Baja California to the Pacific plate and estimates of Pacific–North America motion, *Geophys. Res. Lett.* 22, no. 24, 3545–3548, doi:10.1029/95GL03323.

Electric Power Research Institute, 1986, Seismic hazard methodology for the Central and Eastern United States, *Technical Report*, vol. 1 -3.

Fletcher, J. and L. Munguía, 2000, Active continental rifting in southern Baja California, Mexico: Implications for plate motion partitioning and the transition to seafloor spreading in the Gulf of California, *Tectonics*, 19, 1107-1123.

Fletcher, J.M., M. Grove, D. Kimbrough, O. Lovera, and G.E. Gehrels, 2007, Ridge-trench interactions and the Neogene tectonic evolution of the Magdalena shelf and southern Gulf of California: Insights from detrital zircon U-Pb ages from the Magdalena fan and adjacent areas, *Geol. Soc. of Am. Bull.*, 119, 1313–1336, doi:10.1130/ B26067.1.

Frankel, A., 1995, Mapping seismic hazard in the central and Eastern United States, *Seism. Res. Lett*., 66, no. 4, 8 -21.

Frankel, A., C. Muller, T. Barnhard, D. Perkins, E. Leyendecker, N. Dickman, S. Hanson, and M. Hooper, M, 1997, Seismic hazard maps for the conterminous United States, *U.S. Geological Survey Open File Report* 97 – 131, 12 maps.

Gorbatov, A. and Y. Fukao, 2005,. Tomographic search for missing link between the ancient Farallon subduction and the present Cocos subduction, *Geophy. J. Int.* 160, Issue 3, 849–854, https://doi.org/10.1111/j.1365-246X.2005.02507.x.

Hausback, B.P., 1984, Cenozoic Volcanic and Tectonic Evolution of Baja California Sur, Mexico, *Ph.D. thesis*, Berkeley, University of California, 72 pp.

Kanamori, H., 1977, The energy release in great earthquakes, J. Geophys. Res. 82, (20), 2981–2987, doi:10.1029/JB082i020p02981.

Lizarralde, D., G.J. Axen, H.E. Brown, J.M. Fletcher, A. González-Fernández, A.J. Harding, W.S. Holbrook, G.M. Kent, P. Paramo, F. Sutherland, and P.J. Umhoefer , 2007, Variation in styles of rifting in the Gulf of California, *Nature*, 448, 466–469, doi:10.1038/ nature06035.

Maloney, S.J., P.J. Umhoefer, J.R. Arrowsmith, G. Martinez- Gutiérrez, A.U. Santillanez, and Rittenour, 2007, Late Pleistocene–Holocene faulting history along the northern El Carrizal fault, Baja California Sur, Mexico, Earthquake recurrence at a persistently active rifted margin Eos *(Transactions, American Geophysical Union)*, 88, no. 52, abs, T41A-0357.

Marzocchi, W., and Jordan, T. H. ,2017, A Unified Probabilistic Framework for Seismic Hazard Analysis. *Bull. Seism. Soc. Am*, 107, 2738-2744. doi: 10.1785/0120170008.

Mayer, L., and K.R. Vincent, 1999, Active tectonics of the Loreto area, Baja California Sur, Mexico, *Geomorphology*, 27, 243–255, doi:10.1016/S0169 -555X (98)00074-9.

Munguía, L.M., M. González, S. Mayer, and A. Aguirre, 2006, Seismicity and state of stress in the La Paz– Los Cabos region, Baja California Sur, Mexico, *Bull. Seism. Soc. Am.* 96, 624–636, doi:10.1785/0120050114.

Ortega, R. and M. Gonzalez, 2007, Seismic-wave attenuation and source excitation in La Paz-Los Cabos, Baja California Sur, Mexico, *Bull. Seism. Soc. Am*. 97, 545-556 doi:10.1785/0120060083.

Ortega, R. and L. Quintanar, 2010, Seismic evidence of a ridge-parallel strike-slip fault off the transform system in the Gulf of California, *Geoph. Res. Lett*., vol. 37, 6, doi: 10.1029/2009GL042208.

Oskin, M., J.M. Stock, and A. Martín-Barajas, 2001, Rapid localization of Pacific–North America plate motion in the Gulf of California, *Geology,* 29, 459–462, doi: 10.1130/0091-7613(2001)029<0459: RLOPNA>2.0.CO;2.

Petersen, M.D., 2008, United States National Seismic Hazard Maps: U.S. Geological Survey Fact Sheet 2008–3017, 4 pp.

Plattner, C., R. Malservisi, T.H. Dixon, P. LaFemina, G.F. Sella, J. Fletcher, and F. Suarez-Vidal, 2007, New constraints on relative motion between the Pacific plate and Baja California microplate (Mexico) from GPS measurements, *Geophy. J. Int.*, 170, no. 3, 1373–1380, doi:10.1111/j.1365-246X.2007.03494.x.

Ramos E., 1998, Características de la deformación en las rocas cristalinas cretásicas de la región E-SE de la ciudad de la Paz, BCS, México, *MS thesis*, CICESE, México (in spanish).

Servicio Geológico Mexicano, 1996, Geologic map, San Antonio, F12-B14, Baja California Sur, México, scale 1: 50,000.

SGM, 1999. Servicio Geológico Mexicano, Geologic map, La Paz, G12-10-11, Baja California Sur, México, scale 1: 250,000.

SGM, 2000. Servicio Geológico Mexicano, Geologic map, San Juan de Los Planes, F12-B14, Baja California Sur, Mexico, scale 1: 50,000.

SGM, 2001. Servicio Geológico Mexicano, Geologic map, Todos Santos, F12-B33, Baja California Sur, México, scale 1: 50,000.

SGM, 2002. Servicio Geológico Mexicano, Carta geológica – minera San Jose del Cabo, F12-2-3-5-6, Baja California Sur, Mexico, scale 1: 250,000.

SGM, 2008. Servicio Geologico Mexicano, Geologic map, La Paz, Baja California Sur, México, scale 1: 50,000.

Stirling M., and M. Gerstenberg, 2018, Applicability of the Gutenberg-Richter relation for major active faults in New Zealand, Bull. Seism. Soc. Am., 108, no. 2, 718-728, doi: 10.1785/0120160257.

Stock, J.M., and K.V. Hodges, 1989, Pre-Pliocene extension around the Gulf of California and the transfer of Baja California to the Pacific plate, *Tectonics*, 8, no. 1, 99–115, doi:10.1029/TC008i001p00099.

Suter, M., 2018, The historical seismicity of the Loreto region, Baja California peninsula, Mexico (1684-1778), *Seism. Res. Lett*, 89, 1, 202-209.

Umhoefer, P.J., L. Mayer, and R.J. Dorsey, 2002, Evolution of the margin of the Gulf of California near Loreto, Baja California peninsula, Mexico, *Geol. Soc. of Am. Bull.* 114, 849–868, doi:10.1130/0016-7606(2002)114<0849: EOTMOT>2.0.CO;2.

Umhoefer, P.J., F. Sutherland, G. Kent, A. Harding, D. Lizarralde, T. Schwennicke, J. Fletcher, W.S. Holbrook, and G. Axen, 2008, Synchronous changes in rift- margin basins and initiation of the Alarcón spreading ridge and related transform fault, southwestern Gulf of California*, Geol. Soc. Am. Abstracts with Programs*, 40, no. 6, 151p.

Wei, S., E. Fielding, S. Leprince, A. Sladen, J.P. Avouac, D. Helmberger , E. Hauksson, R. Chu, M. Simons, K. Hudnut, T. Herring and R. Briggs (2011), Superficial simplicity of the 2010 El Mayor-Cucapah earthquake of Baja California in Mexico. *Nature Geoscience*. doi:10.1038/ngeo1213, 2011.

Wells, D.L. and K.J. Coppersmith, 1994, New empirical relationships among magnitude, rupture length, rupture witdh, rupture área and surface displacement, *Bull. Seism. Soc. Am*. 8, no. 4, 974 -1009.

Wesnousky, S., 1986, Earthquakes, quaternary faults, and seismic hazard in California, *J. of Geophy. Res*. 91: doi:10.1029/0JGREA000091000B12012587000001.

Woessneser J. and S. Wiemer, 2005, Assessing the quality of earthquake catalogs: Estimating the magnitude of completeness and its uncertainty, *Bull. Seim. Soc. Am.* 95, 684-698.

Wiemer S., 2001, A software package to analyze seismicity: ZMAP, Seism.Res. Lett. 72, 373-382.

Geofísica Internacional (2019) 58-2: 169-178

Original paper

# Coseismic displacements and Mw estimation of the El Mayor-Cucapah earthquake, Mexico, from GPS source spectra

J. Carlos Robles-Avalos, J. Alejandro González-Ortega*, J. Javier González-García and J. Antonio Vidal-Villegas

Received: August 10, 2018; accepted: November 20, 2018; published on line: April 01, 2019
DOI: http://dx.doi.org/10.22201/igeof.00167169p.2018.58.2.1968

**Resumen**

El sismo de magnitud Mw 7.2 El Mayor-Cucapah ocurrió el 4 de abril de 2010 en el Valle de Mexicali, cerca de la frontera entre California USA y Baja California, México. El objetivo del presente trabajo fué examinar el GPS como una herramienta complementaria en estudios sísmicos y estimar el momento sísmico del sismo y su magnitud Mw. Para ello se exploró la capacidad de los datos de GPS de alta frecuencia (5Hz) localizados en el norte de la ruptura sísmica para obtener la cinemática de los desplazamientos cosísmicos. Los datos GPS se procesaron utilizando el método de Posicionamiento Puntual Preciso con el software GIPSY-OASIS II, posteriormente se aplicó la Transformada Rápida de Fourier a las series de tiempo de posición, se calcularon los parámetros espectrales, momento sísmico y Mw. Se encontró una buena concordancia en términos de correlación de la señal de los desplazamientos GPS comparando los registros sísmicos de movimientos fuertes integrados al desplazamiento, utilizando parámetros de filtrado para dos conjuntos de instrumentos. Los espectros de desplazamiento cinemático GPS muestran un nivel de desplazamiento espectral de baja frecuencia (~0.2 Hz) cuando se compara con la doble integración de los datos de movimientos fuertes. Es fácil calcular el movimiento cosísmico estático a partir de los datos GPS. Sin embargo es muy difícil calcularlos a partir de los datos de movimientos fuertes. Un modelo simple de fuente sísmica es adecuado para el conjunto de datos GPS utilizados en este trabajo, se estimó Mw=7.19±0.13, que concuerda con el Mw 7.2 obtenido en otros estudios del sismo de El Mayor-Cucapah.

Palabras clave: Cinemática de desplazamiento cosísmico, Sismología GPS, Posicionamiento Puntual Preciso, Análisis Espectral, sismo El Mayor-Cucapah, Sismogeodesia.

**Abstract**

El Mayor-Cucapah earthquake Mw 7.2 on April 4, 2010, occurred on Mexicali Valley near the international border between California, USA and Baja California, Mexico. The objective of this paper was to examine GPS as a complementary tool for seismic studies and to estimate earthquake seismic moment and Mw. For this purpose the capabilities of high-rate GPS (5 Hz) data located in the northern part of the seismic rupture has been explored to obtain the kinematic coseismic displacements. GPS data were processed using Precise Point Positioning method with GIPSY-OASIS II software, then applying the Fast Fourier Transform to the position time series, spectral parameters, seismic moment and Mw were calculated. A good agreement was found in terms of signal correlation of the GPS displacements, by comparing strong-motion seismic records integrated to displacement, using filtering parameters for two sets of instruments. Kinematic GPS displacement spectra clearly shows the low frequency displacement spectral level (~0.2 Hz) when compared with double integration of strong-motion data. It is easy to calculate the static coseismic motion from GPS data, however it is very difficult to calculate it from strong-motion data. A simple earthquake source model is suitable for the GPS dataset used in this work, estimated on Mw=7.19±0.13, was in according with Mw 7.2 obtained in other studies of the El Mayor-Cucapah earthquake.

Key words: Kinematic coseismic displacement, GPS Seismology, Precise Point Positioning, Spectral Analysis, El Mayor-Cucapah earthquake, Seismogeodesy.

J. C. Robles-Avalos
Posgrado en la División de Ciencias de la Tierra
Centro de Investigación Científica
y de Educación Superior de Ensenada
Baja California, Ensenada
B.C. México

J. A. González-Ortega*
J. J. González-García
J. A. Vidal-Villegas
Departamento de Sismología
División de Ciencias de la Tierra
Centro de Investigación Científica
y de Educación Superior de Ensenada
Baja California, Ensenada
B.C. México
*Corresponding author: aglez@cicese.mx

## Introduction

El Mayor-Cucapah earthquake has provided an important opportunity to study about the geodynamics of the northwest region of Mexico (Fletcher *et al*., 2016), as spatial and tectonic geodesy (Wei *et al*., 2011). The use of GPS in seismology was first documented by Hirahara *et al*., (1994), Ge *et al*., (2000) and Nikolaidis *et al*., (2001), who demonstrate the potential of GPS as a seismological instrument. For instance, Larson *et al*., (2003) using GPS (1 Hz) achieved to observe the kinematic displacements of the Alaska Denali earthquake (*Mw* 7.9) in 2002, suggesting that GPS observations are crucial to study rupture processes. Miyazaki *et al*., (2004) compared displacements from GPS with the double integration of the acceleration records, finding a good correlation between both for the Tokachi-Oki earthquake (*Mw* 8.3, occurred in 2003). Blewitt *et al*., (2006) demonstrated the GPS ability to estimate the magnitude of a megathrust earthquake, using data from up to only a few minutes after earthquake initiation, as well as its high tsunamigenic potential for the Sumatra–Andaman earthquake (*Mw* 9.2-9.3) in 2004; whereas, Hung *et al*., (2017) shown that 5 Hz high-rate GPS observations is an optimal sampling rate for GPS seismology as observed for the Ruisi Taiwan earthquake occurred in 2013. Nowadays, broadband and/or strong-motion seismic instruments located with high-rate GPS receivers are the best instrumental candidates to measure the complexity in the seismic source, rapid slip characterization of finite fault rupture and also for applications on early seismic warning systems (Melgar *et al*., 2013; Bock *et al*., 2011; Bock and Melgar, 2016).

Northern Baja California tectonics is primary dominated by right-lateral strike slip of ~50 mm/yr along southernmost San Andreas Fault system, between the Pacific and North American plates (Argus *et al*., 2010; DeMets *et al*., 2010) (Figure 1-inset). The El Mayor-Cucapah earthquake (32.278° N, 115.339° W; 4 km Depth; Mw 7.1; To=2010-04-04 22:40:40 UTC; RESNOM Database) of April 4, 2010, Mw 7.2, had a complex bidirectional rupture divided into two main domains from the epicentral zone located in the southeast corner of the Sierra Cucapah mountain range (Hauksson *et al*., 2010; Fletcher *et al*., 2014). The rupture in the northern section spread through the Cucapah mountains by several multiple faults-segments: Pescadores, Borrego, Paso Superior e Inferior. While in the southern section it extended through the Colorado River Delta, where it was possible to identify a new fault named Indiviso. The extent of the rupture was around 120 km (Figure 1) (González-García *et al*., 2010; Wei *et al*., 2011, Fletcher *et al*., 2014).

The characterization of a seismic source depends primarily on the direction of propagation of the seismic waves, distribution of the rupture and the magnitude of the coseismic displacements (Hanks, 1981). One way to estimate earthquake source parameters (seismic moment, stress drop and source radius) is computing the Fast Fourier Transform (FFT) to the displacements in the far-field (Savage, 1972), and getting the spectral parameters (level at low frequencies, corner frequency and slope to high frequencies), to obtain the seismic moment ($M_0$) (Brune, 1970), and then the moment magnitude (Mw) (Hanks and Kanamori, 1979) of an earthquake.

High-rate GPS (from 1-10 Hz) displacements has been proved very useful for monitoring long-period ground motion, moreover, the optimal combination of near-source GPS and seismic strong-motion data covers a broad spectrum of coseismic motion, from high frequencies to long periods (Bock and Melgar, 2016). Taking advantage of the availability of high-rate GPS records (5 Hz) nearby the seismic rupture of the El Mayor-Cucapah earthquake, the position ground motion was obtained, and then the results were compared with the double integration of acceleration data, for two sets of located (close to each other) GPS and strong-motion instruments. In the case of acceleration data a first order Butterworth filter was used within 0.10 – 50 Hz (Bendat and Piersol, 2011; Oppenheim and Shafer, 2011) in the frequency domain, while not for the GPS position. Finally, the earthquake seismic moment was estimated using a simple earthquake source model (Brune, 1970; Kumar *et al*., 2012) and moment magnitude was obtained following Hanks and Kanamori (1979).

## Data and Methods

High-rate GPS (5Hz) data were used from the Plate Boundary Observatory GPS network (Figure 1), obtained through the University NAVSTAR Consortium (UNAVCO) and acceleration data from Southern California Earthquake Data Center (SCEDC), and Center for Engineering Strong Motion Data (CESMD) for the El Mayor-Cucapah earthquake.

The technique used to process the GPS data was Precise Point Positioning (PPP) with GIPSY-OASIS software (Zumberge *et al*., 1997; Kouba and Heroux 2001). PPP is a positioning technique that is based on precise

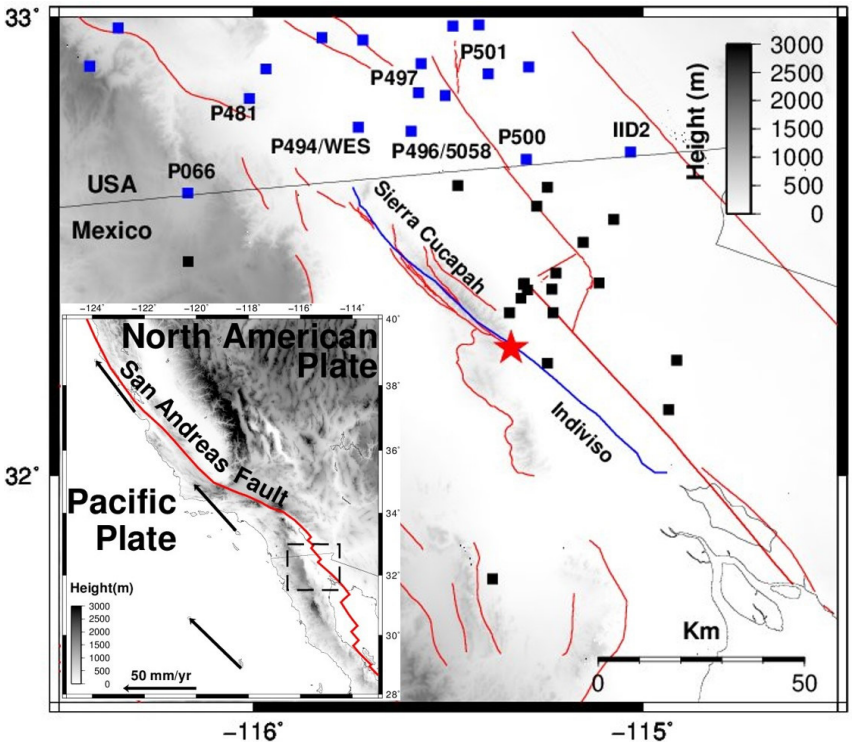


**Figure 1.** Tectonic setting of the north Baja California region, where the El Mayor-Cucapah earthquake occurred. The red star denotes the earthquake epicenter. Blue line denotes the surface rupture [Fialko *et al.,* 2010] and red lines denote known active faults. Blue squares denote GPS continuous recording sites in USA during the earthquake occurrence and black squares are GPS temporal surveyed sites after the earthquake (González-Ortega *et al*., 2014). P494/WES and P496/5058 are colocated GPS and strong-motion instruments; as well as, P066, P481 P497, P50, P500 and IID2 are GPS stations used in the present study. Inset illustrates a broader tectonic setting of the study area. Black vectors shows the tectonic motion with respect to North American Plate.

position coordinates obtention for a single station without a reference station, using precise orbit products and clock corrections provided by the International GNSS Service (IGS) (Abdallah and Schwieger, 2014). This technique can be used for both kinematic and static GPS processing. To achieve centimeter-level accuracy estimates, several modeling effects must be taken into account, such as the atmospheric effects on the carrier phase, as well as terrestrial and oceanic tides (Heroux *et al*., 2001). Thus, from far-field displacements in the frequency domain, earthquake seismic moment and magnitude can be obtained (Hanks and Wyss, 1972; Johnson and McEvilly, 1974).

The simplest and widely used earthquake source models are those proposed by: Haskell (1964) and Brune (1970). In the Haskell's model, two corner frequencies $f_r = \frac{2}{t_r}$ and $f_d = \frac{2}{t_d}$ are defined. Where $t_r$ is rupture time and $t_d$ is rise time. The spectrum is flat for frequencies less than $f_r$, then goes as $f^{-1}$ between $f_r$ and $f_d$, to finally decay as $f^{-2}$ for high frequencies. Thus the spectrum is parametrized by three factors, seismic moment Mo, raise time $t_d$ and rupture time $t_r$ (Stein and Wysession, 2003). The Brune's model has a single corner frequency, $f_c$, that combines the effects of rise and rupture time. The amplitude spectrum corresponds to displacements observed in the far-field; however, it is also applicable for observations in the near-field as long as the source-receiver distance is greater than the wavelength of the seismic waves (Madariaga, 1989). In the present case, a wavelength of ~26 km is obtained when considering seismic wave velocity of 3.3 km/s (Fuis *et al*., 1982) and 8 s period of the first oscillation for P494 station (Figure 2).

One of the most important spectral parameter is the flat line-segment of the amplitude spectrum at low frequencies as proposed by Haskell (1964) and Brune (1970). This frequency line-segment is commonly referred as $\Omega_0$, spectral level to low frequencies, from this parameter seismic moment is (Brune, 1970; Archuleta *et al*., 1982),

$$M_o = \frac{\Omega_0}{F_s R_{\theta\phi}} 4\pi\rho R\beta^3 \quad (1)$$

Where $\Omega_0$ is the line-segment at low frequencies, $R_{\theta\phi}$ is the average radiation pattern for *S* waves (~0.6), $\rho$ is the density of the medium (2.75 $\frac{g}{cm^3}$) and $\beta$ the s-wave velocity (3.3 x $10^5$ $\frac{cm}{s}$ ) (Fuis *et al*., 1982), $R$ is the distance from the hypocenter to the observation site and $Fs$ is the free surface factor (2). Finally, we used the moment magnitude relation proposed by Hanks and Kanamori [1979], in which *Mo* is in units of dyne-cm,

$$Mw = \frac{2}{3} logM_o - 10.7 \quad (2)$$

**Results**

GPS position time series corresponding to the nearest sites to the earthquake rupture are shown in Figure 2. The kinematic displacement generated by the passage of the seismic waves can be observed, as well as the coseismic permanent displacement, derived from the surface motion of the El Mayor-Cucapah earthquake. Differences in amplitude and oscillation are due to the type of soil and epicentral distance. P494 is located ~65 km from the epicenter in the west Salton Sea basin; while P481 is ~87 km in the Peninsular Ranges. To estimate the coseismic displacements, the linear trend of the surperficial pre-arrival seismic wave was first calculated and then the entire record of the

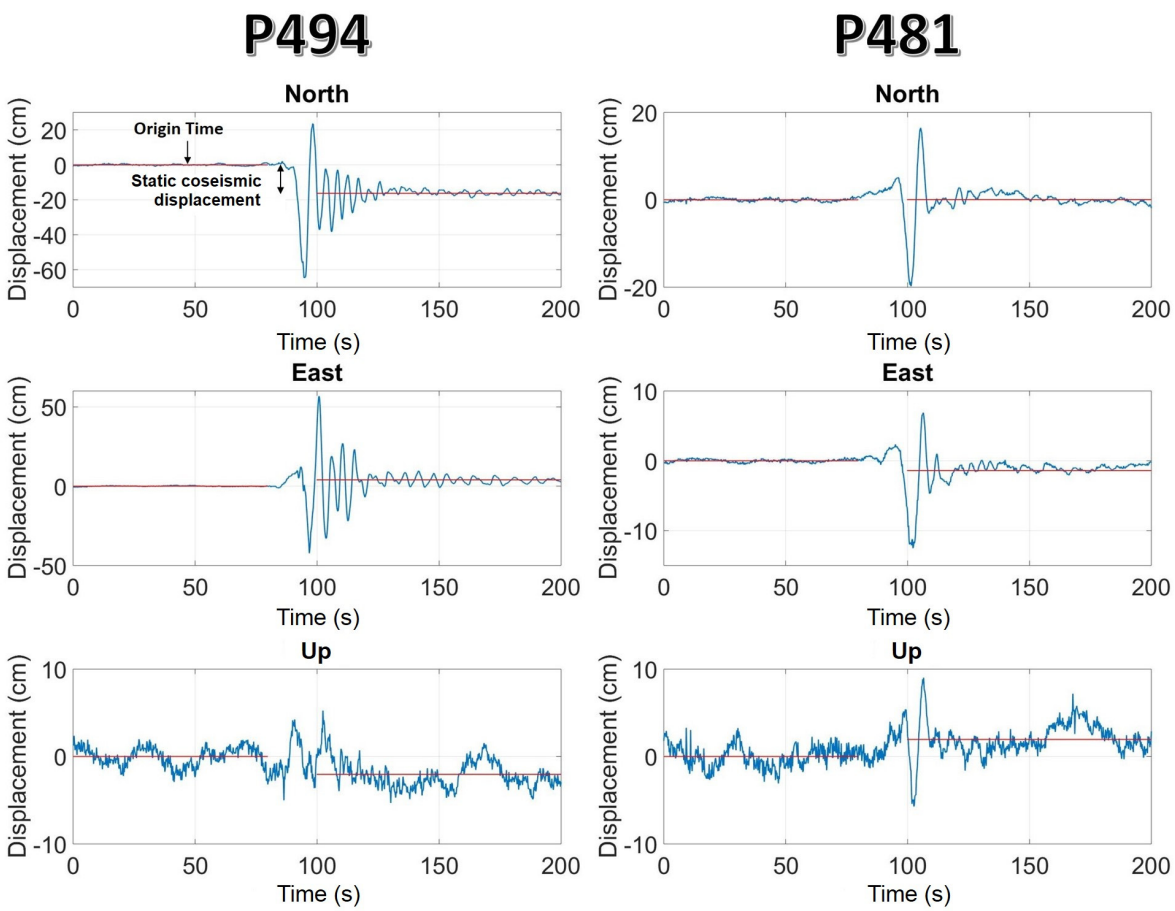


**Figure 2.** GPS position time series. Left column, GPS site P494, ~65 km from epicenter. Right column, GPS site P481, ~87 km from epicenter. Red lines indicate linear detrend removed before and after the S-wave arrival to estimate the static coseismic offsets.

position time series. Subsequently, the mean of the oscillations of the pre-arrival and post-arrival segments was calculated, the difference between both segments corresponds to the static (permanent) coseismic displacement. In Table 1, the kinematic and static coseismic displacements for GPS sites processed in this study are presented.

GPS position time series were compared with the displacement series obtained from the double integration of the accelerometer records from WES and 5058 accelerograph stations, located at <1 km from GPS sites P494 and P496, respectively (Figure 3). Horizontal components show alignment in phase and similarity in amplitudes (see inset plots). For strong-motion data several tests to find the frequency range and order for the Butterworth filter were performed. First-order Butterworth bandpass filter was selected, from 0.08 and 0.20 to Nyquist frequency for WES and 5058 respectively. This type of filter allows to improve the position of the time series and to carry out the comparison with GPS position time series. High order Butterworth filters tend to generate biases in position baseline and cause distortions [Oppenheim and Schafer, 2011].

To compare the kinematic GPS displacements and double integrated accelerogram data, a normalized cross-correlation was used. In general, correlation values are better in the east-west (>0.90) than north-south (>0.70), due to the smaller kinematic coseismic displacement in the east-west direction. Consequences of seismic filtering tends to diminish the amplitudes of the displacement series obtained from

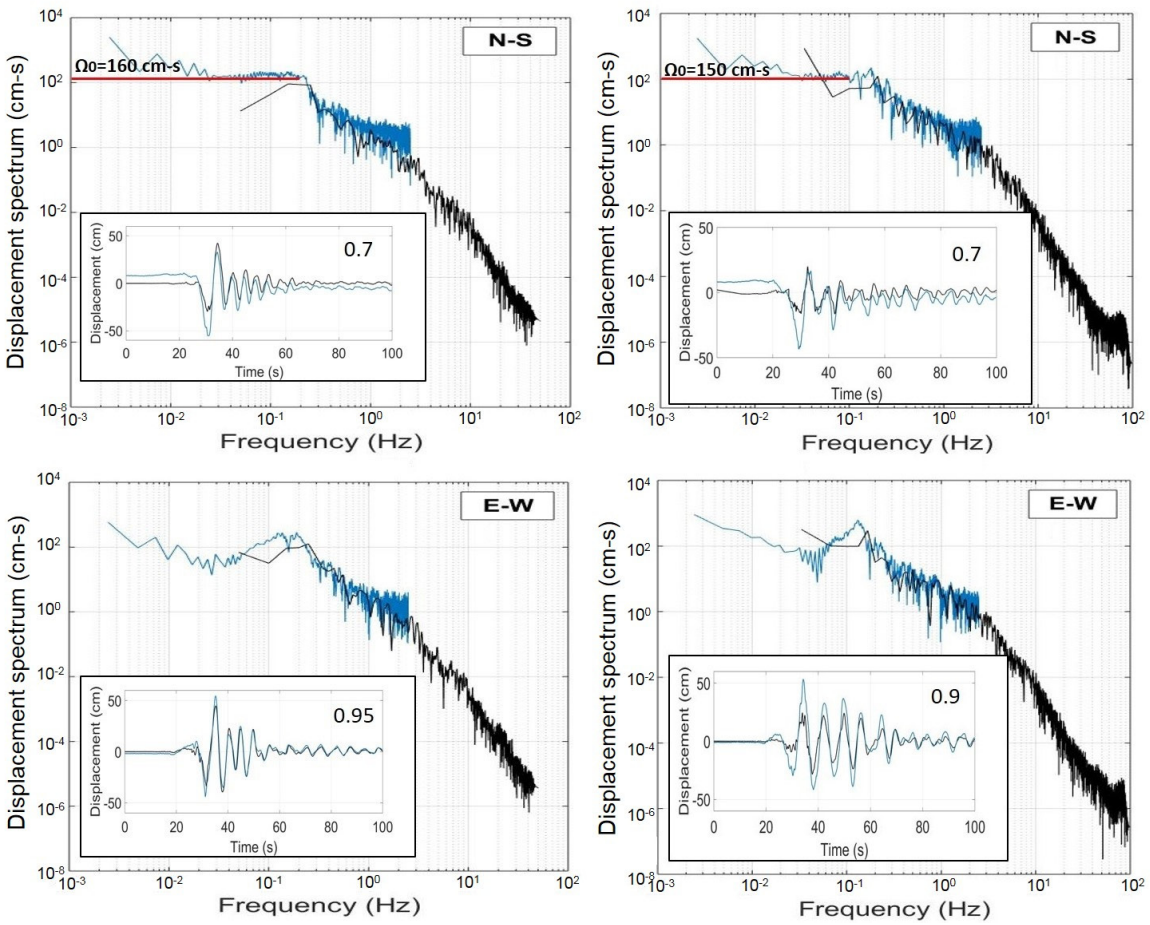


**Figure 3.** Displacement spectrum comparisons from collocated strong motion (black) and high-rate GPS (blue). Left column, horizontal displacement spectrum at P494-GPS and WES accelerograph station. Right column, horizontal displacement spectrum at P496-GPS and 5058 accelerograph station. Red horizontal lines indicate $\Omega_0$ value. Insets show comparison between GPS and integrated (from strong-motion) time series displacement and corresponding cross-correlation values estimate.

**Table 1.** 3D Coseismic displacements estimates from GPS position time series. Includes earthquake distance to GPS sites, peak-to-peak oscillation seismic wave motion, flat line segment amplitude value at low frequencies $\Omega_o$, $M_o$ and $M_w$.

| GPS site | Lat. | Long. | Epicentral distance (km) | Kinematic peak to peak oscillation, north (cm) | Kinematic peak to peak oscillation, east (cm) | Kinematic peak to peak oscillation, Up (cm) | Static coseismic north (cm) | Static coseismic east (cm) | Static coseismic Up (cm) | $\Omega_o$ (cm-s) | $M_o$ (dyne-cm) 1x10$^{26}$ | $M_w$ |
|---|---|---|---|---|---|---|---|---|---|---|---|---|
| P494 | 32.760 | -115.732 | 65 | 90 | 100 | 10 | -18 | 4 | ~ -1 | 160 | 10.8 | 7.32 |
| P496 | 32.751 | -115.596 | 58 | 60 | 95 | 24 | -17 | ~2 | ~0 | 150 | 9.0 | 7.27 |
| P497 | 32.835 | -115.577 | 67 | 40 | 60 | 15 | -9 | ~1 | ~1 | 125 | 8.7 | 7.26 |
| P501 | 32.876 | -115.398 | 67 | 45 | 36 | 10 | -5 | ~2 | ~1 | 137 | 9.5 | 7.29 |
| P500 | 32.690 | -115.300 | 46 | 26 | 30 | 12 | -4 | 5 | ~0 | 93 | 4.4 | 7.06 |
| IID2 | 32.706 | -115.032 | 54 | 16 | 21 | NA | ~ -2 | 3 | ~0 | 77 | 4.3 | 7.06 |
| P481 | 32.822 | -116.012 | 87 | 36 | 20 | 15 | ~ -2 | ~ -1 | ~0 | 74 | 6.7 | 7.18 |
| P066 | 32.617 | -116.170 | 90 | 16 | 11 | 13 | ~0 | -7 | ~0 | 51 | 4.8 | 7.08 |

accelerogram double integration data when compared to those obtained with GPS. Static coseismic displacements are not observable in strong-motion due to wideband limitation but in GPS these are clearly captured.

Figure 3 shows horizontal GPS and strong-motion source spectra comparison for P494-GPS and WES, as well as, P496-GPS and 5058. With GPS spectra, the amplitude at low frequencies $\Omega_0$ is easily identified. After a value of ~0.2Hz, amplitudes decay at $f^{-2}$ as frequency increases up to where GPS spectra turns constant. At this point, seismic oscillations with spectral amplitudes of ~2cm·s associated with frequency values ~1Hz (periods ≥ 1 s for 5Hz GPS sampling rate), are not detectable with GPS. On the other hand, with strong-motion displacement spectra, two corner frequencies at ~0.2Hz and ~3Hz can be identified. For frequencies >3Hz amplitude decay as $f^{-4}$. These amplitude decays are related to attenuation and site effects [Shearer, 1999].

Seismic moment ($M_o$) and moment magnitude ($M_w$) of the El Mayor-Cucapah earthquake is $M_o$ = 7.3±3.5x10$^{26}$ dyne-cm, $M_w$ = 7.19±0.13 using GPS spectra (Table 1), and *Mo* = 6.4±0.07x10$^{26}$ dyne-cm, $M_w$ = 7.14±0.01, using WES and 5058 strong-motion data spectra. These values are similar to estimates obtained from seismic and geodetic data inversion $M_o$ = 9.9x10$^{26}$ dyne-cm, $M_w$ = 7.26 [Wei *et al*., 2011] and from field measurements of $M_o$ = 7.2x10$^{26}$ dyne-cm, $M_w$ = 7.17 [Fletcher *et al*., 2014].

Figure 4 shows the El Mayor-Cucapah static coseismic horizontal displacements. The maximum horizontal static coseismic displacement is ~1.16 m, in the N137°E direction, ~8 km from the epicenter, in the southeastern part of the Sierra Cucapah, and the maximum vertical displacement is ~-0.64 m. The displacement pattern, clearly observed in the northeast is consistent with a right-lateral focal mechanism of The El Mayor-Cucapah earthquake (González-Ortega *et al*., 2014). These authors, estimated earthquake moment magnitude using dislocation inversion methods from a finite coseismic slip model composed of several fault segments using GPS and InSAR static displacements in a homogeneous (Fialko *et al.,* 2010) and in an layered earth structure [Huang *et al*., 2016].

## Discussion

Zheng *et al*., (2012), also used high-rate GPS data with the aim of carrying out the seismotectonics analysis of El Mayor-Cucapah earthquake with different methodology as in this work. They used the Cut and Paste method (CAP) developed by Zhu and Helmberger (1996), which allows separating the $P_n$ and surface waves independently, not requiring an accurate crustal velocity model or a high number of stations, but a good azimuthal coverage for the focal mechanism inversion and earthquake magnitude. Also, Allen and Ziv (2011), re-processed in a simulated real-time high-rate GPS static displacement data, to estimate earthquake magnitude via static slip inversion, using preliminary earthquake hypocenter from seismic data and a catalog of active faults, for the purpose of earthquake early warning system test in southern California.

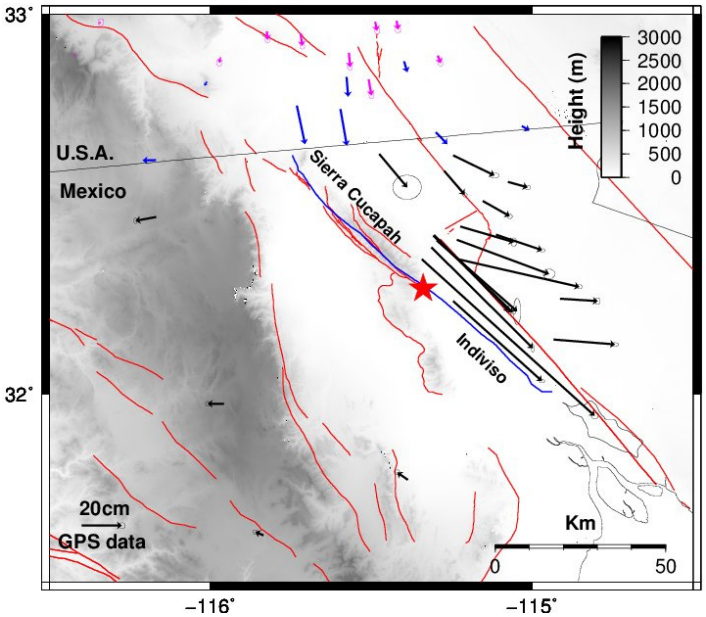


**Figure 4.** GPS horizontal coseismic displacements from El Mayor-Cucapah earthquake. Blue vectors are estimates obtained in this study. Black are displacements from Gonzalez-Ortega (2014), and magenta are from GPS Explorer Data Products (http://geodemo-c.ucsd.edu). The red star denotes the earthquake epicenter. Blue line denotes the surface rupture [Fialko *et al.,* 2010] and red lines denote known active faults.

Differences between Zheng *et al*., (2012), and the present work lies in the GPS data processing; while we used the PPP technique, they used the Double Differences (DD). For the DD technique (Herring *et al.*, 2015) it is necessary to have a reference station, which must be located at a distance far enough to not be affected by seismic waves, but close enough to act as reference station which guarantees the same satellites observation of the sites of interest. Such condition is not required with PPP technique, as it uses precise GPS orbit and clock data products with centimeter accuracy. Although the methodology used in Zheng *et al*., (2012) and the present one differ in estimating GPS time series and seismic moment, in general, position time series and moment magnitude results are very similar and confirm earlier studies using GPS high-rate data from El Mayor-Cucapah earthquake (Allen and Ziv, 2011; Bock *et al.*, 2011).

With high-rate GPS spectral analysis, amplitude at low frequencies is clear to identify in contrast to accelerogram data. This flat low frequency section is associated with large displacement amplitudes generated by the passage of surperficial seismic waves (Udias, 1989). Thus, estimates of $M_o$ and $M_w$ can have a greater degree of certainty with GPS data than with accelerometer records. GPS data can be of crucial importance for estimating major earthquake magnitude in real time (Blewitt *et al.*, 2006; Bock and Melgar, 2016). According to the present results, average $\Omega_0$ value with GPS data is 115±4 cm-s, while with accelerogram data is 90±8 cm-s. However, as GPS is sampled at 5 Hz, for frequencies >2.5 Hz (Nyquist frequency) GPS is unable to observe spectral displacements below 2 cm-s, which does not happen with the acceleration records. This highlights the importance of the complementarity between both instruments, closely located GPS and strong-motion, for near field displacements earthquake studies.

## Conclusion

High-rate (5 Hz) kinematic GPS position time series of the El Mayor-Cucapah earthquake were studied and compared to the displacement series obtained from the double integration of strong-motion data. The comparison shows good agreement in terms of cross-correlation, for P494-GPS and WES, and, P496-GPS and 5058, instruments at ~75 km from epicenter. Kinematic GPS data at low frequencies, associated with large spectrum displacements, help to clearly identify the flat line segment amplitude better than accelerogram data, and thus using a simple earthquake source model the earthquake seismic moment, Mo=7.3±3.5x$10^{26}$ dyne-cm, Mw=7.19±0.13 could be estimated, similar

to Mw 7.2 as previously reported using other methodologies. Static coseismic displacements are very difficult to obtain from accelerogram data, however with GPS data, these are easily obtained and consistent with the right-lateral strike-slip mechanism of the El Mayor-Cucapah earthquake.

## Data and Resources

High-rate GPS data can be found at UNAVCO, ftp://data-out.unavco.org/pub/highrate/5-Hz/rinex/ (last accessed April 2018). Coseismic displacements from the northern side of the El Mayor-Cucapah rupture can be found at GPS Explorer, http://geodemo-c.ucsd.edu (last accessed April 2018). Accelerometric data can be found at SCEDC, http://scedc.caltech.edu/research-tools/waveform.html (last accessed April 2018) and CESMD, https://www.strongmotioncenter.org/cgi-bin/CESMD/search_options.pl (last accessed April 2018). Map figures were generated by Generic Mapping Tool (GMT) software [Wessel *et al*., 2013].

## Acknowledgments

The authors would like to thank Editor Dr. Manuel Berrocoso-Dominguez and two anonymous reviewers for their valuable suggestions. This work was partially financially supported by CONACyT though a graduate scholarship to Robles-Avalos J.C. (2015-2017). We thank Dr. Sara Ivonne Franco Sánchez and Dr. Luis Mungía Orozco for their comments during this work. Also we acknowledge to local people during the GPS campaigns in northern Baja California.

## References

Abdallah, A. and Schwieger, V. (2014). Accuracy Assessment Study of GNSS Precise Point Positioning for Kinematic Positioning. In Schattenberg, J., Minßen, T. F.: Proceeding on 4th International Conference on Machine Control and Guidance (MCG), Braunschweig: Institut für mobile Maschinen und Nutzfahrzeuge, Braunschweig, Germany.

Allen, R. M. and Ziv, A. (2011). Application of Real-Time GPS to earthquake early warning. Geophysical Research Letters, 38, L16310.

Archuleta, R. J., Cranswick, E., Mueller, C., and Spudich, P. (1982). Source parameters of the 1980 Mammoth Lakes, California, earthquake sequence. Journal of Geophysical Research: Solid Earth, 87(B6), 4595-4607.

Argus, D.F., Gordon, R.G., Heflin, M.B., Ma, Ch., Eanes, R.J., Willis, P., Peltier, W.R. and Owen, S.E. (2010). The angular velocities of the plates and the velocity of Earth's center from space geodesy. Geophysical Journal International, 180(3), 913-960.

Bendat, J.S., Piersol, A.G. (2011). Random Data: Analysis and Measurement Procedures. John Wiley & Sons. 640 pp.

Blewitt, G., Kreemer, C., Hammond, W. C., Plag, H. P., Stein, S., and Okal, E. (2006). Rapid determination of earthquake magnitude using GPS for tsunami warning systems. Geophysical Research Letters, 33(11).

Bock, Y. and Melgar D. (2016). Physical applications of GPS geodesy: a review. Reports on Progress in Physics. 79, 106801, 119 p.

Bock, Y., Melgar, D., and Crowell B.W. (2011). Real-time strong motion broadband displacement from collocated GPS and accelerometers. Bulletin of the Seismological Society of America. 101(6). 2904-2925.

Brune, J. N. (1970). Tectonic stress and the spectra of seismic shear waves from earthquakes. Journal of Geophysical Research, 75(26), 4997-5009.

DeMets, C., Gordon, R.G. and Argus, D.F. (2010). Geologically current plate motions. Geophysical Journal International, 181(1), 1-80.

Fialko, Y., A. González, J. González, S. Barbot, S. Leprince, D. Sandwell, and D. Agnew (2010), Static rupture model of the 2010 Mw 7.2 El Mayor-Cucapah earthquake from ALOS, ENVISAT, SPOT and GPS data, Abstract T53B-2125 presented at 2010 Fall Meeting, AGU, San Francisco, Calif.

Fletcher, J., Teran, O.J., Rockwell, T. K., Oskin, M., Hudnut, K. W., Mueller, K. J. Spelz, R. M., Akciz, S. O., Masana, E., Faneros, G., Fielding, E. J., Leprince, S., Morelan, A. E., Stock, J. Lynch, D. K. Elliott, A. J., Gold, P., Liu-Zeng, J., González-Ortega, A. Hinojosa-Corona, A., and González-García, J. (2014). Assembly of a large earthquake from a complex fault system: Surface rupture kinematics of the 4 April 2010 El Mayor–Cucapah (Mexico) Mw 7.2 earthquake. Geosphere, 10 (4), 797-827.

Fletcher, J.M., M.E. Oskin, and Teran, O.J. (2016). The role of a keystone fault in triggering the complex El Mayor–Cucapah

earthquake rupture. Nature Geoscience, 9, 303–307.

Fuis, G.S., Mooney, W.D., Healey, J.H., McMechan G.A., and Lutter, W.J. (1982). Crustal structure of the Imperial Valley region. USGS professional paper 1254, 25-50.

Ge, L., Han, S., Rizos, C., Ishikawa, Y., Hoshiba, M., Yoshida, Y. and Himori, S. (2000). GPS seismometers with up to 20 Hz sampling rate. Earth, planets and space, 52(10), 881-884.

González-García, J. J., J. A. González Ortega, Y. Bock, Y. Fialko, E. J. Fielding, J. Fletcher, J. E. Galetzka, K. W. Hudnut, L. Munguia, and S. M. Nelson. (2010). Seismotectonics of the 2010 El Mayor Cucapah—Indiviso earthquake and its relation to seismic hazard in southern California, Abstract T53B-2117 presented at 2010 Fall Meeting, AGU, San Francisco, Calif.

González-Ortega, A., Y. Fialko, D. Sandwell, F. Alejandro Nava-Pichardo, J. Fletcher, J. González-García, B. Lipovsky, M. Floyd, and G. Funning (2014), EL Mayor-Cucapah (Mw7.2) earthquake: Early near-field posteismic deformation from InSAR and GPSobservations, J. Geophys. Res. Solid Earth, 119, 1482-1472.

González-Ortega, J. A., (2014). Análisis sismo-geodésico del sismo El Mayor-Cucapah (Mw=7.2) del 4 de abril de 2010, Baja California Tesis de doctorado en ciencias. Centro de Investigación Científica y de Educación Superior de Ensenada, Baja California.

Hanks, T. (1981). The Corner Frequency Shift, Earthquake Source Models, and Q. Bulletin of the Seismological Society of America. 71 (3); pp. 597-612.

Hanks, T. and Kanamori, H. (1979). A moment magnitude scale. Journal of Geophysical Research. 84(B5), 2348–2350.

Hanks, T. and Wyss, M. (1972). The use of body-wave spectra in the determination of seismic-source parameters. Bulletin of the Seismological Society of America, 62(2), 561-589.

Haskell, N. (1964). Total energy and energy spectral density of elastic wave radiation from propagating faults. Bulletin of the Seismological Society of America, 54, 1811-1841.

Hauksson, E., Stock, J., Hutton, K., Yang, W., Vidal-Villegas, J.A. and Kanamori, H. (2010). The 2010 Mw 7.2 El Mayor-Cucapah Earthquake Sequence, Baja California, Mexico and Southernmost California, USA: Active Seismotectonics along the Mexican Pacific Margin. Pure Applied Geophysics. 168, 1255–1277.

Heroux, P., Kouba, J., Collins, P., and Lahaye, F. (2001). GPS carrier phase point positioning with precise orbit products. In Procedings of the KIS, 5-8. Pierre Heroux Geodetic Survey Division, Natural Resources Canada.

Herring, T. A., R. W. King, M. A. Floyd, and S. C. McClusky (2015). Introduction to GAMIT/GLOBK, Release 10.6, Mass. Inst. Of Technol., Cambridge, Massachusetts.

Hirahara, K., Nakano, T. and Hoso, Y. (1994). An experiment for GPS strain seismometer. In Proceeding of Japanese Symposium on GPS. pp. 67-75. 15-16 December, Tokio, Japan.

Huang, M.-H., E. J. Fielding, H. Dickinson, J. Sun, J. Alejandro González-Ortega, A. M. Freed, and R. Bürgmann (2016). Fault Geometry Inversion and Slip Distribution of the 2010 Mw 7.2 El Mayor-Cucapah Earthquake from Geodetic Data, J. Geophys. Res. Solid Earth, 121, 607-622.

Hung, H-K, Rau, R-J., Benedetti, E., Branzanti, M., Mazzoni, A., Colosimo, G., and Crespi, M. (2017). GPS Seismology for a moderate magnitude earthquake: Lessons learned from the analysis of the 31 October 2013 ML 6.4 Ruisui (Taiwan) earthquake. Annals of Geophysics, 60, 5, 2017; S0553.

Johnson, L. R., and McEvilly, T. V. (1974). Near-field observations and source parameters of central California earthquakes. Bulletin of the Seismological Society of America, 64(6), 1855-1886.

Kouba, J., and Heroux, P. (2001). Precise point positioning using IGS orbit and clock products. GPS solutions, 5(2), 12-28.

Kumar A., Kumar, A., Mittal, H., Kumar, A., and Bhardwaj, R. (2012). Software to Estimate Earthquake Spectral and Source Parameters. International Journal of Geosciences, 3, 1142-1149.

Larson, K. M., Bodin, P., and Gomberg, J. (2003). Using 1-Hz GPS data to measure deformations caused by the Denali fault earthquake. Science, 300(5624), 1421-1424.

Madariaga, R. (1989). Propagación de Ondas Sísmicas en el campo cercano. Física de la Tierra, 1, 51-73. Ed. Universidad Complutense Madrid.

Melgar, D., Crowell B.W., Bock Y. and Hasse J.S. (2013). Rapid modelling of the 2011 Mw 9.0 Tohoku-Oki earthquake with seismogeodesy. Geophysical Research Letters, 40(12).2963-2968.

Miyazaki, S. I., Larson, K. M., Choi, K., Hikima, K., Koketsu, K., Bodin, P. and Yamagiwa, A. (2004). Modeling the rupture process of the 2003 September 25 Tokachi Oki (Hokkaido) earthquake using 1 Hz GPS data. Geophysical Research Letters, 31(21).

Nikolaidis, R.M., Bock Y., de Jonge P.J., Shearer P., Agnew D.C. and Van Domselaar M. (2001). Seismic wave observations with the Global Positioning System. Journal of Geophysical Research, 106 (10) 21879-21916.

Oppenheim A., and Schafer R. (2011). Digital Signal Processing. Prentice-Hall of India Pvt. Limited. 585 pp.

Savage, J. C. (1972). Relation of corner frequency to fault dimensions. Journal of Geophysical Research, 77(20), 3788-3795.

Shearer P. (1999). Introduction to seismology. Cambridge University Press.

Stein, S., and Wysession, M. (2003). An introduction to seismology, earthquakes, and earth structure. Blackwell Pub.

Udias, A. (1989). Parámetros del foco de los terremotos. Física de la Tierra, 1, 87-104. Ed. Universidad Complutense Madrid.

Wei, S., Fielding, E., Leprince, S., Sladen, A., Avouac, J.P., Helmberger, D., Hauksson, E., Chu, R., Simons, M., Hudnut, K., Herring, T., Briggs, R. (2011). Superficial simplicity of the 2010 El Mayor–Cucapah earthquake of Baja California in Mexico. Nature Geoscience 4, 615-618.

Wessel, P., W. H. F. Smith, R. Scharroo, J. Luis, and F. Wobbe (2013), Generic mapping tools: Improved version released, EOS Trans. AGU, 94(45), 409–410.

Zheng, Y., Li, J., Xie, Z., Ritzwoller, M.H. (2012). 5 Hz GPS seismology of the El Mayor-Cucapah earthquake: estimating the earthquake focal mechanism. Geophysical Jounal International, 190, 1723-1732.

Zhu, L., and Helmberger, D. V. (1996). Advancement in source estimation techniques using broadband regional seismograms. Bulletin of the Seismological Society of America, 86(5), 1634-1641.

Zumberge, J. F., Heflin, M. B., Jefferson, D. C., Watkins, M. M., and Webb, F. H. (1997). Precise point positioning for the efficient and robust analysis of GPS data from large networks. Journal of Geophysical Research, 102(B3), 5005-5017.

Geofísica Internacional (2019) 58-2: 151-168

Original paper

# Probabilistic seismic hazard analysis in La Paz-Los Cabos, Mexico: The importance of active Quaternary fault segments

Roberto Ortega*, Dana Carciumaru, Edahí Gutierrez, Eduardo Huesca–Pérez and Luis Quintanar

Received: August 01, 2018; accepted: January 23, 2019; published on line: April 01, 2019
DOI: http://dx.doi.org/10.22201/igeof.00167169p.2018.58.2.1967

**Resumen**

Se presenta un estudio de Análisis Probabilístico de Riesgo Sísmico (PSHA) en el sur de la Península de Baja California, México. En este estudio se analizó la contribución de segmentos de falla del Cuaternario que incluyen dos fallas que han sido consideradas potencialmente activas por algunos autores, pero inactivas por otros, que son las fallas de La Paz y San José. Se probaron varios escenarios para comparar la estimación del riesgo con la contribución de dichas fallas y finalmente se propuso un árbol lógico para añadir las mentidumbres epistemicas. Adicionalmente se escogieron tres presas situadas alrededor del área de estudio, La buena Mujer, La Palma y Santa Inés. Los valores máximos de aceleración del suelo (PGA) se compararon por 50, 100, 200 años al 10.5 y 2% de excedencia. La combinación de periodos con niveles de porcentajes de excedencia se usaron como referencia para distintos grados de riesgo. El modelo escogido se presenta en un árbol de riesgo PSHA clásico. Contrariamente a lo esperado, no parece muy importante incluir todas las fuentes sísmicas como las fallas de La Paz y San José en la determinación de riesgo de diseño ingenieril, ya que en la región las fallas características son insensibles a las relaciones bajas. Sin embargo es solo un artefacto de la decisión arbitraria de utilizar periodos de retorno como grado de protección. Los resultados muestran que en el caso de construcciones esenciales, 2% de probablilidades de excedencia en 200 años lo mejor para esta región. Es necesario realizar estudios poleosísmicos en esta región para saber si estas fallas geologicas son activas ya que muchas estructuras importantes se encuentran cerca de las fallas estudiadas.

Palabras clave: peligro sísmico, sur de Baja California, atenuación sísmica.

**Abstract**

A study of Probabilistic Seismic Hazard Analysis (PSHA) in the southern part of the Baja California Peninsula, Mexico is presented. In this study, the contribution of Quaternary fault segments are analyzed including two faults that have been considered potentially active by some authors, but inactive by others, namely, La Paz and San José faults. Therefore, different scenarios were tested to compare the hazard estimation with the contribution of these faults and finally a logic tree was proposed to add the epistemic uncertainties. In addition, three dams situated around the study area were chosen: La Buena Mujer, La Palma and Santa Ines. The peak ground acceleration values (PGA) were compared for 50, 100 and 200 years at 10, 5 and 2% of exceedance. The combinations of periods with percentages of levels of exceedance were used as reference for different degrees of hazard assessments. The preferred model is presented in a classical PSHA logic tree. Contrary to expectations, it seems that it is not so important to include all the seismic sources as La Paz and San José faults in hazard assessment of engineering design because in this region the characteristic faults are not sensitive for lower rates. However, this is only a mere artifact of the arbitrary decision of using return periods as a degree of protection. The present results show that in the case of essential facilities 2% probability of exceedance in 200 years is the best for this specific region. It is necessary to perform paleoseismic studies in this region, to know if these geological faults are active because many important structures are located close to the studied faults.

Key words: seismic hazard, southern Baja California, seismic attenuation.

R. Ortega*
D. Carciumaru
Centro de Investigación Científica
y de Educación Superior de Ensenada
Unidad La Paz. Miraflores 334
La Paz 23050 BCS, México.
*Corresponding author: ortega@cicese.mx

E. Gutierrez
E. Huesca–Pérez
CONACYT
Centro de Investigación Científica
y de Educación Superior de Ensenada
Unidad La Paz. Miraflores 334
La Paz 23050 BCS, México.

L. Quintanar
Instituto de Geofísica
Departamento de Sismología
Universidad Nacional Autónoma de México
Ciudad Universitaria
Delegación Coyoacán, 04510
CDMX, México.

## Introduction

The La Paz-Los Cabos region is an active tectonic zone with little historical seismicity reported, (Ortega and González, 2007). This article is a long-term effort, started in 1995 when a major earthquake struck the southern part of Baja California Peninsula. From 1996 to 1997 the Centro de Investigación Científica y de Educación Superior de Ensenada, Baja California (CICESE) deployed a local seismic network. Later, a temporary strong motion network was in operation from 1998 to 2007 (Munguía *et al*., 2006; Ortega and González, 2007). Recently, CICESE installed seismic broadband stations within and around La Paz Bay. For 15 years, seismicity and attenuation relations that are the basic parameters for seismic hazard analysis are been studied. In this work, a probabilistic seismic hazard analysis for the southern part of the Baja California Peninsula is presented.

Particularly, the seismic sources that have been a topic of active discussions are studied. There has been a long debate on whether some fault segments should be considered active or not. Of special importance are La Paz and San José faults because they are the most prominent features of the region. Therefore, all the fault segments that have been reported and mapped by the Mexican Geological Service (SGM, Servicio Geológico Mexicano) are presented. For example, some authors, (Cruz-Falcón *et al*., 2010; Munguía *et al*., 2006) have reported the existence of La Paz fault, whereas others, (Busch *et al*., 2006; Busch *et al*., 2007; Maloney *et al*., 2007; Ramos 1998) say this fault does not exist. In addition, a common problem is that there are several faults which cannot be identified with a unique name. The purpose of this work is to compare the seismic hazard in different scenarios: a) using all faults, b) without La Paz Fault (WLP) and c) without the San Jose Fault (WSJ). It is important to note that in this article active Quaternary faults only those faults that have exhibited an observed movement or evidence of seismic activity during the last 20,000 years are called.

## Tectonic setting

The Gulf of California is an oblique – divergent plate boundary with active transtensional continental rifting (Busby and Ingersoll, 1995). Strike slip and normal faults systems accommodate the deformation in this region (Angelier *et al*., 1981; Fletcher and Munguía, 2000; Umhoefer *et al*., 2002; Plattner *et al*., 2007). Right lateral strike slip faults marked the extremities of the Gulf of California and they are separated by short spreading centers. On the east side of the southern part of Baja California peninsula an array of onshore to offshore faults north striking exists, left stepping and east dipping known as system of gulf margin (Fletcher and Munguía, 2000) (Figure 1).

During the continental rifting (DeMets, 1995; Fletcher and Munguía, 2000; Plattner *et al*., 2007; Lizarralde *et al*., 2007), starts the onset of seafloor spreading in the southern part of the Gulf of California (Lizarralde *et al*., 2007); Umhoefer *et al*., 2008). In this region, the fault system development could be studied during the transition of rift to drift process, when ocean spreading begun and continental rifting is active. Along the Alarcon rise in the southern Gulf of California the spreading rate is slower than across plate boundary of the Pacific – North America, indicating that structures along with transform faults and spreading centers in the gulf could finally accommodate deformation in this region (DeMets, 1995; Fletcher and Munguía, 2000; Plattner *et al*., 2007).

The seismicity data (Munguía *et al*., 2006) and geomorphic relationships (Fletcher and Munguía, 2000; Busch *et al*., 2006, 2007; Maloney *et al*., 2007) show that the normal faults array rupturing the southern tip of Baja California peninsula are still active and act as a shear zone which contributes to translating the peninsula blocks away from mainland Mexico (Plattner *et al*., 2007). The gulf – border is an extensional zone as well as an area of decreasing elevation and thinning crust (Lizarralde *et al*., 2007). The topography of the southern tip of the Baja California peninsula is controlled by normal faults which produced moderate sized earthquake (Fletcher and Munguía, 2000), whereas the gulf margin fault array has a minor contribution to the plate divergence in the region. The faults delineate Quaternary basins and offset Quaternary alluvial deposits (Fletcher and Munguía, 2000; Busch *et al*., 2006, 2007; Maloney *et al*., 2007).

During the Cenozoic, the western part of North America at the latitude of Baja California was the place of a subduction zone, where Farallon plate was subducting beneath Western North America (Stock and Hodges, 1989; Hausback, 1984). During Farallon plate subduction (Figure 1a), the Pacific plate, located west of the Farallon plate met the North America plate (Atwater, 1970; Stock and Hodges, 1989) and stopped the subduction in the north beginning the development of the Mendocino and Rivera triple junction

along southern California and northern Baja California (Gorbatov and Fukao, 2005).

While Mendocino triple junction moved northward the Rivera triple junction went southward lengthening the right lateral transform plate boundary that had initiated between Pacific and North America plates (Stock and Hodges, 1989). This right–lateral system developed marked the early stages of San Andreas system (Atwater, 1970). Between 20 and 12 Ma a series of microplates was formed along Baja California. The microplates were located within the Pacific Plate, and the trench was developed in a right lateral fault zone, known as the Tosco-Abreojos fault (Stock and Hodges, 1989). Between 12 and 6 Ma normal faults with NNW and N trend, developed the east of the Tosco-Abreojos fault (Figure 1b) adjacent to the west of the current Gulf region from California (Stock and Hodges, 1989; Hausback, 1984; Umhoefer *et al*., 2002). The system of normal faults that dominates the margin of the gulf was part of the distribution of the deformation between the Gulf of California and the Tosco-Abreojos fault (Stock and Hodges, 1989), the gulf margin system was part of a complex system of transtensional faults from 12 Ma (Fletcher *et al*., 2007). The regime of oblique-divergence started about 6 ago Ma, when small rift basins began to form in the current Gulf of California (Figure 1c). This oblique – divergence regime began as transform faults separated by rift basins (Fletcher and Munguía, 2000; Oskin *et al*., 2001; Fletcher *et al*., 2007). Along Alarcon Rise, the southernmost spreading center in the Gulf of California, new ocean crust started forming (DeMets, 1995; Umhoefer *et al*., 2008). Nowadays, the Gulf of California continues to be an oblique divergent continental rifting (Fletcher and Munguía, 2000; Umhoefer *et al*., 2002; Mayer and Vincent, 1999; DeMets, 1995).

## Method

In this study, a classical approach for Probabilistic Seismic Hazard Analysis (PSHA) was used based on a three-step procedure (Cornell, 1968; Algermissen *et al*., 1990; Algermissen and Perkins, 1976; Bernreuter *et al*., 1989; Electric Power Research Institute, 1986). First, the seismicity parameters (*a* and *b* values) of the transform fault system were obtained. The Quaternary faults with low seismicity rate were also included using their annual rate of displacement obtained from independent studies. These faults were assumed to present a constant moment rate. Next, the attenuation relations were estimated using a simple omega-squared model based on a general regression of the maximum acceleration recorded versus distance. These attenuation relations for this region were published in a previous work (Ortega and González, 2007). Finally, the hazard maps were computed to show probabilistic ground accelerations with 10%, 5%, and 2% probabilities of exceedance in 50, 100 and 200 years. The maps were constructed on the assumption that earthquake occurrence is Poissonian. Then the hazard curve was computed for three specific dams belonging to the National Commission of Water in Mexico and different fault system combinations comparing the results. The details on the hazard estimation are described in Frankel (1995), and Frankel *et al*., (1997). In the following sections, the steps to prepare the different parts of the probabilistic hazard analysis are describe.

## Seismicity and moment rate

Two different models were used to compute the seismic hazard: Gutenberg-Richter and Characteristic Models. The former was used to analyze the transform fault system of the Gulf of California and the latter was used for the Quaternary faults within the Baja California Peninsula. For the Gutenberg-Richter model, the catalog was compiled for 18 years of operation of La Paz Seismic Network (Munguía *et al*., 2006). 2127 earthquakes ranging from 1 to 6.1 degrees in magnitude, between 23° < Lat < 25° and -111° < Long < -108° were located. The catalog to remove the aftershocks of 1998 in Los Barriles, and 2007 Cerralvo earthquake was reviewed (Ortega and Quintanar, 2010). In Figure 1d the seismicity of the region from 1998 to 2013 is present.

The $a$ and $b$ values were computed using the EMR method described by Woessner and Wiemer (2005), and coded in the Z-Map suite of programs (Wiemer, 2001, Figure 2). The $b$ values were estimated using a maximum likelihood method (Bender, 1983).

The hazard calculation using the Gutenberg - Richter model involves the summation of the source contribution ranging from a minimum to a maximum expected earthquake magnitude. For each magnitude, a fault rupture length is calculated using the relationships of Wells and Coppersmith (1994). Next, a floating fault along the geological fault was set, and then the distance to the floating rupture for each site to calculate the frequency of exceedance (equation 2 from Frankel (1995) was found).

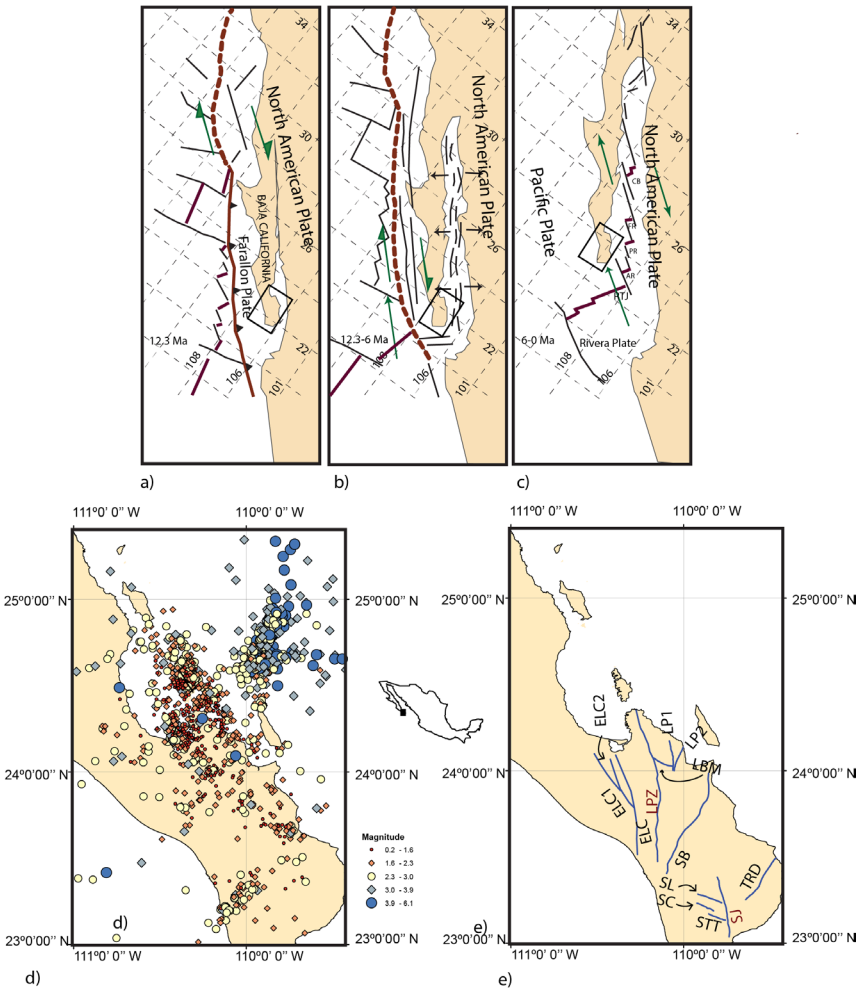


**Figure 1.** a) Farallon Plate that began the process of subduction starting the development of the Rivera Triple Junction. Between 20 and 12 Ma a series of microplates were formed along Baja California. b) Between 12 and 6 Ma normal faults with NNW and N trend, developed the east of the Tosco-Abreojos fault the system of normal faults was part of the distribution of the deformation, the gulf margin system was part of a complex system of transtensional faults. c) The regime of oblique divergence started about 6 Ma, when small rift basins began to form in the current Gulf of California. d) seismicity of the region, the complete catalog is represented. e) Quaternary Faults used in this article, La Paz and San José faults are used later to define different scenarios. AR, Alarcon Rise, PR, Pescadero Rise, FR Frallon Rise, CB Carmen Basin, RTJ, Rivera Triple Junction, and the faults: ELC, El Carrizal, ELC1, El Carrizal 1, ELC2, El Carrizal 2, LPZ, La Paz, LP1, San Juan de los Planes I, LP2, San Juan de los Planes II, LBM La Buena Mujer, SB, San Bartolo, TRD, La Trinidad, SL, San Lazaro, SC, San Carlos.

The estimation of the annual rate of earthquakes ($v_0$) for a characteristic fault was computed using the following relation (Wesnousky, 1986, Stirling and Gerstenberger, 2018):

$$v_0 = \mu \dot{u} LW / M_{0c} \qquad (1)$$

where $\mu$ is the shear modulus (30 GPa), $\dot{u}$ the annual slip rate of the fault, L and W are the fault length and width, respectively and $M_{0c}$ the characteristic moment obtained from the empirical scaling relation of Wells and Coppersmith (1994). The width of the fault $W$ was determined assuming a seismogenic depth of 20 km and projecting its dip, so that the width is equal to 20 km divided by the *sine* of the dip. The fault length is calculated from the total length of the digitized fault traces (Figure 1b). The slip rate was estimated using paleoseismic studies based on the overall vertical offset of the basins, and quantitative studies using trenches in specific areas (Maloney *et al*., 2007). Table 1 shows inland faults displacements and other parameters useful to estimate (1).

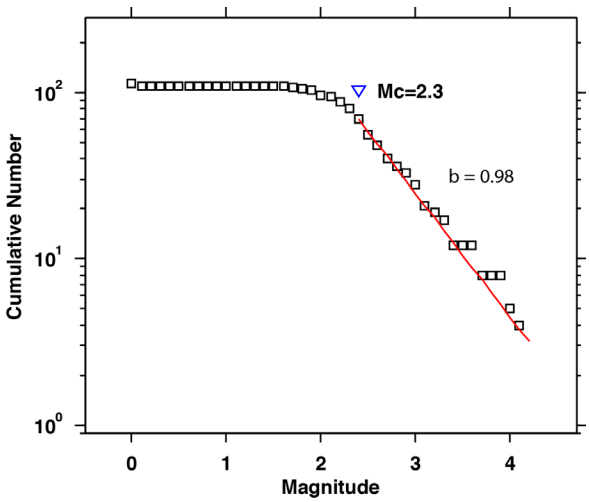


**Figure 2.** Plot of cumulative number of earthquakes versus earthquake magnitude, Mc =2.2 is the magnitude of completeness (b value is equal to 0.98).

The characteristic magnitude was determined from the length of the fault using the relationships of Wells and Coppersmith (1994), whose regression parameters depend on the tectonic environment. The characteristic moment was finally calculated from Kanamori (1977) equation once given the characteristic magnitude.

## Attenuation relations

The earthquake attenuation relations estimated in this area by Ortega and González (2007) were used. They observed that the attenuation in general is similar to that of southern California. The data were recorded using 32 strong-motion seismic stations from La Paz network

Table 1. Quaternary fault parameters used in this study.

| No. | Length (km) | Name | $M_{max}$ | Min. displacement (mm / year) | Max. displacement (mm / year) | Average displacement (mm / year) | Mo (dyne/cm) | Moment rate (dyne/cm*year) |
|---|---|---|---|---|---|---|---|---|
| 1 | 19.3 | San Juan de Los Planes I | 6.68 | 0.25 | 1 | 0.63 | 1.17E+26 | 7.24E+22 |
| 2 | 16.09 | San Juan de Los Planes II | 6.61 | 0.25 | 1 | 0.63 | 9.22E+25 | 6.03E+22 |
| 3 | 13.42 | La Buena Mujer | 6.54 | 0.25 | 1 | 0.63 | 7.27E+25 | 5.03E+22 |
| 4 | 39.47 | San José del Cabo | 6.95 | 0.5 | 1.5 | 1.00 | 2.97E+26 | 2.37E+23 |
| 5 | 15.22 | San Lázaro | 6.59 | 0.5 | 1.5 | 1.00 | 8.57E+25 | 9.13E+22 |
| 6 | 11 | Saltito | 6.47 | 0.7 | 0.8 | 0.75 | 5.61E+25 | 4.95E+22 |
| 7 | 11.35 | San Carlos | 6.48 | 0.25 | 1 | 0.63 | 5.84E+25 | 4.26E+22 |
| 8 | 71.4 | San Bartolo | 7.17 | 1 | 1 | 1.00 | 6.44E+26 | 4.28E+23 |
| 9 | 32.9 | Trinidad | 6.88 | 1 | 1 | 1.00 | 2.34E+26 | 1.97E+23 |
| 10 | 100 | La Paz | 7.30 | 0.11 | 1.6 | 0.86 | 1.00E+27 | 5.13E+23 |
| 11 | 65 | Carrizal | 7.14 | 0.11 | 1.6 | 0.86 | 5.70E+26 | 3.33E+23 |
| 12 | 34 | Carrizal1 | 6.89 | 0.11 | 1.6 | 0.86 | 2.45E+26 | 1.74E+23 |
| 13 | 37.5 | Carrizal2 | 6.93 | 0.11 | 1.6 | 0.86 | 2.78E+26 | 1.92E+23 |

(LAP) comprising 1320 small to moderate earthquakes (Figure 3). Some characteristics of the ground motion are:

a) attenuation functions for distances ranging between 40 and 100 km tend to slightly increase their amplitudes due to the critical reflections of the shear waves from the Moho. This feature is better observed at low frequencies (<5 Hz). These fluctuations are modeled in the parametric form of the geometrical spreading function, $g(r)$, which controls some changes in the seismic wave propagation.

b) values of the geometrical spreading control the general propagation effect due to distance between site and source. This propagation effect includes the source parameters, effects from finite faults that generate seismic waves at different depths, and the contribution of small and large earthquakes.

The predicted ground motion spectra at a frequency $f$ as a function of the hypocentral distance $r$ is given by:

$$logA_{ij}(r,f) = E_i(r_{obs},f)+SITE_j(f)+D(r,f) \quad (2)$$

where:

$$E_i(r_{obs},f)=log[S(f,M_w)+ +log[g(\frac{-\pi r_{obs}}{Q(f)\beta})exp(fr_{obs})] \overline{V}(f)e^{-\pi f\kappa eff} \quad (3)$$

and, $S(f, M_w)$ is the source Fourier velocity spectrum

$M_w$ is the moment magnitude

$g(r_{obs})$is the geometrical spreading function relative to $r_{obs}$ = 40 km

$Q(f)$ is the frequency-dependent quality factor

$\overline{V}(f)$ is a site amplification function

$\beta$ is the shear-wave propagation velocity

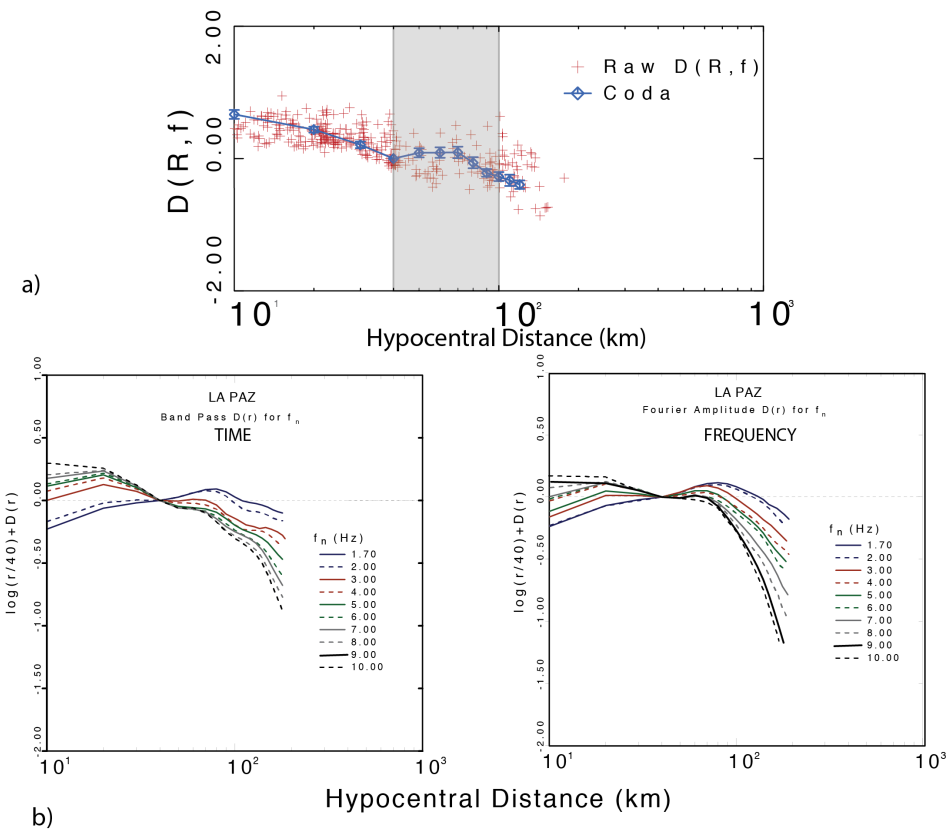


**Figure 3.** Attenuation relations estimated in the area. Top, example of the attenuation function from the regression, the gray area represents the distance between 40 and 100 km where the geometrical spreading exponent is low (0.2). Bottom, attenuation function for different frequencies using time (left) or frequency (right) analysis.

$\kappa_{eff}$ is a site attenuation coefficient

$r_{obs}$ is the observed distance from which we extrapolate to other distances

The second term is a level of motion that propagates the $S(f, M_w)$ term at $r_{obs}$. The source function $S(f)$ is a simple $\omega^2$ model as described by Brune (1970):

$$\mathrm{S}(f, Mo) = \frac{CM_0 2\pi f}{1+(f/[4.91\mathrm{x}10^6\,\beta\,(\Delta\sigma/M_0)^{1/3}])^2} \quad (4)$$

where: $C$ is equal to (0.55) (2) (0.707)/$4\pi\rho\beta^3$
the term $[4.91\mathrm{x}10^6\,\beta\,(\Delta\sigma/M_0)^{1/3}]$ is the corner frequency
$\Delta\sigma$ is the stress parameter in (bars)
$\beta$ is the average shear-wave crustalvelocity (3.5 km/sec.)
$M_0$ is the scalar seismic moment, which in turn is related to the moment magnitude (Kanamori, 1977).

$$M_w = \left(^{logMo}/_{1.5}\right) - 10.73. \quad (5)$$

Magnitude-distance tables were constructed using the SMSIM suite (Boore, 1983) and the ground motion parameters of Table 2.

Table 2. Ground-motion parameters

| | |
|---|---|
| $\kappa_{eff}$ | 0.06 |
| $\mathrm{Q}(f)$ | $180f^{0.32}$ |
| $\beta$ | 3.5 |
| $\rho$ | 2.8 |
| $\overline{\nabla}(f)$ | GEN97* |
| $\Delta\sigma$ | 40 |
| $\mathrm{g}(r)$ | $\begin{cases} r^{-1.0} & 0 \le r < 40 \\ r^{-0.2} & 40 \le r < 100 \\ r^{-0.5} & 100 \le r < 180 \end{cases}$ |

These attenuation relations are used in a look-up table procedure that was originally coded by (Frankel, 1995) in the USGS computer programs.

**Hazard estimation**

The hazard calculation was performed using the codes of USGS for the National Seismic Hazard Mapping Project (NSHMP) (Petersen, 2008). This code has the flexibility to be easily adapted and has been extensively reviewed during some decades (Frankel, 1995; Frankel *et al*., 1997). The attenuation relation's analysis were adapted using a look-up table. This code has the advantage that the data structure is virtually identical to the New Generation of Attenuation relations (NGA) that has been reviewed recently. So, any logical tree that would be adequate to this region can be created, including NGA attenuation relations. For simplicity, the attenuation relations of Table 2 were used. On the other hand, there are some advantages of using this computer code such as simple input of geological data and easy access to adjust the source code. This code has different modules including a smoothed grid source (Frankel, 1995) and floating fault sources. The program allows choosing between Gutenberg – Richter or the Characteristic models. During the last 20 years, thas been observed that there is not enough information to compute robust $a$ and $b$ values for Quaternary faults. However, for transform fault systems, the Gutenberg – Richter model is adequate. Most of the seismicity occurred in main - aftershock earthquake sequences, and once the aftershock removal is performed, the seismicity parameters can be obtained. The hazard calculation was performed using the Characteristic model for the Quaternary faults and the Gutenberg – Richter for the transform fault system.

**Fault contributions**

There are two types of sources. Active faults and Quaternary Faults both sources are fault areas; there is much work in defining the correct source. For the Quaternary faults, which is the focus of this article, in a map view, a fault is a line because it is expressed as a strike and dip. Not a smoothed grid area source was used because the transform system is well defined and there is no sparse seismicity in the surrounding region. The active faults were modeled using the Anderson (1979) model. The seismogenic thickness is constrained to 20 km; the fault dip is based on geophysical models (Arzate, 1986). Since the present model is based on the Characteristic fault rupture, then completeness magnitude and statistical values of a and b are not used. However, in the active tectonics, the maximum magnitude and magnitude range play an essential role.

In the study area, faults that control the hazard are not well identified and different authors disagree on whether some faults should be considered as potentially dangerous in hazard estimation. The purpose of this work is to test whether there are significant

differences if some Quaternary fault segments are included or discarded in the seismic hazard analysis. First, the seismic hazard was computed using all the source information that is available from the national geological maps of the Mexican Geological Survey (SGM), using the 1: 10,000 and 1: 250,000 maps (SGM, 1996, 1999, 2000, 2001, 2002, 2008). Second, two different scenarios were computed: scenario (a), the seismic hazard without La Paz fault (WLP), and scenario (b) seismic hazard without San Jose fault (WSJ). Finally, the PGA for 3 sites was computed. In Figure 4, the results of the probabilistic seismic hazard analysis for all the faults are shown. It is noticeable that the Transform Fault System of the Gulf of California controls the seismic hazard for short return periods. This are to the use of the Characteristic Model for inland faults with a return period greater than 1000 years, and these characteristic faults do not contribute to the hazard estimation for short return periods. On the other hand, in the case of long return periods the characteristic faults control the hazard.

In Figure 4, the lower panels represent the 2% of exceedance of 50, 100 and 200 years that correspond to return periods of 2479, 4950 and 9900 years, respectively. These return periods are usually used for the engineering design of essential facilities such as bridges and dams.

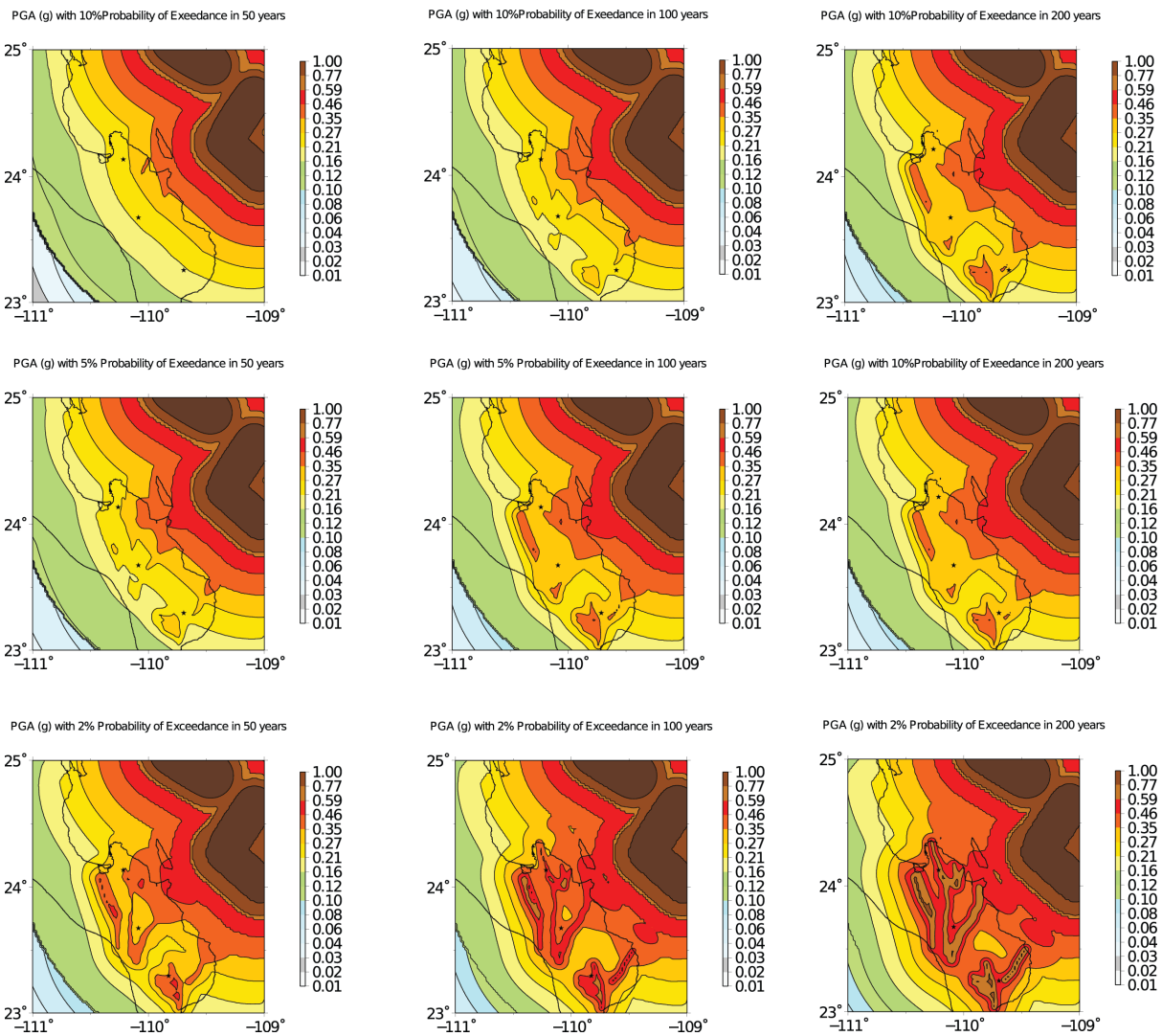


**Figure 4.** Probabilistic seismic hazard analysis for different return periods and observation times using all the sources. The transform fault system is located at the top right of the map and analyzed with the Gutenberg-Richter model. The Quaternary faults are located within the Baja California Peninsula and analyzed with the Characteristic model, the stars represent the site of the dams, the northern dam is La Buena Mujer, in the middle Santa Ines and at the southern side La Palma (see text for details).

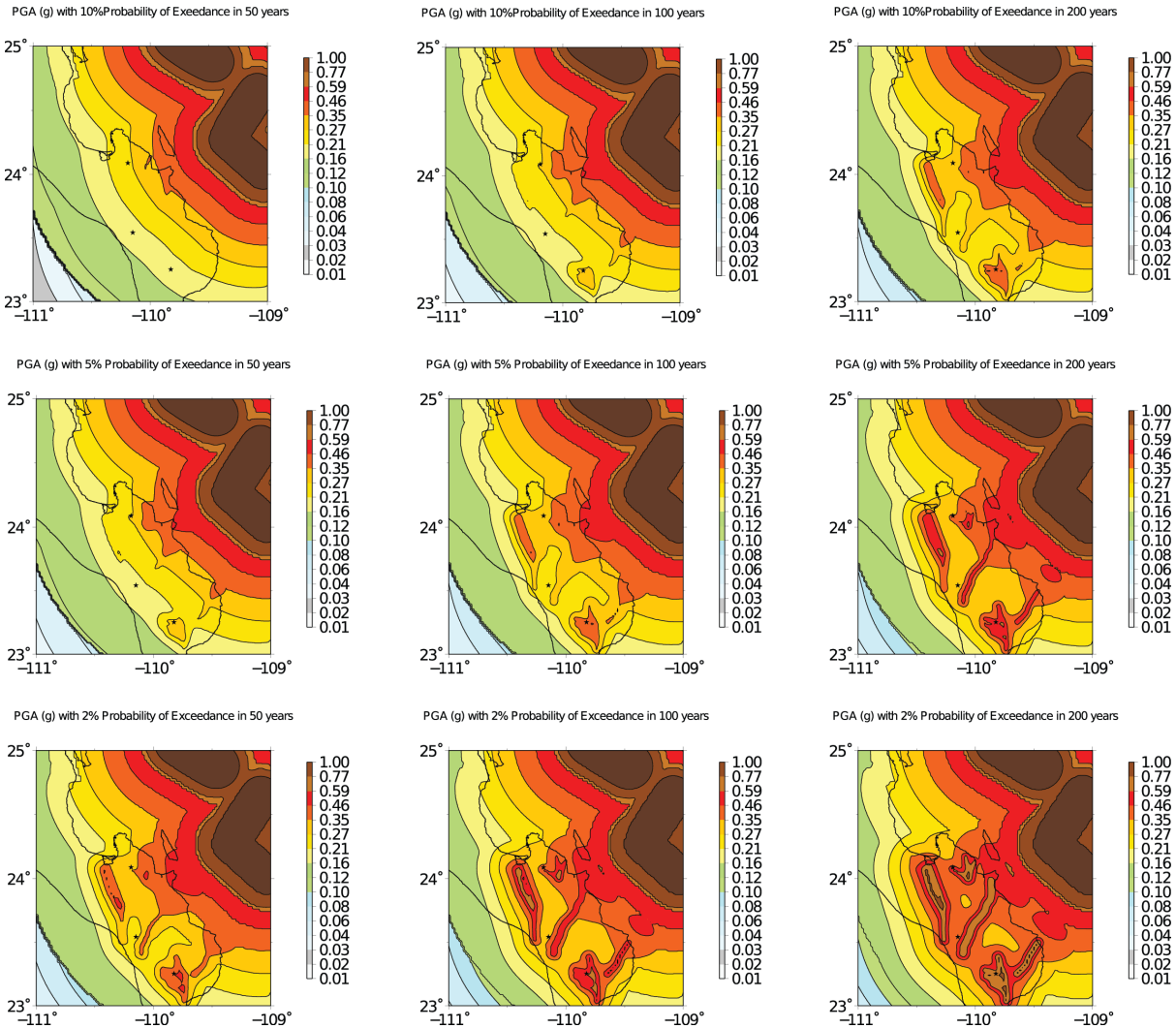


**Figure 5.** Probabilistic seismic hazard analysis for different exceedance probabilities and observation periods using the WLP model. The transform fault system is located at the top right of the map and analyzed with the Gutenberg-Richter model. The Quaternary faults are located within the Baja California Peninsula and analyzed with the Characteristic model (see text for details).

In the last panel of Figure 4, the location of the three principal dams (stars) match with the region of the high seismic hazard.

In Figure 5 the seismic hazard using the WLP model is shown and for short return periods (panels 1,2,4) the maps are virtually identical. However, for long return periods there are substantial differences among the principal dams, especially for the Buena Mujer and Santa Ines dams, identified at the northern side of the region (panels 6,7,8 and 9). In contrast, La Palma dam is too far from La Paz fault and the hazard contribution is negligible.

Similarly, in Figure 6, the hazard using the WSJ model was calculated. The San José fault affects La Palma dam and is not contributing to the hazard of Buena Mujer and Santa Ines dams. In this case, the presence of smaller faults (Saltito, San Lazaro, Trinidad) are of special importance since they are located close to La Palma dam and the absence of the San José fault in the hazard calculation is not so sensitive as is the case of the WLP model.

Figure 7 shows a comparison among models for PGA values of hazard calculation for different return periods and the three different fault scenarios. In the absence of these faults, the PGA is reduced for the long return period.

In Figure 8, the hazard curve of the complete model for La Palma, Santa Ines and

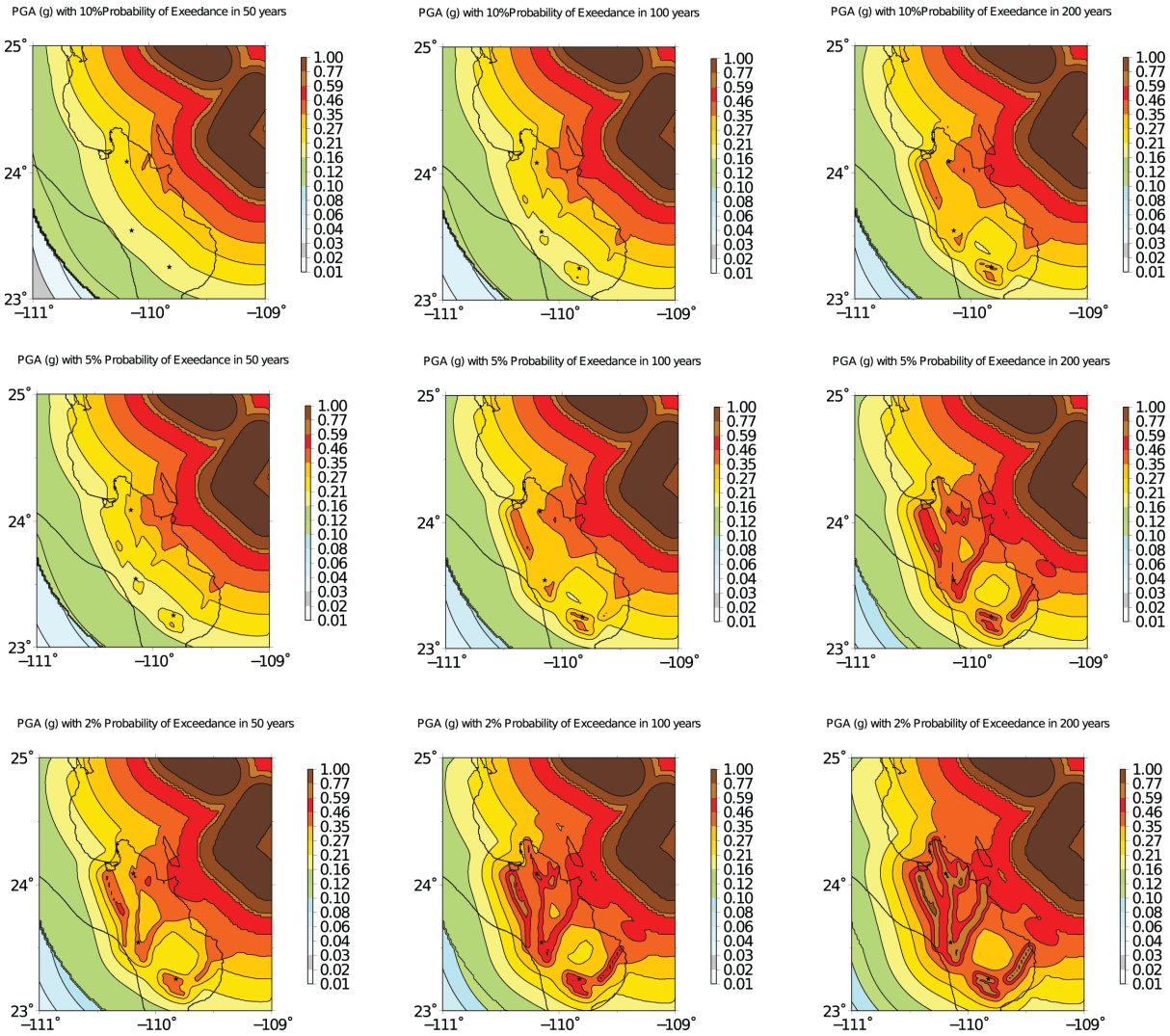


**Figure 6.** Probabilistic seismic hazard analysis for different return periods and observation times using the WSJ model. The transform fault system is located at the top right of the map and it was analyzed with the Gutenberg-Richter model. The Quaternary faults are located within the Baja California Peninsula and analyzed with the Characteristic model (see text for details).

Buena Mujer dams is depicted. In the hazard curve, the Characteristic Fault Model was used excluding the transform faults of the Gulf of California. The three curves are similar; the Buena Mujer and Santa Ines curves are parallel because their hazard is controlled mainly by La Paz fault, and the rest of the faults are not important.

In Figure 9, the hazard curves of the three dams using the WLP model are shown. In this case, the three curves are different and we observe that the Santa Ines dam has lower PGA values. The Santa Ines dam is relatively far from the other faults, except for La Paz fault that is the closest to the dam.

In Figure 10, the WSJ model is depicted. Interestingly, the WSJ and the complete model of Figure 8 are similar, suggesting that for these sites the contribution of the San José fault is not so important.

In general, the hazard estimation has been used in Mexico with $a$ and $b$ values statistical coefficients of seismicity. Little importance has been given to faults that exhibit large return periods and pose risks in the long term. A recent example reported by a study of seismic hazard in central Mexico used instrumental seismicity as well as historical data includeding fault information (Beyona *et al*., 2017). However, this is the first time that a similar study is performed in Baja California

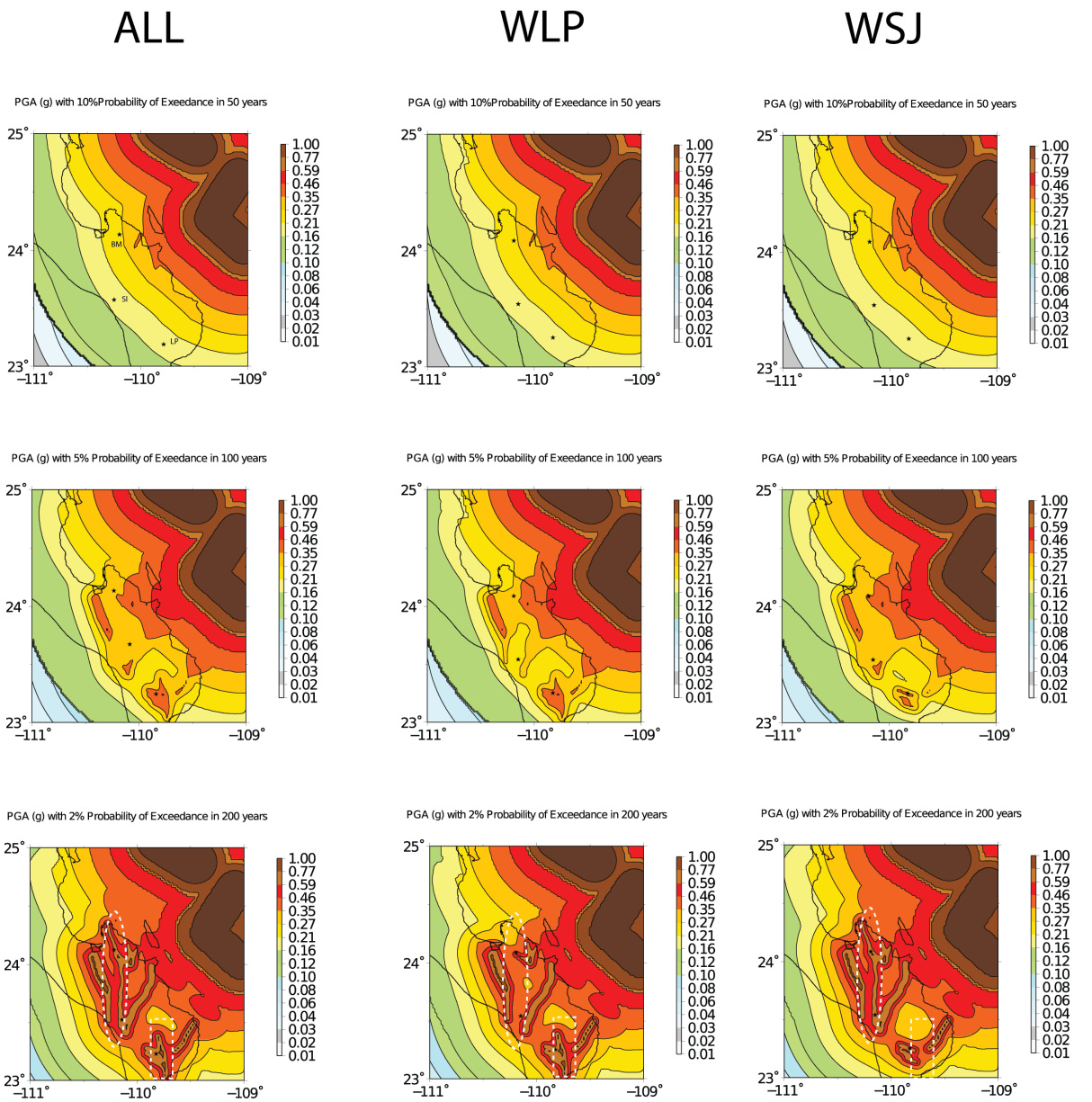


**Figure 7.** Contour plot for PGA values of hazard calculation for different return periods and three different fault scenarios. Left column, model with all faults; central column, model without La Paz fault; right column, model without San José fault. The cases are 10% of probability of exceedance in 50 years (first row, from top to bottom); 5% of probability of exceedance in 100 years (second row); 2% of probability of exceedance in 200 years (third row). The last row shows the long return period expressed as 2% probability of exceedance in 200 years. The elliptical region covers La Paz fault and the squared region San Jose fault. BM Buena Mujer Dam, SI Santa Ines Dam and LP La Palma Dam.

Sur. There are some reasons why long return periods have not been traditionally considered in the seismic hazard estimation in Mexico, such as: a) the high active tectonics in the coast which is usually more important than inland active faults and b) there are insufficient paleoseismic studies in the region. However, in Baja California Sur, the active sources with high annual moment rate occur in the Gulf of California, and Quaternary faults are located in the peninsula. Moreover, this region was originally populated in areas close to principal faults, because these faults are the principal sources of water that is collected from the mountain ranges situated at the center of the Peninsula. Also, these faults are the cause of the high mineralization of gold, copper and silver, giving rise to important mining development. Therefore, there is a high correlation between fault location and population.

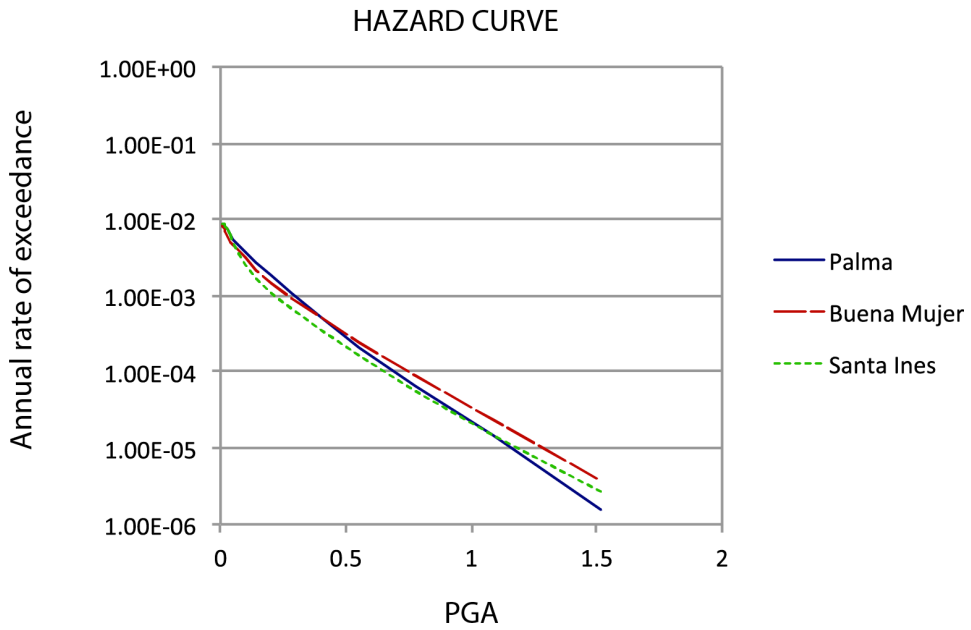


**Figure 8.** Hazard curve for the complete model for La Palma, Santa Ines and Buena Mujer dams using the Characteristic models of the Quaternary faults.

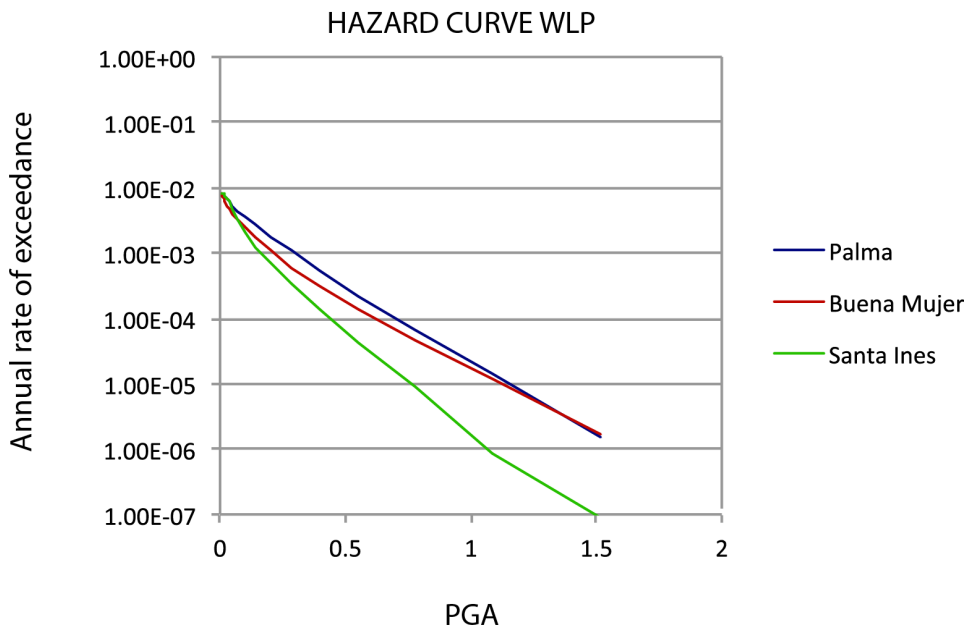


**Figure 9.** Hazard curve of the WLP for La Palma, Santa Ines and Buena Mujer dams using the Characteristic models of the Quaternary faults.

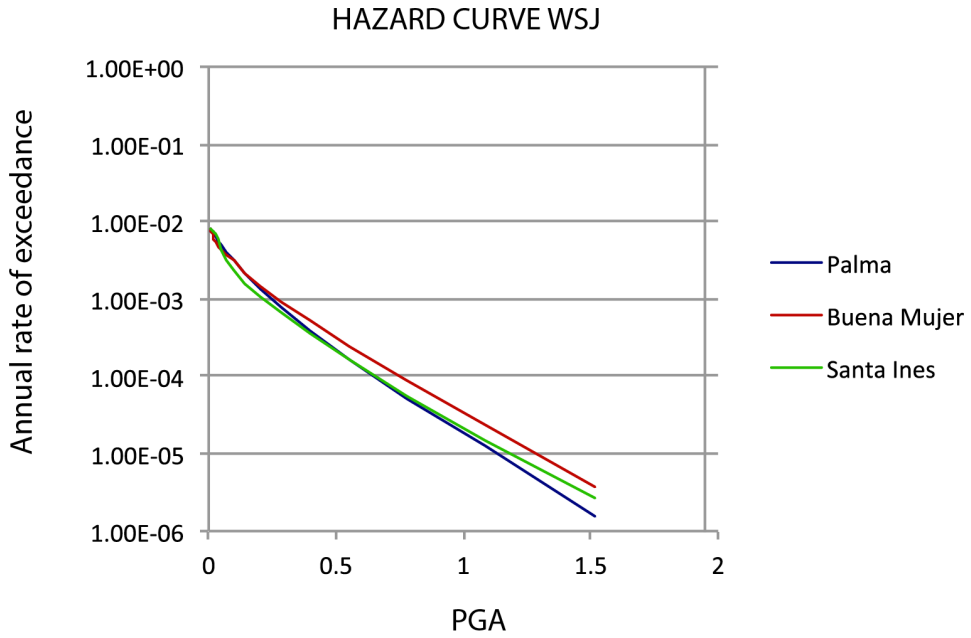


**Figure 10.** Hazard curve of the WSJ for La Palma, Santa Ines and Buena Mujer dams using the Characteristic models of the Quaternary faults.

Another contribution of this study is the usage of attenuation relations obtained for this region. A simple look-up table of magnitude-distance based was introduced on the work of Ortega and González, (2007). However, the results do not differ considerably when the attenuation relations of Southern California are used instead, since they are characterized by similar values of $Q(f)$, geometrical spreading function and kappa (Ortega and Gonzalez, 2007). Moreover, the NGA attenuation relations are also a good approximation. In this work, rather than analyzing the sensitivity of the predictive relationships, the differences in considering or ignoring some faults are studied.

## Discussions

Including or excluding faults in PSHA implies great differences in the results. This is not surprising in PSHA because this problem has been observed over decades in different regions, however, there are some interesting aspects of this region that we will discuss. First, the PSHA is based on a formal probabilistic framework that considers all the uncertainties, including the epistemic ones. For this reason, PSHA is based on logic trees that mimics the probability distribution of the seismic sources epistemic errors. To design the logic tree, decisions are always made through panels of experts. Marzochi and Jordan (2017) discussed a global framework to analyze the PSHA, in their article they noted the importance of the participation of experts, but it is important to say that there is a subjective part that implies adding preferential information, which not always seem to have a scientific basis. It is important to emphasize that adding subjective preferences is not necessarily non-scientific knowledge, the most important thing is to be able to prove if our preferences make sense or if they should be discarded in the future.

A problem that frequently occurs in the PSHA by participating in a committee of experts that is specifically focused to seismic hazard, is that experts tend to strategically manipulate their opinion. For example, in the case of giving advice on the existence of a fault to develop hazard maps, an expert knows that in case of an error there is a risk of a major disaster, but in the case of developing maps of natural resources those errors are not so relevant and probably their opinion will be different. In addition, an expert may be pro- environment and inadvertently he would include more restrictions if the panel of experts take decissions for nuclear power plants for example. After analyzing the best option for PSHA the logic tree of Figure 11 was prefered. This model exemplifies the epistemic uncertainty of sources, magnitude and attenuation relations (GMPE, Ground motion prediction equations).

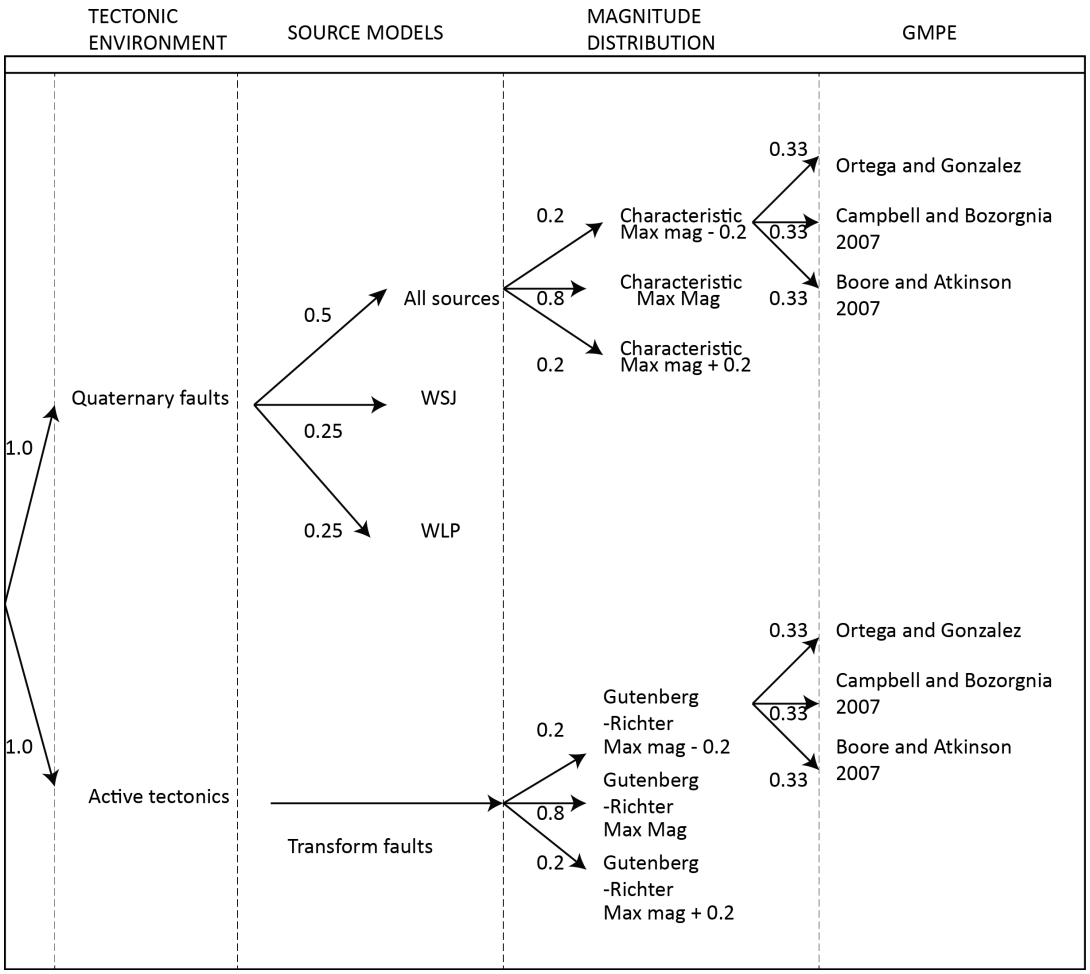


**Figure 11.** Logic tree for PSHA of Baja California Sur.

The logic tree of Figure 11 is based on analyzing advantages and disadvantages of the different models. In this model, the most important decision was the Quaternary faults weights of three different models (all faults, WSJ and WLP).

In Figure 12 the final map for two return periods is presented, the first panel represents 2% of exceedance in 50 years, the second represents 2% of exceedance in 200 years, therefore the first is equivalent to a return period of 2475 years and de second of 9900 years. In this interval, there is a major difference in the hazard maps. However, the 2475 return period is sometimes considered as the highest threshold for essential facilities. Comparing the 2475 return period (Figure 12 first panel) with the 474 years (Figure 4 first panel) we observe that the Quaternary faults apparently are not sensitive for high rates. However, this is only a mere artifact of the arbitrary decision of using return periods as a degree of protection because at higher return periods the hazard should be nuanced. Recently Stirling and Gerstengerg (2018), studied the applicability of a Gutenberg-Richter magnitude distribution instead of the Characteristic fault model. In their study Stirling and Gerstengerg (2018) analyzed active faults with high slip rates (> 1 mm/yr), their results suggest that the Gutenberg Richter magnitude distribution is compatible with active faults and cannot be ruled out in PSHA, but for low slip rates ( < 1 mm/yr), this possibility has not been tested yet. Our study opens a possibility to improve the PSHA in Baja California to include the Gutenberg-Richter magnitude distribution in the future. Similar studies have been reported in central Mexico (Bayona *et al*., 2017). Work is in progress to present a combination of Gutenberg-Richter and Characteristic magnitude distribution. Care should be taken if we compare our results with other studies, for example, it is common to represent a PGA concerning a specific rock

site namely Vs30=760, this reference is based on geotechnical studies in which there is a competent rock at 30m depth with a value of 760 m/s for shear wave velocity. We used a general average value that represents the common amplification of the basins in BCS. Also, we used a low attenuation model. It is important to note that we do not have the intention to use our results for engineering purposes until we can validate them.

This article reflects the importance of studying active Quaternary faults at a regional scale. Paleoseismic studies provide valuable information about slip rates. It is crucial to use this information in the seismic hazard analysis and include the results in a specific way that can be useful in hazard maps. For example, Busch *et al*. studied the Carrizal Fault (Figure 1) they prepared trenches and presented their results in a self-consistent tectonic framework. Their studies discussed a tectonic relation of the transtensional regime in Baja California. We obtained the slip rate from their analysis, but in other cases, the slip rate is not estimated. For example in the La Paz fault. In that case, we only estimated a possible slip rate based on limited work about the fault.

Nowadays, paleoseismology studies are becoming a new discipline; they also provide information that the instrumental seismicity is not capable of obtaining. The active crustal faults sometimes are not included in PSHA because it seems that they are not as dangerous if compared to active tectonics (e.g., subduction margins), but we believe that this impression is incorrect. The Major-Cucapah earthquake in 2010 (Mw = 7.2) that occurred in Mexicali, Baja California is an excellent example of a crustal fault that caused severe damages. The geological and geophysical geometry is essential to consider in mapping the damages (Wei *et al*., 2011), the recurrence is about 2,000 years (Rockwell *et al*., 2010) so, if we compare to the active tectonics of few tens of years, it probably should be not so critical. However, the problem is the location of these faults. In the Baja Peninsula, the faults are located close to the urban centers.

Another problem to address is the lack of studies and instrumentation. For example, Suter (2018) reported the Loreto earthquake of 1878; this event seems to be the worst scenario for Baja California Sur, the destruction was very severe. Up to date, there are no studies that identify the actual fault. Note that in this region, there are seismic records with extreme levels of PGA, in 2007 a strong motion instrument recorded an earthquake with a maximum value of 0.6 g in Bahia Asuncion (Munguia *et al*., 2010; Ortega *et al*., 2017). The value of 0.6 g exceeds by far any expected value in previous hazard maps in the region, reflecting the need to study the Quaternary Faults and the effect in the seismic hazard.

We conclude that the Quaternary faults are only important when computing the hazard using high recurrence rates. In places where the active tectonic sources, such as faults belonging to the transform fault system, are far from the sites, as is the case of Baja California Sur, the contribution of the hazard of such Quaternary faults is not so evident. Specially for low recurrence rates. Clearly, a detailed paleoseismic study is of crucial importance to assess the hazard for this region. The complete model with all the sources is the best for earthquake-resistance structures, especially for dams' design. On the other hand, overestimating the hazard may have the consequence of introducing unnecessary severe construction codes causing an economic impact on the development of this region due to the increase in construction costs. In Mexico, there is no specific guidance for choosing return periods on dams' designs. However, the general trend of 2% of exceedance in 50 years may be not adequate and 2% of exceedance in 200 years seems to be adequate in Baja California Sur. This level of security has a large impact in the economic development and is very important for strategic planning.

## Conclusions

The general conclusions are:

1) The southern part of Baja California is a region with important faults that control the seismic hazard of the high return periods.

2) Active Quaternary faults need to be studied, especially the average displacement or moment rates.

3) Specifically, in Baja California Sur, the return period for critical facilities should be 9900 years expressed as the 2% probability of exceedance in 200 years.

## Acknowledgments

This work is the effort of many years of seismic studies; we are in debt with the technical staff of CICESE Ensenada who initiated most of the field work in Baja California Sur. Alfredo Aguirre and Sergio Mayer are acknowledged for maintaining the seismic stations of Baja California Sur during the past 18 years. We

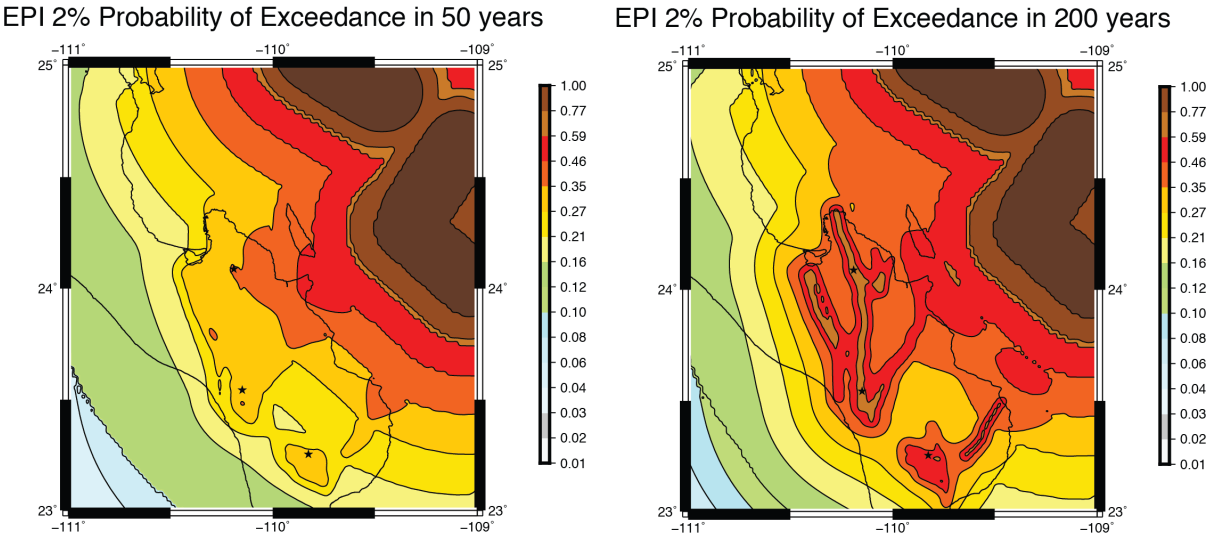


**Figure 12.** Hazard map of the final model using a logic tree for Baja California Sur for two different return periods. The 2% probability of exceedance in 50 years is a standard for dam designs. In contrast a 2% probability of exceedance in 200 years is plotted for comparison.

acknowledge three anonymous reviewers that helped to improve the quality of this article. This work was partly supported by a CONACYT grant number 133910, CICESE internal projects 691114, 691115, and Cátedras Conacyt projects 97 and 2284.

## References

Algermissen, S.T., and D.M. Perkins ,1976, A probabilistic estimate of máximum acceleration in rock in the contiguous United States, *US Geological Survey Open – File Report* 76 – 416, 45 pp., 3 plates.

Algermissen, S.T., Perkins, D.M., Thenhaus, P.C., Hanson, S.L., and Bender, B.L., 1990, Probabilistic earthquake acceleration and velocity maps for the United States and Puerto Rico, *US Geological Survey Map MF – 2120*, 2 sheets, 4 plates.

Anderson, J.G.,1979, Estimating the seismicity from geological structures for seismic risk studies, *Bull. Seism. Soc. Am*. 69 135 -158.

Angelier, J., B. Colletta, J. Chorowicz, L. Ortlieb, and C. Rangin, 1981, Fault tectonics of the Baja California peninsula and the opening of the Sea of Cortez, Mexico, *Journal of Structural Geology* 3, no. 4, 347–357, doi:10.1016/0191-8141(81)90035-3.

Arzate, J. 1986. Geophysical Reconnaissance for Geohydrological Evaluation in the La Paz-El Carrizal Valley, Baja California Sur, Mexico. M.S. Thesis. International Institute for Aerosurvey and Earth Sciences (ITC), Delft, Holanda.

Atwater, T.,1970, Implications of plate tectonics for the Cenozoic tectonic evolution of western North America, *Geol. Soc. Am. Bull*. 81 3513– 3536, doi:10.1130/0016-7606(1970)81[3513: IOPTFT]2.0 .CO;2.

Bayona Viveros J. A., G. Suarez G. and M. Ordaz, 2017, A probabilistic seismic hazard assesment of the Trans-Mexican volcanic belt, Mexico, based on historical and instrumentally recorded seismicity, Geofisica Internacional, 56, 1, 87-101.

Bender, B., 1983, Maximum likelihood estimation of b values for magnitude grouped data, *Bull. Seism. Soc. Am*. 73, no. 3, 831 -851.

Bernreuter, D.L., J.B. Savy, R.W. Mensing, and J.C. Chen, 1989, Seismic hazard characterization of 69 nuclear power plant sites east of the Rocky Mountains, *U.S Nuclear Regulation Commission, NUREG/CR – 5250, UCID 21517,* Lawrence Livermore National Lab.

Boore, D. M., 1983, Stochastic simulation of high-frequency ground motions based on seismological models of the radiated spectra, *Bull. Seism. Soc. Am.* 73, no.6 1865-1894.

Brune, J. N., 1970, Tectonic stress and the spectra of seismic shear waves from earthquakes*, J. Geophys. Res*. 75, 4997–5009, doi:10.1029/JB075i026p04997.

Busby, C. J. and R.V. Ingersoll, 1995, *Tectonics of sedimentary basins*, Blackwell Science, Cambridge, MA, 579 pp.

Busch, M.M., J.R. Arrowsmith, P.J. Umhoefer, G. Martínez- Gutiérrez, N.A. Toké, D. Brothers, E.N. DiMaggio, S.J. Maloney, O. Zielke, and B. Buchanan (2006). Late Quaternary faulting in the Cabo San Lucas–La Paz region, Baja California, *Eos (Transactions, American Geophysical Union).* 87, no. 52, fall meeting supplement, [abs] T41D-1612.

Busch, M.M., J.A. Coyan, J.R. Arrowsmith, S.J. Maloney, G. Martínez-Gutiérrez, and P.J. Umhoefer, 2007, Late Quaternary faulting along the San Juan de Los Planes fault zone, Baja California Sur, Mexico, *Eos (Transactions, American Geophysical Union).* 88, no. 52, [abs] T41A-0357.

Cornell, C.A., 1968, Engineering seismic risk analysis, *Bull. Seism. Soc. Am*. 58, 1583 – 1606.

Cruz Falcón A., R. Vázquez González, J. Ramírez Hernández, F. Salinas González, E. Nava Sánchez and E. Troyo Diéguez, 2010, Depth estimation to cristalline basement in the valley of La Paz, Baja California Sur, Mexico*, Geofísica Internacional*, 49, 213-224.

DeMets, C., 1995, A reappraisal of seafloor spreading lineations in the Gulf of California: Implications for the transfer of Baja California to the Pacific plate and estimates of Pacific–North America motion, *Geophys. Res. Lett.* 22, no. 24, 3545–3548, doi:10.1029/95GL03323.

Electric Power Research Institute, 1986, Seismic hazard methodology for the Central and Eastern United States, *Technical Report*, vol. 1 -3.

Fletcher, J. and L. Munguía, 2000, Active continental rifting in southern Baja California, Mexico: Implications for plate motion partitioning and the transition to seafloor spreading in the Gulf of California, *Tectonics*, 19, 1107-1123.

Fletcher, J.M., M. Grove, D. Kimbrough, O. Lovera, and G.E. Gehrels, 2007, Ridge-trench interactions and the Neogene tectonic evolution of the Magdalena shelf and southern Gulf of California: Insights from detrital zircon U-Pb ages from the Magdalena fan and adjacent areas, *Geol. Soc. of Am. Bull.*, 119, 1313–1336, doi:10.1130/ B26067.1.

Frankel, A., 1995, Mapping seismic hazard in the central and Eastern United States, *Seism. Res. Lett*., 66, no. 4, 8 -21.

Frankel, A., C. Muller, T. Barnhard, D. Perkins, E. Leyendecker, N. Dickman, S. Hanson, and M. Hooper, M, 1997, Seismic hazard maps for the conterminous United States, *U.S. Geological Survey Open File Report* 97 – 131, 12 maps.

Gorbatov, A. and Y. Fukao, 2005,. Tomographic search for missing link between the ancient Farallon subduction and the present Cocos subduction, *Geophy. J. Int.* 160, Issue 3, 849–854, https://doi.org/10.1111/j.1365-246X.2005.02507.x.

Hausback, B.P., 1984, Cenozoic Volcanic and Tectonic Evolution of Baja California Sur, Mexico, *Ph.D. thesis*, Berkeley, University of California, 72 pp.

Kanamori, H., 1977, The energy release in great earthquakes, J. Geophys. Res. 82, (20), 2981–2987, doi:10.1029/JB082i020p02981.

Lizarralde, D., G.J. Axen, H.E. Brown, J.M. Fletcher, A. González-Fernández, A.J. Harding, W.S. Holbrook, G.M. Kent, P. Paramo, F. Sutherland, and P.J. Umhoefer , 2007, Variation in styles of rifting in the Gulf of California, *Nature*, 448, 466–469, doi:10.1038/ nature06035.

Maloney, S.J., P.J. Umhoefer, J.R. Arrowsmith, G. Martinez- Gutiérrez, A.U. Santillanez, and Rittenour, 2007, Late Pleistocene–Holocene faulting history along the northern El Carrizal fault, Baja California Sur, Mexico, Earthquake recurrence at a persistently active rifted margin Eos *(Transactions, American Geophysical Union)*, 88, no. 52, abs, T41A-0357.

Marzocchi, W., and Jordan, T. H. ,2017, A Unified Probabilistic Framework for Seismic Hazard Analysis. *Bull. Seism. Soc. Am*, 107, 2738-2744. doi: 10.1785/0120170008.

Mayer, L., and K.R. Vincent, 1999, Active tectonics of the Loreto area, Baja California Sur, Mexico, *Geomorphology*, 27, 243–255, doi:10.1016/S0169 -555X (98)00074-9.

Munguía, L.M., M. González, S. Mayer, and A. Aguirre, 2006, Seismicity and state of stress in the La Paz– Los Cabos region, Baja California Sur, Mexico, *Bull. Seism. Soc. Am.* 96, 624–636, doi:10.1785/0120050114.

Ortega, R. and M. Gonzalez, 2007, Seismic-wave attenuation and source excitation in La Paz-Los Cabos, Baja California Sur, Mexico, *Bull. Seism. Soc. Am*. 97, 545-556 doi:10.1785/0120060083.

Ortega, R. and L. Quintanar, 2010, Seismic evidence of a ridge-parallel strike-slip fault off the transform system in the Gulf of California, *Geoph. Res. Lett*., vol. 37, 6, doi: 10.1029/2009GL042208.

Oskin, M., J.M. Stock, and A. Martín-Barajas, 2001, Rapid localization of Pacific–North America plate motion in the Gulf of California, *Geology,* 29, 459–462, doi: 10.1130/0091-7613(2001)029<0459: RLOPNA>2.0.CO;2.

Petersen, M.D., 2008, United States National Seismic Hazard Maps: U.S. Geological Survey Fact Sheet 2008–3017, 4 pp.

Plattner, C., R. Malservisi, T.H. Dixon, P. LaFemina, G.F. Sella, J. Fletcher, and F. Suarez-Vidal, 2007, New constraints on relative motion between the Pacific plate and Baja California microplate (Mexico) from GPS measurements, *Geophy. J. Int.*, 170, no. 3, 1373–1380, doi:10.1111/j.1365-246X.2007.03494.x.

Ramos E., 1998, Características de la deformación en las rocas cristalinas cretásicas de la región E-SE de la ciudad de la Paz, BCS, México, *MS thesis*, CICESE, México (in spanish).

Servicio Geológico Mexicano, 1996, Geologic map, San Antonio, F12-B14, Baja California Sur, México, scale 1: 50,000.

SGM, 1999. Servicio Geológico Mexicano, Geologic map, La Paz, G12-10-11, Baja California Sur, México, scale 1: 250,000.

SGM, 2000. Servicio Geológico Mexicano, Geologic map, San Juan de Los Planes, F12-B14, Baja California Sur, Mexico, scale 1: 50,000.

SGM, 2001. Servicio Geológico Mexicano, Geologic map, Todos Santos, F12-B33, Baja California Sur, México, scale 1: 50,000.

SGM, 2002. Servicio Geológico Mexicano, Carta geológica – minera San Jose del Cabo, F12-2-3-5-6, Baja California Sur, Mexico, scale 1: 250,000.

SGM, 2008. Servicio Geologico Mexicano, Geologic map, La Paz, Baja California Sur, México, scale 1: 50,000.

Stirling M., and M. Gerstenberg, 2018, Applicability of the Gutenberg-Richter relation for major active faults in New Zealand, Bull. Seism. Soc. Am., 108, no. 2, 718-728, doi: 10.1785/0120160257.

Stock, J.M., and K.V. Hodges, 1989, Pre-Pliocene extension around the Gulf of California and the transfer of Baja California to the Pacific plate, *Tectonics*, 8, no. 1, 99–115, doi:10.1029/TC008i001p00099.

Suter, M., 2018, The historical seismicity of the Loreto region, Baja California peninsula, Mexico (1684-1778), *Seism. Res. Lett*, 89, 1, 202-209.

Umhoefer, P.J., L. Mayer, and R.J. Dorsey, 2002, Evolution of the margin of the Gulf of California near Loreto, Baja California peninsula, Mexico, *Geol. Soc. of Am. Bull.* 114, 849–868, doi:10.1130/0016-7606(2002)114<0849: EOTMOT>2.0.CO;2.

Umhoefer, P.J., F. Sutherland, G. Kent, A. Harding, D. Lizarralde, T. Schwennicke, J. Fletcher, W.S. Holbrook, and G. Axen, 2008, Synchronous changes in rift- margin basins and initiation of the Alarcón spreading ridge and related transform fault, southwestern Gulf of California*, Geol. Soc. Am. Abstracts with Programs*, 40, no. 6, 151p.

Wei, S., E. Fielding, S. Leprince, A. Sladen, J.P. Avouac, D. Helmberger , E. Hauksson, R. Chu, M. Simons, K. Hudnut, T. Herring and R. Briggs (2011), Superficial simplicity of the 2010 El Mayor-Cucapah earthquake of Baja California in Mexico. *Nature Geoscience*. doi:10.1038/ngeo1213, 2011.

Wells, D.L. and K.J. Coppersmith, 1994, New empirical relationships among magnitude, rupture length, rupture witdh, rupture área and surface displacement, *Bull. Seism. Soc. Am*. 8, no. 4, 974 -1009.

Wesnousky, S., 1986, Earthquakes, quaternary faults, and seismic hazard in California, *J. of Geophy. Res*. 91: doi:10.1029/0JGREA000091000B12012587000001.

Woessneser J. and S. Wiemer, 2005, Assessing the quality of earthquake catalogs: Estimating the magnitude of completeness and its uncertainty, *Bull. Seim. Soc. Am.* 95, 684-698.

Wiemer S., 2001, A software package to analyze seismicity: ZMAP, Seism.Res. Lett. 72, 373-382.

Geofísica Internacional (2019) 58-2: 169-178

Original paper

# Coseismic displacements and Mw estimation of the El Mayor-Cucapah earthquake, Mexico, from GPS source spectra

J. Carlos Robles-Avalos, J. Alejandro González-Ortega*, J. Javier González-García and J. Antonio Vidal-Villegas

Received: August 10, 2018; accepted: November 20, 2018; published on line: April 01, 2019
DOI: http://dx.doi.org/10.22201/igeof.00167169p.2018.58.2.1968

**Resumen**

El sismo de magnitud Mw 7.2 El Mayor-Cucapah ocurrió el 4 de abril de 2010 en el Valle de Mexicali, cerca de la frontera entre California USA y Baja California, México. El objetivo del presente trabajo fué examinar el GPS como una herramienta complementaria en estudios sísmicos y estimar el momento sísmico del sismo y su magnitud Mw. Para ello se exploró la capacidad de los datos de GPS de alta frecuencia (5Hz) localizados en el norte de la ruptura sísmica para obtener la cinemática de los desplazamientos cosísmicos. Los datos GPS se procesaron utilizando el método de Posicionamiento Puntual Preciso con el software GIPSY-OASIS II, posteriormente se aplicó la Transformada Rápida de Fourier a las series de tiempo de posición, se calcularon los parámetros espectrales, momento sísmico y Mw. Se encontró una buena concordancia en términos de correlación de la señal de los desplazamientos GPS comparando los registros sísmicos de movimientos fuertes integrados al desplazamiento, utilizando parámetros de filtrado para dos conjuntos de instrumentos. Los espectros de desplazamiento cinemático GPS muestran un nivel de desplazamiento espectral de baja frecuencia (~0.2 Hz) cuando se compara con la doble integración de los datos de movimientos fuertes. Es fácil calcular el movimiento cosísmico estático a partir de los datos GPS. Sin embargo es muy difícil calcularlos a partir de los datos de movimientos fuertes. Un modelo simple de fuente sísmica es adecuado para el conjunto de datos GPS utilizados en este trabajo, se estimó Mw=7.19±0.13, que concuerda con el Mw 7.2 obtenido en otros estudios del sismo de El Mayor-Cucapah.

Palabras clave: Cinemática de desplazamiento cosísmico, Sismología GPS, Posicionamiento Puntual Preciso, Análisis Espectral, sismo El Mayor-Cucapah, Sismogeodesia.

**Abstract**

El Mayor-Cucapah earthquake Mw 7.2 on April 4, 2010, occurred on Mexicali Valley near the international border between California, USA and Baja California, Mexico. The objective of this paper was to examine GPS as a complementary tool for seismic studies and to estimate earthquake seismic moment and Mw. For this purpose the capabilities of high-rate GPS (5 Hz) data located in the northern part of the seismic rupture has been explored to obtain the kinematic coseismic displacements. GPS data were processed using Precise Point Positioning method with GIPSY-OASIS II software, then applying the Fast Fourier Transform to the position time series, spectral parameters, seismic moment and Mw were calculated. A good agreement was found in terms of signal correlation of the GPS displacements, by comparing strong-motion seismic records integrated to displacement, using filtering parameters for two sets of instruments. Kinematic GPS displacement spectra clearly shows the low frequency displacement spectral level (~0.2 Hz) when compared with double integration of strong-motion data. It is easy to calculate the static coseismic motion from GPS data, however it is very difficult to calculate it from strong-motion data. A simple earthquake source model is suitable for the GPS dataset used in this work, estimated on Mw=7.19±0.13, was in according with Mw 7.2 obtained in other studies of the El Mayor-Cucapah earthquake.

Key words: Kinematic coseismic displacement, GPS Seismology, Precise Point Positioning, Spectral Analysis, El Mayor-Cucapah earthquake, Seismogeodesy.

J. C. Robles-Avalos
Posgrado en la División de Ciencias de la Tierra
Centro de Investigación Científica
y de Educación Superior de Ensenada
Baja California, Ensenada
B.C. México

J. A. González-Ortega*
J. J. González-García
J. A. Vidal-Villegas
Departamento de Sismología
División de Ciencias de la Tierra
Centro de Investigación Científica
y de Educación Superior de Ensenada
Baja California, Ensenada
B.C. México
*Corresponding author: aglez@cicese.mx

## Introduction

El Mayor-Cucapah earthquake has provided an important opportunity to study about the geodynamics of the northwest region of Mexico (Fletcher *et al*., 2016), as spatial and tectonic geodesy (Wei *et al*., 2011). The use of GPS in seismology was first documented by Hirahara *et al*., (1994), Ge *et al*., (2000) and Nikolaidis *et al*., (2001), who demonstrate the potential of GPS as a seismological instrument. For instance, Larson *et al*., (2003) using GPS (1 Hz) achieved to observe the kinematic displacements of the Alaska Denali earthquake (*Mw* 7.9) in 2002, suggesting that GPS observations are crucial to study rupture processes. Miyazaki *et al*., (2004) compared displacements from GPS with the double integration of the acceleration records, finding a good correlation between both for the Tokachi-Oki earthquake (*Mw* 8.3, occurred in 2003). Blewitt *et al*., (2006) demonstrated the GPS ability to estimate the magnitude of a megathrust earthquake, using data from up to only a few minutes after earthquake initiation, as well as its high tsunamigenic potential for the Sumatra–Andaman earthquake (*Mw* 9.2-9.3) in 2004; whereas, Hung *et al*., (2017) shown that 5 Hz high-rate GPS observations is an optimal sampling rate for GPS seismology as observed for the Ruisi Taiwan earthquake occurred in 2013. Nowadays, broadband and/or strong-motion seismic instruments located with high-rate GPS receivers are the best instrumental candidates to measure the complexity in the seismic source, rapid slip characterization of finite fault rupture and also for applications on early seismic warning systems (Melgar *et al*., 2013; Bock *et al*., 2011; Bock and Melgar, 2016).

Northern Baja California tectonics is primary dominated by right-lateral strike slip of ~50 mm/yr along southernmost San Andreas Fault system, between the Pacific and North American plates (Argus *et al*., 2010; DeMets *et al*., 2010) (Figure 1-inset). The El Mayor-Cucapah earthquake (32.278° N, 115.339° W; 4 km Depth; Mw 7.1; To=2010-04-04 22:40:40 UTC; RESNOM Database) of April 4, 2010, Mw 7.2, had a complex bidirectional rupture divided into two main domains from the epicentral zone located in the southeast corner of the Sierra Cucapah mountain range (Hauksson *et al*., 2010; Fletcher *et al*., 2014). The rupture in the northern section spread through the Cucapah mountains by several multiple faults-segments: Pescadores, Borrego, Paso Superior e Inferior. While in the southern section it extended through the Colorado River Delta, where it was possible to identify a new fault named Indiviso. The extent of the rupture was around 120 km (Figure 1) (González-García *et al*., 2010; Wei *et al*., 2011, Fletcher *et al*., 2014).

The characterization of a seismic source depends primarily on the direction of propagation of the seismic waves, distribution of the rupture and the magnitude of the coseismic displacements (Hanks, 1981). One way to estimate earthquake source parameters (seismic moment, stress drop and source radius) is computing the Fast Fourier Transform (FFT) to the displacements in the far-field (Savage, 1972), and getting the spectral parameters (level at low frequencies, corner frequency and slope to high frequencies), to obtain the seismic moment ($M_0$) (Brune, 1970), and then the moment magnitude (Mw) (Hanks and Kanamori, 1979) of an earthquake.

High-rate GPS (from 1-10 Hz) displacements has been proved very useful for monitoring long-period ground motion, moreover, the optimal combination of near-source GPS and seismic strong-motion data covers a broad spectrum of coseismic motion, from high frequencies to long periods (Bock and Melgar, 2016). Taking advantage of the availability of high-rate GPS records (5 Hz) nearby the seismic rupture of the El Mayor-Cucapah earthquake, the position ground motion was obtained, and then the results were compared with the double integration of acceleration data, for two sets of located (close to each other) GPS and strong-motion instruments. In the case of acceleration data a first order Butterworth filter was used within 0.10 – 50 Hz (Bendat and Piersol, 2011; Oppenheim and Shafer, 2011) in the frequency domain, while not for the GPS position. Finally, the earthquake seismic moment was estimated using a simple earthquake source model (Brune, 1970; Kumar *et al*., 2012) and moment magnitude was obtained following Hanks and Kanamori (1979).

## Data and Methods

High-rate GPS (5Hz) data were used from the Plate Boundary Observatory GPS network (Figure 1), obtained through the University NAVSTAR Consortium (UNAVCO) and acceleration data from Southern California Earthquake Data Center (SCEDC), and Center for Engineering Strong Motion Data (CESMD) for the El Mayor-Cucapah earthquake.

The technique used to process the GPS data was Precise Point Positioning (PPP) with GIPSY-OASIS software (Zumberge *et al*., 1997; Kouba and Heroux 2001). PPP is a positioning technique that is based on precise

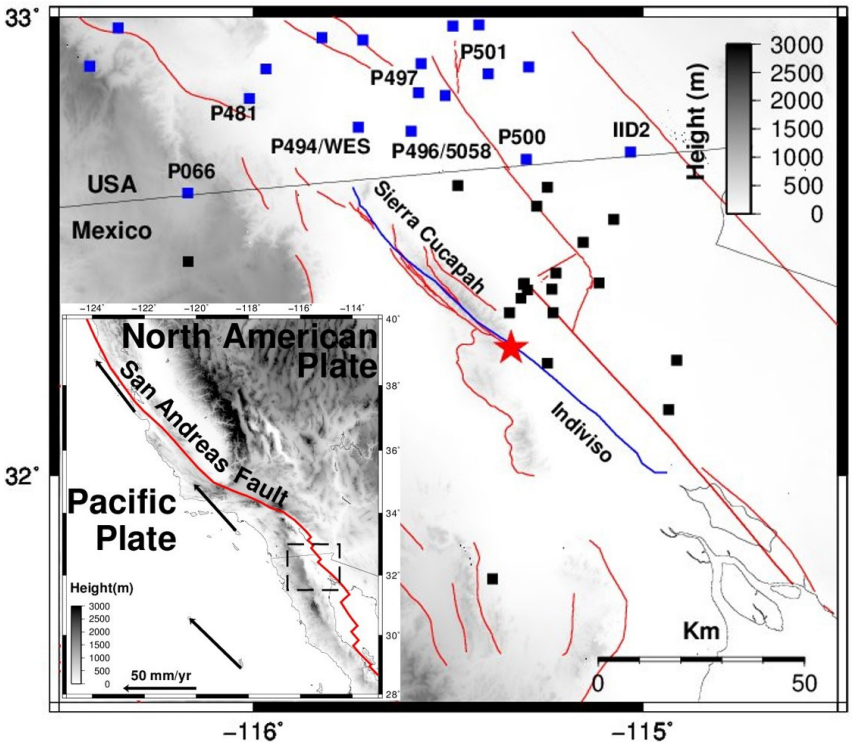


**Figure 1.** Tectonic setting of the north Baja California region, where the El Mayor-Cucapah earthquake occurred. The red star denotes the earthquake epicenter. Blue line denotes the surface rupture [Fialko *et al.,* 2010] and red lines denote known active faults. Blue squares denote GPS continuous recording sites in USA during the earthquake occurrence and black squares are GPS temporal surveyed sites after the earthquake (González-Ortega *et al*., 2014). P494/WES and P496/5058 are colocated GPS and strong-motion instruments; as well as, P066, P481 P497, P50, P500 and IID2 are GPS stations used in the present study. Inset illustrates a broader tectonic setting of the study area. Black vectors shows the tectonic motion with respect to North American Plate.

position coordinates obtention for a single station without a reference station, using precise orbit products and clock corrections provided by the International GNSS Service (IGS) (Abdallah and Schwieger, 2014). This technique can be used for both kinematic and static GPS processing. To achieve centimeter-level accuracy estimates, several modeling effects must be taken into account, such as the atmospheric effects on the carrier phase, as well as terrestrial and oceanic tides (Heroux *et al*., 2001). Thus, from far-field displacements in the frequency domain, earthquake seismic moment and magnitude can be obtained (Hanks and Wyss, 1972; Johnson and McEvilly, 1974).

The simplest and widely used earthquake source models are those proposed by: Haskell (1964) and Brune (1970). In the Haskell's model, two corner frequencies $f_r = \frac{2}{t_r}$ and $f_d = \frac{2}{t_d}$ are defined. Where $t_r$ is rupture time and $t_d$ is rise time. The spectrum is flat for frequencies less than $f_r$, then goes as $f^{-1}$ between $f_r$ and $f_d$, to finally decay as $f^{-2}$ for high frequencies. Thus the spectrum is parametrized by three factors, seismic moment Mo, raise time $t_d$ and rupture time $t_r$ (Stein and Wysession, 2003). The Brune's model has a single corner frequency, $f_c$, that combines the effects of rise and rupture time. The amplitude spectrum corresponds to displacements observed in the far-field; however, it is also applicable for observations in the near-field as long as the source-receiver distance is greater than the wavelength of the seismic waves (Madariaga, 1989). In the present case, a wavelength of ~26 km is obtained when considering seismic wave velocity of 3.3 km/s (Fuis *et al*., 1982) and 8 s period of the first oscillation for P494 station (Figure 2).

One of the most important spectral parameter is the flat line-segment of the amplitude spectrum at low frequencies as proposed by Haskell (1964) and Brune (1970). This frequency line-segment is commonly referred as $\Omega_0$, spectral level to low frequencies, from this parameter seismic moment is (Brune, 1970; Archuleta *et al*., 1982),

$$M_o = \frac{\Omega_0}{F_s R_{\theta\phi}} 4\pi\rho R\beta^3 \quad (1)$$

Where $\Omega_0$ is the line-segment at low frequencies, $R_{\theta\phi}$ is the average radiation pattern for *S* waves (~0.6), $\rho$ is the density of the medium (2.75 $\frac{g}{cm^3}$) and $\beta$ the s-wave velocity (3.3 x $10^5$ $\frac{cm}{s}$ ) (Fuis *et al*., 1982), $R$ is the distance from the hypocenter to the observation site and $Fs$ is the free surface factor (2). Finally, we used the moment magnitude relation proposed by Hanks and Kanamori [1979], in which *Mo* is in units of dyne-cm,

$$Mw = \frac{2}{3} logM_o - 10.7 \quad (2)$$

**Results**

GPS position time series corresponding to the nearest sites to the earthquake rupture are shown in Figure 2. The kinematic displacement generated by the passage of the seismic waves can be observed, as well as the coseismic permanent displacement, derived from the surface motion of the El Mayor-Cucapah earthquake. Differences in amplitude and oscillation are due to the type of soil and epicentral distance. P494 is located ~65 km from the epicenter in the west Salton Sea basin; while P481 is ~87 km in the Peninsular Ranges. To estimate the coseismic displacements, the linear trend of the surperficial pre-arrival seismic wave was first calculated and then the entire record of the

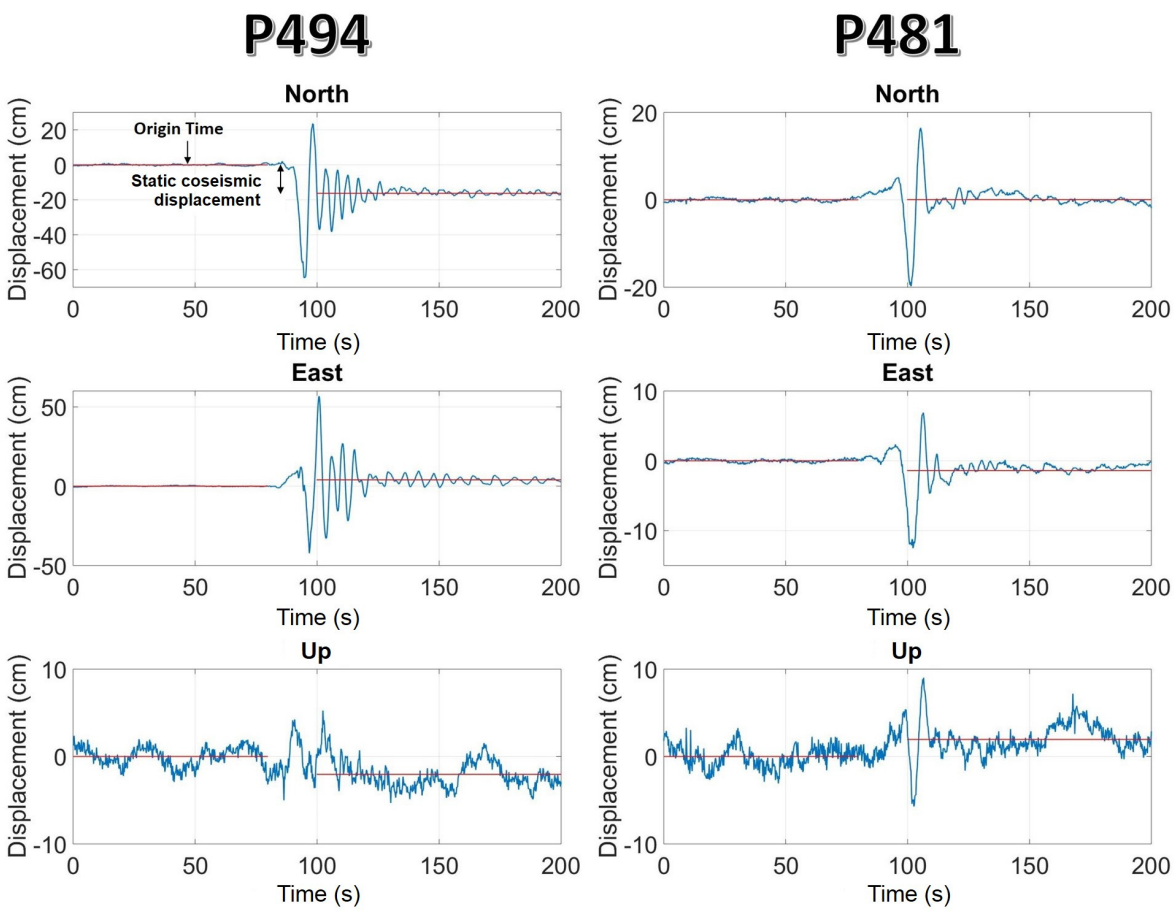


**Figure 2.** GPS position time series. Left column, GPS site P494, ~65 km from epicenter. Right column, GPS site P481, ~87 km from epicenter. Red lines indicate linear detrend removed before and after the S-wave arrival to estimate the static coseismic offsets.

position time series. Subsequently, the mean of the oscillations of the pre-arrival and post-arrival segments was calculated, the difference between both segments corresponds to the static (permanent) coseismic displacement. In Table 1, the kinematic and static coseismic displacements for GPS sites processed in this study are presented.

GPS position time series were compared with the displacement series obtained from the double integration of the accelerometer records from WES and 5058 accelerograph stations, located at <1 km from GPS sites P494 and P496, respectively (Figure 3). Horizontal components show alignment in phase and similarity in amplitudes (see inset plots). For strong-motion data several tests to find the frequency range and order for the Butterworth filter were performed. First-order Butterworth bandpass filter was selected, from 0.08 and 0.20 to Nyquist frequency for WES and 5058 respectively. This type of filter allows to improve the position of the time series and to carry out the comparison with GPS position time series. High order Butterworth filters tend to generate biases in position baseline and cause distortions [Oppenheim and Schafer, 2011].

To compare the kinematic GPS displacements and double integrated accelerogram data, a normalized cross-correlation was used. In general, correlation values are better in the east-west (>0.90) than north-south (>0.70), due to the smaller kinematic coseismic displacement in the east-west direction. Consequences of seismic filtering tends to diminish the amplitudes of the displacement series obtained from

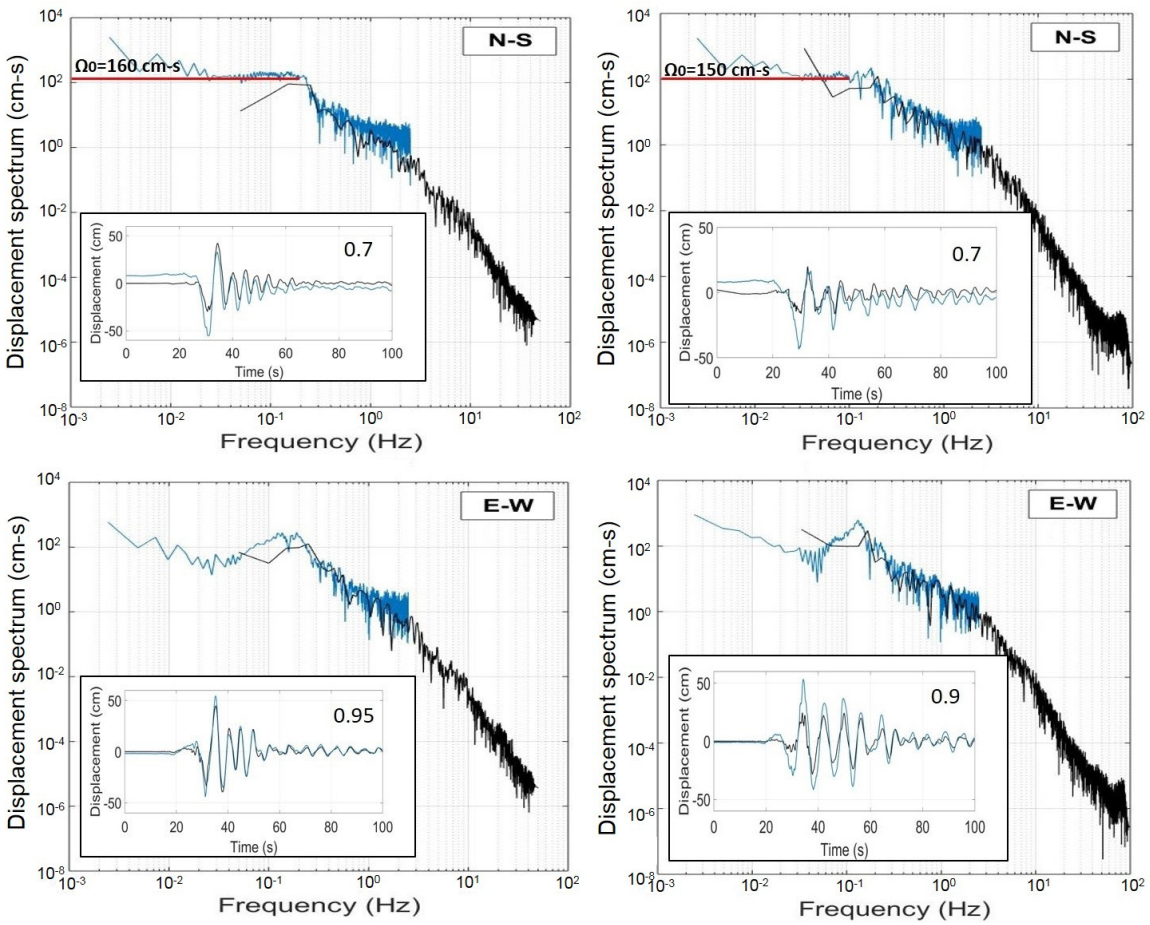


**Figure 3.** Displacement spectrum comparisons from collocated strong motion (black) and high-rate GPS (blue). Left column, horizontal displacement spectrum at P494-GPS and WES accelerograph station. Right column, horizontal displacement spectrum at P496-GPS and 5058 accelerograph station. Red horizontal lines indicate $\Omega_0$ value. Insets show comparison between GPS and integrated (from strong-motion) time series displacement and corresponding cross-correlation values estimate.

**Table 1.** 3D Coseismic displacements estimates from GPS position time series. Includes earthquake distance to GPS sites, peak-to-peak oscillation seismic wave motion, flat line segment amplitude value at low frequencies $\Omega_o$, $M_o$ and $M_w$.

| GPS site | Lat. | Long. | Epicentral distance (km) | Kinematic peak to peak oscillation, north (cm) | Kinematic peak to peak oscillation, east (cm) | Kinematic peak to peak oscillation, Up (cm) | Static coseismic north (cm) | Static coseismic east (cm) | Static coseismic Up (cm) | $\Omega_o$ (cm-s) | $M_o$ (dyne-cm) 1x10$^{26}$ | $M_w$ |
|---|---|---|---|---|---|---|---|---|---|---|---|---|
| P494 | 32.760 | -115.732 | 65 | 90 | 100 | 10 | -18 | 4 | ~ -1 | 160 | 10.8 | 7.32 |
| P496 | 32.751 | -115.596 | 58 | 60 | 95 | 24 | -17 | ~2 | ~0 | 150 | 9.0 | 7.27 |
| P497 | 32.835 | -115.577 | 67 | 40 | 60 | 15 | -9 | ~1 | ~1 | 125 | 8.7 | 7.26 |
| P501 | 32.876 | -115.398 | 67 | 45 | 36 | 10 | -5 | ~2 | ~1 | 137 | 9.5 | 7.29 |
| P500 | 32.690 | -115.300 | 46 | 26 | 30 | 12 | -4 | 5 | ~0 | 93 | 4.4 | 7.06 |
| IID2 | 32.706 | -115.032 | 54 | 16 | 21 | NA | ~ -2 | 3 | ~0 | 77 | 4.3 | 7.06 |
| P481 | 32.822 | -116.012 | 87 | 36 | 20 | 15 | ~ -2 | ~ -1 | ~0 | 74 | 6.7 | 7.18 |
| P066 | 32.617 | -116.170 | 90 | 16 | 11 | 13 | ~0 | -7 | ~0 | 51 | 4.8 | 7.08 |

accelerogram double integration data when compared to those obtained with GPS. Static coseismic displacements are not observable in strong-motion due to wideband limitation but in GPS these are clearly captured.

Figure 3 shows horizontal GPS and strong-motion source spectra comparison for P494-GPS and WES, as well as, P496-GPS and 5058. With GPS spectra, the amplitude at low frequencies $\Omega_0$ is easily identified. After a value of ~0.2Hz, amplitudes decay at $f^{-2}$ as frequency increases up to where GPS spectra turns constant. At this point, seismic oscillations with spectral amplitudes of ~2cm·s associated with frequency values ~1Hz (periods ≥ 1 s for 5Hz GPS sampling rate), are not detectable with GPS. On the other hand, with strong-motion displacement spectra, two corner frequencies at ~0.2Hz and ~3Hz can be identified. For frequencies >3Hz amplitude decay as $f^{-4}$. These amplitude decays are related to attenuation and site effects [Shearer, 1999].

Seismic moment ($M_o$) and moment magnitude ($M_w$) of the El Mayor-Cucapah earthquake is $M_o$ = 7.3±3.5x10$^{26}$ dyne-cm, $M_w$ = 7.19±0.13 using GPS spectra (Table 1), and *Mo* = 6.4±0.07x10$^{26}$ dyne-cm, $M_w$ = 7.14±0.01, using WES and 5058 strong-motion data spectra. These values are similar to estimates obtained from seismic and geodetic data inversion $M_o$ = 9.9x10$^{26}$ dyne-cm, $M_w$ = 7.26 [Wei *et al*., 2011] and from field measurements of $M_o$ = 7.2x10$^{26}$ dyne-cm, $M_w$ = 7.17 [Fletcher *et al*., 2014].

Figure 4 shows the El Mayor-Cucapah static coseismic horizontal displacements. The maximum horizontal static coseismic displacement is ~1.16 m, in the N137°E direction, ~8 km from the epicenter, in the southeastern part of the Sierra Cucapah, and the maximum vertical displacement is ~-0.64 m. The displacement pattern, clearly observed in the northeast is consistent with a right-lateral focal mechanism of The El Mayor-Cucapah earthquake (González-Ortega *et al*., 2014). These authors, estimated earthquake moment magnitude using dislocation inversion methods from a finite coseismic slip model composed of several fault segments using GPS and InSAR static displacements in a homogeneous (Fialko *et al.,* 2010) and in an layered earth structure [Huang *et al*., 2016].

## Discussion

Zheng *et al*., (2012), also used high-rate GPS data with the aim of carrying out the seismotectonics analysis of El Mayor-Cucapah earthquake with different methodology as in this work. They used the Cut and Paste method (CAP) developed by Zhu and Helmberger (1996), which allows separating the $P_n$ and surface waves independently, not requiring an accurate crustal velocity model or a high number of stations, but a good azimuthal coverage for the focal mechanism inversion and earthquake magnitude. Also, Allen and Ziv (2011), re-processed in a simulated real-time high-rate GPS static displacement data, to estimate earthquake magnitude via static slip inversion, using preliminary earthquake hypocenter from seismic data and a catalog of active faults, for the purpose of earthquake early warning system test in southern California.

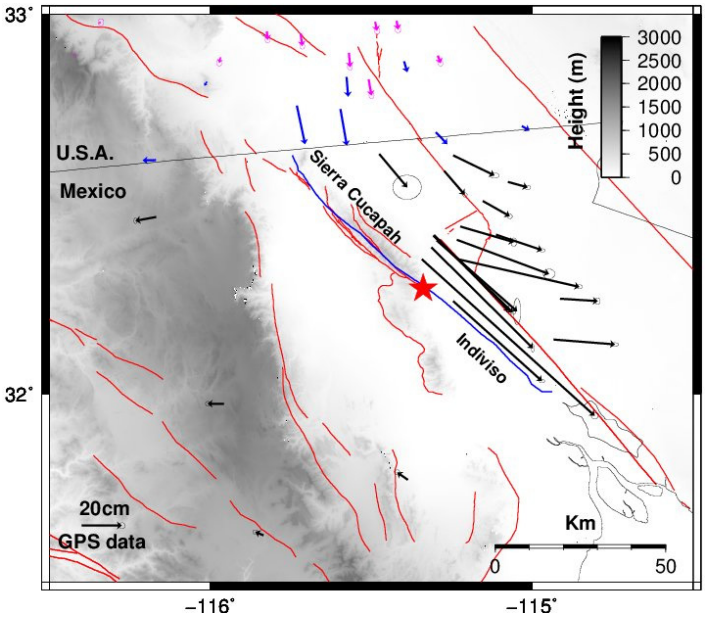


**Figure 4.** GPS horizontal coseismic displacements from El Mayor-Cucapah earthquake. Blue vectors are estimates obtained in this study. Black are displacements from Gonzalez-Ortega (2014), and magenta are from GPS Explorer Data Products (http://geodemo-c.ucsd.edu). The red star denotes the earthquake epicenter. Blue line denotes the surface rupture [Fialko *et al.,* 2010] and red lines denote known active faults.

Differences between Zheng *et al*., (2012), and the present work lies in the GPS data processing; while we used the PPP technique, they used the Double Differences (DD). For the DD technique (Herring *et al.*, 2015) it is necessary to have a reference station, which must be located at a distance far enough to not be affected by seismic waves, but close enough to act as reference station which guarantees the same satellites observation of the sites of interest. Such condition is not required with PPP technique, as it uses precise GPS orbit and clock data products with centimeter accuracy. Although the methodology used in Zheng *et al*., (2012) and the present one differ in estimating GPS time series and seismic moment, in general, position time series and moment magnitude results are very similar and confirm earlier studies using GPS high-rate data from El Mayor-Cucapah earthquake (Allen and Ziv, 2011; Bock *et al.*, 2011).

With high-rate GPS spectral analysis, amplitude at low frequencies is clear to identify in contrast to accelerogram data. This flat low frequency section is associated with large displacement amplitudes generated by the passage of surperficial seismic waves (Udias, 1989). Thus, estimates of $M_o$ and $M_w$ can have a greater degree of certainty with GPS data than with accelerometer records. GPS data can be of crucial importance for estimating major earthquake magnitude in real time (Blewitt *et al.*, 2006; Bock and Melgar, 2016). According to the present results, average $\Omega_0$ value with GPS data is 115±4 cm-s, while with accelerogram data is 90±8 cm-s. However, as GPS is sampled at 5 Hz, for frequencies >2.5 Hz (Nyquist frequency) GPS is unable to observe spectral displacements below 2 cm-s, which does not happen with the acceleration records. This highlights the importance of the complementarity between both instruments, closely located GPS and strong-motion, for near field displacements earthquake studies.

## Conclusion

High-rate (5 Hz) kinematic GPS position time series of the El Mayor-Cucapah earthquake were studied and compared to the displacement series obtained from the double integration of strong-motion data. The comparison shows good agreement in terms of cross-correlation, for P494-GPS and WES, and, P496-GPS and 5058, instruments at ~75 km from epicenter. Kinematic GPS data at low frequencies, associated with large spectrum displacements, help to clearly identify the flat line segment amplitude better than accelerogram data, and thus using a simple earthquake source model the earthquake seismic moment, Mo=7.3±3.5x$10^{26}$ dyne-cm, Mw=7.19±0.13 could be estimated, similar

to Mw 7.2 as previously reported using other methodologies. Static coseismic displacements are very difficult to obtain from accelerogram data, however with GPS data, these are easily obtained and consistent with the right-lateral strike-slip mechanism of the El Mayor-Cucapah earthquake.

## Data and Resources

High-rate GPS data can be found at UNAVCO, ftp://data-out.unavco.org/pub/highrate/5-Hz/rinex/ (last accessed April 2018). Coseismic displacements from the northern side of the El Mayor-Cucapah rupture can be found at GPS Explorer, http://geodemo-c.ucsd.edu (last accessed April 2018). Accelerometric data can be found at SCEDC, http://scedc.caltech.edu/research-tools/waveform.html (last accessed April 2018) and CESMD, https://www.strongmotioncenter.org/cgi-bin/CESMD/search_options.pl (last accessed April 2018). Map figures were generated by Generic Mapping Tool (GMT) software [Wessel *et al*., 2013].

## Acknowledgments

The authors would like to thank Editor Dr. Manuel Berrocoso-Dominguez and two anonymous reviewers for their valuable suggestions. This work was partially financially supported by CONACyT though a graduate scholarship to Robles-Avalos J.C. (2015-2017). We thank Dr. Sara Ivonne Franco Sánchez and Dr. Luis Mungía Orozco for their comments during this work. Also we acknowledge to local people during the GPS campaigns in northern Baja California.

## References

Abdallah, A. and Schwieger, V. (2014). Accuracy Assessment Study of GNSS Precise Point Positioning for Kinematic Positioning. In Schattenberg, J., Minßen, T. F.: Proceeding on 4th International Conference on Machine Control and Guidance (MCG), Braunschweig: Institut für mobile Maschinen und Nutzfahrzeuge, Braunschweig, Germany.

Allen, R. M. and Ziv, A. (2011). Application of Real-Time GPS to earthquake early warning. Geophysical Research Letters, 38, L16310.

Archuleta, R. J., Cranswick, E., Mueller, C., and Spudich, P. (1982). Source parameters of the 1980 Mammoth Lakes, California, earthquake sequence. Journal of Geophysical Research: Solid Earth, 87(B6), 4595-4607.

Argus, D.F., Gordon, R.G., Heflin, M.B., Ma, Ch., Eanes, R.J., Willis, P., Peltier, W.R. and Owen, S.E. (2010). The angular velocities of the plates and the velocity of Earth's center from space geodesy. Geophysical Journal International, 180(3), 913-960.

Bendat, J.S., Piersol, A.G. (2011). Random Data: Analysis and Measurement Procedures. John Wiley & Sons. 640 pp.

Blewitt, G., Kreemer, C., Hammond, W. C., Plag, H. P., Stein, S., and Okal, E. (2006). Rapid determination of earthquake magnitude using GPS for tsunami warning systems. Geophysical Research Letters, 33(11).

Bock, Y. and Melgar D. (2016). Physical applications of GPS geodesy: a review. Reports on Progress in Physics. 79, 106801, 119 p.

Bock, Y., Melgar, D., and Crowell B.W. (2011). Real-time strong motion broadband displacement from collocated GPS and accelerometers. Bulletin of the Seismological Society of America. 101(6). 2904-2925.

Brune, J. N. (1970). Tectonic stress and the spectra of seismic shear waves from earthquakes. Journal of Geophysical Research, 75(26), 4997-5009.

DeMets, C., Gordon, R.G. and Argus, D.F. (2010). Geologically current plate motions. Geophysical Journal International, 181(1), 1-80.

Fialko, Y., A. González, J. González, S. Barbot, S. Leprince, D. Sandwell, and D. Agnew (2010), Static rupture model of the 2010 Mw 7.2 El Mayor-Cucapah earthquake from ALOS, ENVISAT, SPOT and GPS data, Abstract T53B-2125 presented at 2010 Fall Meeting, AGU, San Francisco, Calif.

Fletcher, J., Teran, O.J., Rockwell, T. K., Oskin, M., Hudnut, K. W., Mueller, K. J. Spelz, R. M., Akciz, S. O., Masana, E., Faneros, G., Fielding, E. J., Leprince, S., Morelan, A. E., Stock, J. Lynch, D. K. Elliott, A. J., Gold, P., Liu-Zeng, J., González-Ortega, A. Hinojosa-Corona, A., and González-García, J. (2014). Assembly of a large earthquake from a complex fault system: Surface rupture kinematics of the 4 April 2010 El Mayor–Cucapah (Mexico) Mw 7.2 earthquake. Geosphere, 10 (4), 797-827.

Fletcher, J.M., M.E. Oskin, and Teran, O.J. (2016). The role of a keystone fault in triggering the complex El Mayor–Cucapah

earthquake rupture. Nature Geoscience, 9, 303–307.

Fuis, G.S., Mooney, W.D., Healey, J.H., McMechan G.A., and Lutter, W.J. (1982). Crustal structure of the Imperial Valley region. USGS professional paper 1254, 25-50.

Ge, L., Han, S., Rizos, C., Ishikawa, Y., Hoshiba, M., Yoshida, Y. and Himori, S. (2000). GPS seismometers with up to 20 Hz sampling rate. Earth, planets and space, 52(10), 881-884.

González-García, J. J., J. A. González Ortega, Y. Bock, Y. Fialko, E. J. Fielding, J. Fletcher, J. E. Galetzka, K. W. Hudnut, L. Munguia, and S. M. Nelson. (2010). Seismotectonics of the 2010 El Mayor Cucapah—Indiviso earthquake and its relation to seismic hazard in southern California, Abstract T53B-2117 presented at 2010 Fall Meeting, AGU, San Francisco, Calif.

González-Ortega, A., Y. Fialko, D. Sandwell, F. Alejandro Nava-Pichardo, J. Fletcher, J. González-García, B. Lipovsky, M. Floyd, and G. Funning (2014), EL Mayor-Cucapah (Mw7.2) earthquake: Early near-field posteismic deformation from InSAR and GPSobservations, J. Geophys. Res. Solid Earth, 119, 1482-1472.

González-Ortega, J. A., (2014). Análisis sismo-geodésico del sismo El Mayor-Cucapah (Mw=7.2) del 4 de abril de 2010, Baja California Tesis de doctorado en ciencias. Centro de Investigación Científica y de Educación Superior de Ensenada, Baja California.

Hanks, T. (1981). The Corner Frequency Shift, Earthquake Source Models, and Q. Bulletin of the Seismological Society of America. 71 (3); pp. 597-612.

Hanks, T. and Kanamori, H. (1979). A moment magnitude scale. Journal of Geophysical Research. 84(B5), 2348–2350.

Hanks, T. and Wyss, M. (1972). The use of body-wave spectra in the determination of seismic-source parameters. Bulletin of the Seismological Society of America, 62(2), 561-589.

Haskell, N. (1964). Total energy and energy spectral density of elastic wave radiation from propagating faults. Bulletin of the Seismological Society of America, 54, 1811-1841.

Hauksson, E., Stock, J., Hutton, K., Yang, W., Vidal-Villegas, J.A. and Kanamori, H. (2010). The 2010 Mw 7.2 El Mayor-Cucapah Earthquake Sequence, Baja California, Mexico and Southernmost California, USA: Active Seismotectonics along the Mexican Pacific Margin. Pure Applied Geophysics. 168, 1255–1277.

Heroux, P., Kouba, J., Collins, P., and Lahaye, F. (2001). GPS carrier phase point positioning with precise orbit products. In Procedings of the KIS, 5-8. Pierre Heroux Geodetic Survey Division, Natural Resources Canada.

Herring, T. A., R. W. King, M. A. Floyd, and S. C. McClusky (2015). Introduction to GAMIT/GLOBK, Release 10.6, Mass. Inst. Of Technol., Cambridge, Massachusetts.

Hirahara, K., Nakano, T. and Hoso, Y. (1994). An experiment for GPS strain seismometer. In Proceeding of Japanese Symposium on GPS. pp. 67-75. 15-16 December, Tokio, Japan.

Huang, M.-H., E. J. Fielding, H. Dickinson, J. Sun, J. Alejandro González-Ortega, A. M. Freed, and R. Bürgmann (2016). Fault Geometry Inversion and Slip Distribution of the 2010 Mw 7.2 El Mayor-Cucapah Earthquake from Geodetic Data, J. Geophys. Res. Solid Earth, 121, 607-622.

Hung, H-K, Rau, R-J., Benedetti, E., Branzanti, M., Mazzoni, A., Colosimo, G., and Crespi, M. (2017). GPS Seismology for a moderate magnitude earthquake: Lessons learned from the analysis of the 31 October 2013 ML 6.4 Ruisui (Taiwan) earthquake. Annals of Geophysics, 60, 5, 2017; S0553.

Johnson, L. R., and McEvilly, T. V. (1974). Near-field observations and source parameters of central California earthquakes. Bulletin of the Seismological Society of America, 64(6), 1855-1886.

Kouba, J., and Heroux, P. (2001). Precise point positioning using IGS orbit and clock products. GPS solutions, 5(2), 12-28.

Kumar A., Kumar, A., Mittal, H., Kumar, A., and Bhardwaj, R. (2012). Software to Estimate Earthquake Spectral and Source Parameters. International Journal of Geosciences, 3, 1142-1149.

Larson, K. M., Bodin, P., and Gomberg, J. (2003). Using 1-Hz GPS data to measure deformations caused by the Denali fault earthquake. Science, 300(5624), 1421-1424.

Madariaga, R. (1989). Propagación de Ondas Sísmicas en el campo cercano. Física de la Tierra, 1, 51-73. Ed. Universidad Complutense Madrid.

Melgar, D., Crowell B.W., Bock Y. and Hasse J.S. (2013). Rapid modelling of the 2011 Mw 9.0 Tohoku-Oki earthquake with seismogeodesy. Geophysical Research Letters, 40(12).2963-2968.

Miyazaki, S. I., Larson, K. M., Choi, K., Hikima, K., Koketsu, K., Bodin, P. and Yamagiwa, A. (2004). Modeling the rupture process of the 2003 September 25 Tokachi Oki (Hokkaido) earthquake using 1 Hz GPS data. Geophysical Research Letters, 31(21).

Nikolaidis, R.M., Bock Y., de Jonge P.J., Shearer P., Agnew D.C. and Van Domselaar M. (2001). Seismic wave observations with the Global Positioning System. Journal of Geophysical Research, 106 (10) 21879-21916.

Oppenheim A., and Schafer R. (2011). Digital Signal Processing. Prentice-Hall of India Pvt. Limited. 585 pp.

Savage, J. C. (1972). Relation of corner frequency to fault dimensions. Journal of Geophysical Research, 77(20), 3788-3795.

Shearer P. (1999). Introduction to seismology. Cambridge University Press.

Stein, S., and Wysession, M. (2003). An introduction to seismology, earthquakes, and earth structure. Blackwell Pub.

Udias, A. (1989). Parámetros del foco de los terremotos. Física de la Tierra, 1, 87-104. Ed. Universidad Complutense Madrid.

Wei, S., Fielding, E., Leprince, S., Sladen, A., Avouac, J.P., Helmberger, D., Hauksson, E., Chu, R., Simons, M., Hudnut, K., Herring, T., Briggs, R. (2011). Superficial simplicity of the 2010 El Mayor–Cucapah earthquake of Baja California in Mexico. Nature Geoscience 4, 615-618.

Wessel, P., W. H. F. Smith, R. Scharroo, J. Luis, and F. Wobbe (2013), Generic mapping tools: Improved version released, EOS Trans. AGU, 94(45), 409–410.

Zheng, Y., Li, J., Xie, Z., Ritzwoller, M.H. (2012). 5 Hz GPS seismology of the El Mayor-Cucapah earthquake: estimating the earthquake focal mechanism. Geophysical Jounal International, 190, 1723-1732.

Zhu, L., and Helmberger, D. V. (1996). Advancement in source estimation techniques using broadband regional seismograms. Bulletin of the Seismological Society of America, 86(5), 1634-1641.

Zumberge, J. F., Heflin, M. B., Jefferson, D. C., Watkins, M. M., and Webb, F. H. (1997). Precise point positioning for the efficient and robust analysis of GPS data from large networks. Journal of Geophysical Research, 102(B3), 5005-5017.